Structure and Dynamics of Binary Soft-Colloid mixtures

Inaugural-Dissertation
zur Erlangung des Doktorgrades der
Mathematisch-Naturwissenschaftlichen Fakultät
der Heinrich-Heine-Universität Düsseldorf

vorgelegt von
Manuel Alfonso Camargo Chaparro
aus Sogamoso (Kolumbien)

Düsseldorf, Mai 2011

Aus dem Institut für Theoretische Physik
der Heinrich-Heine Universität Düsseldorf

Gedruckt mit Genehmigung der
Mathematisch-Naturwissenschaftlichen Fakultät
der Heinrich-Heine-Universität Düsseldorf

Referent: Prof. Dr. Christos N. Likos
Koreferent: Prof. Dr. Jan K. G. Dhont
Koreferent: Prof. Dimitris Vlassopoulos

Tag der mündlichen Prüfung: 26. Mai 2011

The work described in this thesis has been published in a number of papers, which constitute the following self-contained chapters:

Chapter 2. M. Camargo and C. N. Likos, *Phase separation in star-linear polymer mixtures*, J. Chem. Phys. **130**, 204904 (2009).

M. Camargo and C. N. Likos, *Cluster formation in star-linear polymer mixtures: equilibrium and dynamical properties*, in preparation.

Chapter 3. M. Camargo and C. N. Likos, *Unusual features of depletion interactions in soft polymer-based colloids mixed with homopolymers*, Phys. Rev. Lett. **104**, 078301 (2010).

- Selected as PRL-Highlight in The Biological Physicist, Newsletter of the Division of Biological Physics of the American Physical Society, Vol. 9, No. 7, April 2010.
- Selected as Scientific Highlight 2010 by the European Network of Excellence "SoftComp".

Chapter 4. B. Lonetti, M. Camargo, J. Stellbrink, C. N. Likos, E. Zaccarelli, L. Willner, D. Richter, and P. Linder, *Ultrasoft Colloid/Polymer mixtures: structure and phase diagram*, Phys. Rev. Lett. **106**, 228301 (2011).

Chapter 5. M. Camargo and C. N. Likos, *Interfacial and wetting behavior of phase-separating ultrasoft mixtures*, Mol. Phys. **109**, 1121 (2011).

Chapter 6. M. Camargo, A. J. Moreno, and C. N. Likos, *Equilibrium dynamics of binary cluster crystals*, J. Stat. Mech. P10015 (2010).

Abstract

In this thesis, we examine the structure and the phase behavior of binary mixtures of soft-colloids in equilibrium. By employing coarse-grained models, we systematically study the properties of soft mixtures and contrast them with those of "hard" colloids.

The work is divided in two sections, each considering a particular system. The first part is devoted to the study of the effects of the addition of small linear (chain) polymer to star polymer suspensions. We commence with a coarse-graining approach that allows us to reduce the system complexity and to describe it by means of effective interactions between the central monomer. Thereafter, in a full two-component integral-equation approach we describe the demixing transition in the fluid phase of star/linear polymer mixtures for low and intermediate functionalities and several chain-to-star size ratios. In order to compare the one- and the two-component descriptions, we resort to the depletion interaction. For both hard sphere mixtures and colloid/non-adsorbing polymer mixtures the range of the depletion interaction increases with the size ratio. For the considered system, the range of the depletion potential is insensitive to the size of the depletant polymer. We discuss the physical origin of this and associated effects, as well as a mapping of the mixtures onto a one-component system. Finally, we offer a robust comparison to experimental results, showing the accuracy of the coarse-graining procedure for developing effective interactions between star-like micelles and polymer chains, in a wide range of concentrated mixtures. Without any adjustable parameter we find quantitative agreement between experiments and theory for the influence of the added chains on the inter-micelle structure and on the phase behavior.

In the second part, we focus on the so-called GEM particles, representing, e.g., amphiphilic dendrimers or ring polymers in solution. We apply density functional theory to study the interfacial and wetting properties of a phase-separating binary fluid within the mean-field approximation. The studied system can lead to first-order wetting transition which is characterized by a layering-like behavior due to the clustering properties of GEM particles. Finally, we describe the dynamic behavior of the crystal phase of GEM mixtures by means of extensive molecular dynamics simulations. In particular, we investigate the effect of the addition of non-clustering

particles on the dynamic scenario of one-component cluster crystals.

Zusammenfassung

In der vorliegenden Dissertation untersuchen wir die Struktur und das Phasenverhalten binärer Mischungen weicher Kolloide im Gleichgewicht. Mittels *coarse-grained* Modellen untersuchen wir systematisch die Eigenschaften weicher Mischungen und stellen sie denen harter Kolloide gegenüber. Die Arbeit ist in zwei Abschnitte unterteilt, wobei jeder ein besonderes Modell in Betracht zieht.

Der erste Teil ist der Untersuchung der Auswirkung gewidmet, welche durch Hinzufügung von linearen Polymerketten zu Sternpolymer Suspensionen hervorgerufen wird. Wir beginnen mit einem *coarse-graining* Ansatz der uns erlaubt, die Komplexität des Systems zu reduzieren und es mittels effektiver wechselwirkungen zwischen den Zentralmonomeren zu beschreiben. Anschließend beschreiben wir mit Hilfe eines vollständigen zweikomponentigen Integralgleichungsansatzes den Entmischungsübergang in der fluiden Phase von Stern/Ketten-Polymermischungen für niedrige und mittelgroße Funktionalitäten, sowie für verschiedene Größenverhältnisse zwischen Ketten und Sternen. Um die ein- und zweikomponentigen Beschreibungen zu vergleichen, greifen wir auf die Depletionswechselwirkung zurück. Sowohl für Harte-Kugel-Mischungen als auch für Mischungen von Kolloiden und nicht-adsorbierenden Polymeren nimmt die Reichweite der Depletionswechselwirkung mit zunehmendem Größenverhältnis zu. Für das betrachtete System ist die Reichweite des Depletionspotentials unabhängig von der Größe der Ketten. Wir erörtern den physikalischen Ursprung dieses und der damit verbundenen Effekte sowie die Übertragung der Mischungen auf einkomponentige Systeme. Anschließend zeigen wir mittels gewissenhaftem Vergleich zu experimentellen Ergebnissen die Genauigkeit des *coarse-graining*-Verfahrens für die Herleitung effektiver wechselwirkungen zwischen sternähnlichen Mizellen und Polymerketten über einen großen Bereich konzentrierter Mischungen. Ohne jegliche anpassbare Parameter finden wir quantitative Übereinstimmung zwischen Experiment und Theorie für den Einfluss hinzugefügter Ketten auf die intermizellare Struktur und auf das Phasenverhalten.

Im zweiten Teil legen wir den Schwerpunkt auf die sog. GEM-Teilchen, durch welche z.B. amphiphile Dendrimere oder Ringpolymere in Lösung repräsentiert werden können. Wir verwenden Dichtefunktionaltheorie, um die Grenzflächen- und

Benetzungseigenschaften eines phasentrennenden binären Fluids mittels der *Mean-field*-Näherung zu untersuchen. Die untersuchten Systeme können zu einem Benetzungsübergang erster Ordnung führen, welcher sich, aufgrund der Clustereigenschaften der GEM-Teilchen, durch ein der Schichtung ähnliches Verhalten kennzeichnet. Abschließend beschreiben wir das Phasenverhalten der kristallinen Phase der GEM-Mischungen mittels umfangreicher Molekulardynamik-Simulationen. Insbesondere untersuchen wir den Effekt, den das Zufügen von nicht-clusternden Teilchen auf das dynamische Szenario einkomponentiger Clusterkristalle hat.

Acknowledgments

In first place, I want to express my sincere gratitude to my advisor Prof. Christos N. Likos, who contributed immensely to the develop of this thesis with his profound physical insight, his patience, and his never-ending enthusiasm.

I also want to thank all the colleagues at the Institute for providing an excellent working atmosphere. In particular, I thank Ronald Blaak who was permanently willing to kindly answer to all my questions. I also owe special thanks to my officemates Arturo Narros, Sebastian Huißmann, and Dominic Lenz for always being ready to help me with major and minor issues.

I am very grateful to the German Academic Exchange Service (DAAD, Germany) and UAN-MEN-ICETEX-Colciencias (Colombia) for a PhD Grant through the Bilateral Exchange Program ALECOL, which enabled me to carried out this work.

Last but not least, I would like to thanks my wife, family, and friends for their support; I deeply appreciate it. Andrea thank you for the love you has offered me all this time.

Contents

Abstract v

Zusammenfassung vii

Acknowledgments ix

Introduction 1

1 Demixing transition in star-linear polymer mixtures 5
- 1.1 Introduction . . . 5
- 1.2 Coarse-grained model of the mixture . . . 7
- 1.3 Bulk structure and phase diagram . . . 10
  - 1.3.1 Fluid structure . . . 10
  - 1.3.2 Binodal lines . . . 11
- 1.4 Results . . . 12
  - 1.4.1 Chain-modified effective star-star interaction . . . 12
  - 1.4.2 Structure of the mixture . . . 15
  - 1.4.3 Demixing transition . . . 20
- 1.5 Concluding remarks . . . 25

2 Depletion interaction 27
- 2.1 Introduction . . . 27
- 2.2 Model . . . 29
- 2.3 Results . . . 29
- 2.4 Conclusions . . . 35

3 Star/Polymer Mixtures: Comparison with experiments **37**
3.1 Introduction 37
3.2 Methods 39
3.3 Results and Discussion 41
3.4 Concluding remarks 46

4 Wetting in GEM mixtures **47**
4.1 Introduction 47
4.2 Model and Method 49
4.3 Results 51
  4.3.1 Bulk properties 51
  4.3.2 Interfacial properties 54
  4.3.3 Wetting 59
4.4 Concluding remarks 68

5 Dynamics in binary cluster crystals **71**
5.1 Introduction 71
5.2 Model and Simulation 73
5.3 Results and Discussion 74
  5.3.1 Phase diagram and static structure 74
  5.3.2 Dynamics in real space 79
  5.3.3 Scattering functions 83
5.4 Conclusions 90

6 Conclusion and Overview **93**

Bibliography **97**

A Star polymers **105**

B Ornstein-Zernike equation **107**

C Non-ergodicity factor **109**

Introduction

The recent progress in synthesis and self-organization of nano- and microscopic colloidal particles and soft matter composites has expanded the possibilities to design and prepare new materials featuring controllable responses to different physical and/or chemical stimuli [1, 2]. In trying to achieve a comprehensible characterization of their static and dynamic macroscopic properties, the complex composition of soft materials gives rise to formidable theoretical and computational challenges. As a consequence of the large length- and time-scale asymmetries between the dissolved, mesoscopic aggregates and the microscopic components, a completely microscopic statistical description of this kind of systems is not possible. Nevertheless, the involved complexity can be greatly reduced by conveniently pre-averaging (coarse-graining) the degrees of freedom of some of the microscopic components, and subsequently mapping the original system onto an effective model, which contains a smaller number of components governed by effective interparticle interactions [3, 4, 5, 6, 7].

In essence, the emerging effective interactions are constrained free energies between appropriately chosen mesoscopic degrees of freedom (effective coordinates), once a canonical trace over the microscopic ones has been carried out. It has the advantage, that the choice of the effective coordinates does not alter dramatically the physical description of the system at hand[1], as long as the same level of approximation is preserved in the coarse-graining (CG) [4, 5]. In this way, simplified coarse-graining methods accounting for a minimal set of properties of the mesoscopic entities are perfectly well-suited to study generic/universal properties of soft matter systems [8]. In the realm of colloidal suspensions, which in their “simplest”

---

[1] However it does change the form of the effective interactions

description consist of a solution of hard particles (colloids, $\sim 1\,\text{nm}-1\,\mu\text{m}$) immersed in a fluid of much smaller ones (solvent molecules, ions, short polymers), a CG treatment is behind the effective screened Coulomb interaction between charged colloids at low density [9], i.e., the electrostatic part of the well-known DLVO potential, which has been of fundamental importance in the understanding of the stability of colloidal dispersions. The same CG procedure lies in the Asakura-Oosawa model for the depletion interaction [10, 11], which since long time has been employed to explain the equilibrium phase behavior of colloid-polymer mixtures [12], and lately to understand the formation and stability of clusters, gelation, repulsive-glass to attractive-glass transition and arrested spinodal decomposition [13].

Recently, the study of soft, deformable colloids have attracted a lot of interest because their singular properties and their relevance for technical application (e.g., design of filter materials, enhancement of catalytic activity) as well as for life sciences (e.g., noninvasive drug/gene delivery, pathogen detection) [2]. They are mainly polymer-based structures, which can be typically categorized into core-shell particles, being polymer-grafted nano-particles, micelles, microgels, star polymers, and dendrimers, to name some examples of the same. As a consequence of their internal structure, these particles may mutually interpenetrate when pressed together and most important, their *softness* is tunable in multiple ways. For example, in the case of star polymers the softness is determined by the number of polymeric arms (functionality) anchored to the central site. The same role is played by the aggregation number in block copolymer micelles, for which the ratio between the block lengths is also a “softness parameter”. For dendrimers, softness is controlled by the generation number, the length of the spacer between generations, and the bond stiffness [5]. Finally, microgels are soft provided that their cross-linking is low. If charge is further included, then charged stars, dendrimers or microgels can change their penetrability by pH variations [14, 15].

The range of possibilities described above can be widely extended if multi-component systems of soft particles are considered. Binary hard sphere mixtures and mixtures of hard spheres and linear polymer chains are well established model systems to investigate on a fundamental level effective interactions and phase behavior of condensed matter [16]. In the same way, studies aiming to explore in detail structure, dynamics and phase behavior of soft colloids, their binary mixtures and mixtures with linear polymer are of current interest. In this work, we employ two coarse-grained models of soft binary mixtures in order to investigate a number of aspects of their structure and phase behavior in equilibrium.

This thesis is divided in two parts, each one considering one specific model. The first part, presented in chapters 1, 2, and 3, is devoted to the study of the effects of the addition of small linear (chain) polymer to a fluid of star-like colloids. We focus on the effects of osmotic forces and on the mechanism of depletion, which allow to address some striking phenomena on the rheology of the suspension, and which appear to be sensitive to the chain-star size ratio. Similar behavior observed with ionic microgel particles suggests the universality of the model [17] and therefore its general validity.

In the second part of this work, we focus on bounded, ultrasoft particles, whose interaction potential belongs to the family of the so-called generalized exponential model (GEM), which has been proposed to represent the potential of mean force (i.e. effective interaction) between the centroids of polymeric macromolecules having a low inner monomer concentration. In such cases, the centroids might coincide without overlapping of the constituting monomers. The most remarkable feature of this model is that, upon increasing the density at fixed temperature, the particles begin to overlap forming clusters that can arrange themselves in ordered phases [18]. From the theoretical point of view, the advantage of employing ultrasoft potentials is that the mean-field approximation (MFA) becomes very accurate, so that many complex properties can be calculated in a straightforward fashion within the realm of classical density functional theory (DFT).

This Dissertation is organized as follows: Chapter 1 deals with a full two-component integral-equation approach to describe the demixing transition in the fluid phase of star/linear polymer mixtures. By mapping the mixtures onto a one-component system, we resort to a depletion-like description in chapter 2, where we discuss some unusual features of the depletion potential. Chapter 3 involves a robust comparison to experimental results, showing the accuracy of the coarse-graining procedure for developing effective interactions between star-like micelles and the polymer chains, in a wide range of concentrated mixtures. In chapter 4, we apply density functional theory to study the interfacial and wetting properties of a phase-separating binary GEM fluid within the mean-field approximation. Chapter 5 is devoted to describe the dynamic behavior of the crystal phase of GEM mixtures by means of extensive molecular dynamics simulations. In particular, we investigate the effect of the addition of non-clustering particles on the dynamic scenario of one-component cluster crystals. Finally, in chapter 6 we summarize and draw a number of concluding remarks.

Chapter 1

Demixing transition in star-linear polymer mixtures

In this chapter, we consider the effect of the addition of small polymer chains on the equilibrium structure, as well as on the phase behavior of low- and intermediate-functionality star polymer solutions. By using a recently introduced effective cross interaction between stars and chains, the two component Ornstein-Zernike equation is solved, finding evidence for cluster formation, which is accompanied by a spinodal instability at moderate chain concentrations. The binodal lines are numerically calculated and the dependence of the observed phenomena on functionality, size and concentrations are rationalized by considering the attractive contribution, which is displayed by the effective, chain-modified star-star interaction potential.

1.1 Introduction

Soft matter systems are generally composed by mesoscopic entities with supramolecular architectures and are largely susceptible to external influences. This characteristic allows us to tune the interactions between the different component of the system enriching the panorama of observable phase phenomena as well as the spectrum of possibilities to take control over them. In order to gain some insights into the understanding of trends in the phase behavior of such systems, we may take advantage of coarse-graining procedures which lead to effective interactions between the mesoscopic components, once the microscopic degrees of freedom have been adequately traced out [4, 5, 19].

By following this strategy, most of the physics of colloidal-polymer mixtures can be captured by the depletion mechanism [10, 11, 12, 16, 20, 21, 22, 23, 24, 25]. If a colloidal particle is brought into a non-adsorbing solution of polymers, the latter are depleted in a zone around the colloidal surfaces due to the colloidal-polymer repulsion. The spatial extension of this zone is of the order of the radius of gyration of the polymers. If two colloidal particles are close enough, the two depletion zones overlap, resulting in an effective attraction between them, which can be seen as stemming from an unbalanced osmotic pressure exerted on the colloidal particles by the surrounding polymers. Because the range of the interaction can be tuned, a variety of phase diagrams can be realized [12].

A new range of possibilities emerges when the hard colloids are replaced by soft ones. Star polymer suspensions have developed to be as well characterized, tunable and highly versatile model of soft colloidal systems that do display very rich equilibrium and dynamical behavior [4, 26]. Star polymers (SP) are complex macromolecules consisting of f polymeric chains (arms) chemically anchored to a common core. An interesting aspect of SP is that, depending on their functionality f they constitute intermediate entities between linear polymers ($f = 1, 2$) and sterically stabilized colloids ($f \gg 1$). When the core size is small compared to the length of the chains, the effective interaction $V_{ss}(r)$ between two stars immersed in a good solvent shows a logarithmic dependence on their center-to-center separation for small distances and it cross over to a Yukawa form for larger ones [26].

The phase diagram of SP solutions has special characteristics originating from the ultrasoft nature of their repulsive interaction [26]; for example, it exhibits a critical functionality ($f_c \simeq 34$) below which the system remains fluid at any concentration, whereas for $f > f_c$ the phase diagram exhibits several unusual solid lattices as well as reentrant melting as the density of the system increases [27]. If an attractive potential is superimposed to $V_{ss}(r)$, so that the total resulting potential features the original, logarithmic repulsion for short distances, the system shows a variety of structurally distinct states. By tuning both the amplitude and the range of the attractive contribution, evidence was found for cluster formation, fluid-fluid separation, fluid-solid transitions as well as the formation of a repulsive glass in SP solutions with intermediate functionality ($f \simeq 32$) [28, 29, 30].

From the physical point of view, several mechanisms bringing about an attractive contribution to the star-star interaction potential can be suggested. As previously mentioned, one possibility is the introduction of one smaller component to the system, in this case homopolymer chains. In that case, the attraction develops as consequence of the depletion-like forces, whose properties can be influenced by modifying the size and the concentration of chains. In order to make progress in the description of the effects of the polymer chains on the phase behavior of star polymer solutions, in this work we employ the coarse-grained effective interaction between all composing entities of the mixture, (i.e. star-star, chain-chain, and star-chain interactions) as input for the two component Ornstein-Zernike equation, whose solution provides a good description of the structural properties of the mixture.

The rest of this chapter is organized as follows: In Sec. 1.2 the coarse-graining procedure is described and the full two-component description of the mixture is presented. In Sec. 1.3 the methods employed to determine the structure and thermodynamics of the system are briefly explained. The central part of this work is presented in Sec. 1.4, where the numerical results for the coexistence lines are displayed. Finally, in Sec. 1.5 we summarize and draw our conclusions.

1.2 Coarse-grained model of the mixture

We employ a coarse-graining description of the star-chain mixture, by taking advantage of the effective interaction potential between both components once adequate effective coordinates have been chosen and all the internal degrees of freedom of the macromolecules are integrated out [4, 31]. We suppose both components to be suspended in a good quality solvent, so that the interactions between the same are steric in origin and therefore the effective interactions scale linearly with the thermal energy k_BT, where k_B is the Boltzmann's constant and T the absolute temperature.

For star polymers the position of the central core (on which the arms are anchored) is the natural effective coordinate. The corresponding effective interaction for high enough functionality ($f > 10$) was derived some time ago by using the blob model of Daoud and Cotton (see Appendix A) [32, 33], and its validity has been widely documented both theoretically and experimentally [26]. It can be expressed as

$$\beta V_{ss}(r) = \frac{5}{18} f^{3/2} \begin{cases} -\ln\left(\frac{r}{\sigma_s}\right) + \frac{1}{1+\frac{\sqrt{f}}{2}} & r \le \sigma_s \\ \frac{1}{1+\frac{\sqrt{f}}{2}} \left(\frac{\sigma_s}{r}\right) \exp\left[-\frac{\sqrt{f}}{2\sigma_s}(r-\sigma_s)\right] & r > \sigma_s \end{cases} \tag{1.1}$$

where f and σ_s are respectively the functionality and the corona diameter of the stars, and $\beta = (k_B T)^{-1}$. The quantity $\sigma_s/2$ defines the distance from the center to the outermost of the star according to the Daoud-Cotton model; it marks the crossover between the inner part of the macromolecule (unswollen region), which resembles a semidilute polymer solution, and the outer part, in which loose chains form a local, dilute solution [26]. Extensive comparisons with simulation data have set this scales to $\sigma_s \simeq 1.3 R_g^{(s)}$, where $R_g^{(s)}$ is the radius of gyration of the star [34].

Although there exist several adequate choices for the effective coordinate of the linear chains [4, 35, 36, 37], by choosing the position of the central monomer of the chain we can establish a certain symmetry between multiarm star polymers and linear chains. In this sense, the linear chain can be considered as a star polymer with $f = 2$ whose arms are anchored to the central monomer. In this representation, the effective interaction between two linear chains, whose central monomers are a distance r apart, is given by [38, 39]

$$\beta V_{cc}(r) = \frac{5}{18} 2^{3/2} \begin{cases} -\ln\left(\frac{r}{\sigma_c}\right) + \frac{1}{2\tau^2\sigma_c^2} & r \le \sigma_c \\ \frac{1}{2\tau^2\sigma_c^2} \exp\left[-\tau^2(r^2-\sigma_c^2)\right] & r > \sigma_c \end{cases} \tag{1.2}$$

with $\tau\sigma_c = 1.03$ and σ_c the corona diameter of the chains. The value of τ is chosen in order to guarantee the correct value of the second virial coefficient of a polymer solution. As before, the corona diameter satisfies the relation $\sigma_c \simeq 1.3 R_g^{(c)}$, where $R_g^{(c)}$ is the gyration radius of the linear chain.

In order to have a complete description of the system, we still need to specify the coarse-grained cross interaction between stars and chains. This task has been

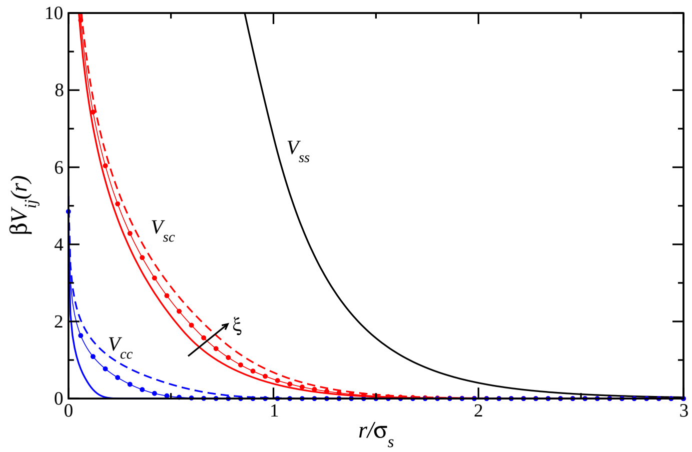

Figure 1.1: Coarse-grained effective interaction potentials given by Eqs. (1.1)-(1.3) for $f = 18$ and size ratios $\xi = 0.1, 0.3, 0.5$.

recently accomplished by using scaling arguments as well as monomer-resolved MD simulations [31]. According to the scaling analysis and similarly to Eqs. (1.1) and (1.2), a logarithmic interaction is obtained for star-chain separations r up to $\sigma_{sc} = (\sigma_s + \sigma_c)/2$; i.e., the cross-diameter for the logarithmic interaction is additive. For larger separations between the star center and the central monomer of the chain, a Flory-like approach was used in which the interaction potential is estimated by the overlap integral between the undisturbed monomer density profiles $\varrho_{s,c}(r)$ of the two interacting objects. In this way the effective cross potential reads as

$$\beta V_{sc}(r) = \begin{cases} -\Theta(f,2)\ln\left(\frac{r}{\sigma_{sc}}\right) + K & r \leq \sigma_{sc} \\ v_0 \int \varrho_s(r')\varrho_c(|\mathbf{r}-\mathbf{r}'|)d\mathbf{r}' & r > \sigma_{sc} \end{cases} \tag{1.3}$$

where $\Theta(f_1, f_2) = \frac{5}{36}\frac{1}{\sqrt{2}-1}((f_1+f_2)^{3/2} - (f_1^{3/2} + f_2^{3/2}))$ and v_0 is an excluded volume parameter. The constants K and v_0 are estimated by requiring that both $V_{sc}(r)$ and its first derivative are continuous functions at $r = \sigma_{sc}$. The density profiles can be evaluated on the basis of the blob model of Daoud and Cotton, resulting [31, 38]

$$\varrho_i(r) = A_i \begin{cases} \left(\frac{\sigma_i}{2}\right)^{-5/3} r^{-4/3} & r \leq \sigma_i/2 \\ \left(\frac{1}{r^2} + 2\kappa_i^2\right)\frac{\zeta_i}{\sigma_i/2}\exp\left\{-\kappa_i^2\left[r^2 - (\sigma_i/2)^2\right]\right\} & r > \sigma_i/2 \end{cases} \tag{1.4}$$

with A_i is a normalization constant and $\zeta_i = (1 + \frac{1}{2}\kappa_i^2\sigma_i^2)^{-1}$. The parameter κ_i is set by $\kappa_i\sigma_i = 1.27$ in order to fit the theoretical profile, Eq. (1.4), to the MD simulation results. We emphasize that the general scheme used to evaluate $V_{sc}(r)$ is consistent for arbitrary functionality f and size ratio $\xi = \sigma_c/\sigma_s$, independently of the degree of polymerization of the star and the chain; the only dependence on them comes implicitly through σ_s and σ_c. In Fig. 1.1 a comparison between the three effective pair potentials V_{ss}, V_{sc} and V_{cc} is shown for $f = 18$ and several size ratios.

1.3 Bulk structure and phase diagram

1.3.1 Fluid structure

The structural information of the mixture was gained by solving the two component Ornstein-Zernike (OZ, see Appendix B) equations with help of the Rogers-Young (RY) closure, which has been showed to be reliable for one component SP solutions as well as for mixtures of SP and hard-spheres colloids [27, 40]. Briefly, for a ν-component mixture with partial densities ρ_i of the i-th specie, the fluid pair structure is fully described by solving $\nu(\nu+1)/2$ coupled OZ equations connecting the total correlation functions $h_{ij}(r)$ with the direct correlation functions $c_{ij}(r)$, $i, j = 1, \ldots, \nu$. In Fourier space the OZ relations read as

$$\hat{\mathbf{H}}(k) = \hat{\mathbf{C}}(k) + \hat{\mathbf{C}}(k) \cdot \hat{\mathbf{D}} \cdot \hat{\mathbf{H}}(k) \tag{1.5}$$

with matrix elements $[\hat{\mathbf{H}}(k)]_{ij} = \hat{h}_{ij}(k)$, $[\hat{\mathbf{C}}(k)]_{ij} = \hat{c}_{ij}(k)$ and $[\hat{\mathbf{D}}]_{ij} = \rho_i\delta_{ij}$. Here, $\hat{h}_{ij}(k)$ and $\hat{c}_{ij}(k)$ denote respectively the Fourier transform of the pair correlation function $h_{ij}(r)$ and the direct correlation function $c_{ij}(r)$.

In order to have a complete solution of Eq. (1.5), it is necessary to provide $\nu(\nu+1)$ additional *closure equations* between the total and the direct correlation functions. Particularly, the Rogers-Young closure for a multicomponent system is given by

$$g_{ij}(r) = \exp\left[-\beta v_{ij}(r)\right] \left\{1 + \frac{\exp\left[\chi_{ij}(r) f(r)\right] - 1}{f(r)}\right\} \tag{1.6}$$

where $g_{ij}(r) \equiv h_{ij}(r) + 1$, $\chi_{ij}(r) = h_{ij}(r) - c_{ij}(r)$, and $v_{ij}(r)$ are the pair interaction between species i and j ($i, j = s, c$ for stars and chains respectively). The auxiliary *mixing* function $f(r) = 1 - \exp[-\alpha r]$ is introduced to enforce thermodynamic consistency of the total isothermal compressibility by matching the value of the parameter α [41].

We determined the pair correlation functions of the star-chain mixtures by calculating the three static structure factors $S_{ij}(k) = \delta_{ij} + \sqrt{\rho_i \rho_j}\hat{h}_{ij}(k)$ once we had numerically solved the OZ-RY equations, Eqs. (1.5) and (1.6), through an iterative Picard method. This procedure was carried out for mixtures characterized by functionalities $f = 18, 24, 32$ and size ratios $\xi = 0.1, 0.3, 0.5$ covering a wide range in the density plane (ρ_s, ρ_c). For some combinations of parameters, we additionally performed standard NVT-Monte-Carlo simulations as a check for the results from the OZ-RY calculations.

1.3.2 Binodal lines

Based on the structural information obtained by solving the OZ-RY equations, we can access in principle to the complete information concerning the thermodynamics of the system. In particular, in order to determine the binodal lines, it suffices to consider the concentration structure factor, $S_{con}(k)$, which is defined as [40, 42, 43, 44]

$$S_{con}(k) = x^2(1-x)S_{ss}(k) + x(1-x)^2 S_{cc}(k) - 2\left[x(1-x)\right]^{3/2} S_{sc}(k) \tag{1.7}$$

with $x = \rho_c/(\rho_s + \rho_c)$ the partial concentration of chains. With this definition, the link between the structural information and the thermodynamics of the system is provided by the sum rule

$$S_{con}(k \to 0) = k_B T \left[\frac{\partial^2 g(x, P, T)}{\partial x^2}\right]^{-1}, \tag{1.8}$$

where $g(x, P, T) = G(x, N, P, T)/N$ is the Gibbs free energy per particle and P denotes the pressure of the mixture [42]. Once $S_{con}(k)$ is known as a function of x for constant pressure and temperature, the Gibbs free energy can be calculated by integrating (1.8) twice, as described in [40, 44]. If $g(x, P, T)$ has concave parts as a function of x for some x-region, the mixture features a fluid-fluid demixing transition and the corresponding phase boundaries can be calculated by means of the

Maxwell's common tangent construction, which guarantees that the partial chemical potentials of every component have the same value on both coexisting phases. As it is performed on an isobar, and for fixed temperature, the pressure and the temperature are also the same for both phases and therefore all conditions for phase equilibrium are fulfilled.

1.4 Results

1.4.1 Chain-modified effective star-star interaction

In order to gain a first insight of the effect of adding linear chains to a SP solution, we can carry out a second coarse-graining procedure and do describe the mixture in first approximation as an effective one-component SP solution. Under this view, the stars are considered to interact not through $V_{ss}(r)$ given by Eq. (1.1), but through a new chain-modified effective potential $V_{\text{eff}}(r)$ in which the degrees of freedom of the chains have been traced out. By construction, this chain-modified interaction potential leaves the correlation functions $g_{ss}(r)$ and $S_{ss}(k)$ between the stars invariant.

One possibility to achieve this mapping is to use the inversion of the full, two component solution for the radial distribution function in the limit of low star density [41]. Once the star-star radial correlation function $g_{ss}(r)$ is known by solving the OZ equations with the Rogers-Young closure, the effective star-star potential can be estimated by means of

$$\beta V_{\text{eff}}(r) = -\ln\left[g_{ss}(r; f, \xi, \rho_s \to 0, \rho_c)\right]. \tag{1.9}$$

In Fig. 1.2 we show the results for the effective star-star potential from the inversion procedure for different values of f and ξ. As can be seen, the increase in ρ_c reduces the range of repulsion and eventually yields to the rise up of an attractive well in $V_{\text{eff}}(r)$ as a consequence of a typical depletion mechanism when the stars are close enough. This effect is more pronounced as the functionality f or the size ratio ξ increase and it becomes more difficult to chains to occupy the inter-star space for a given r.

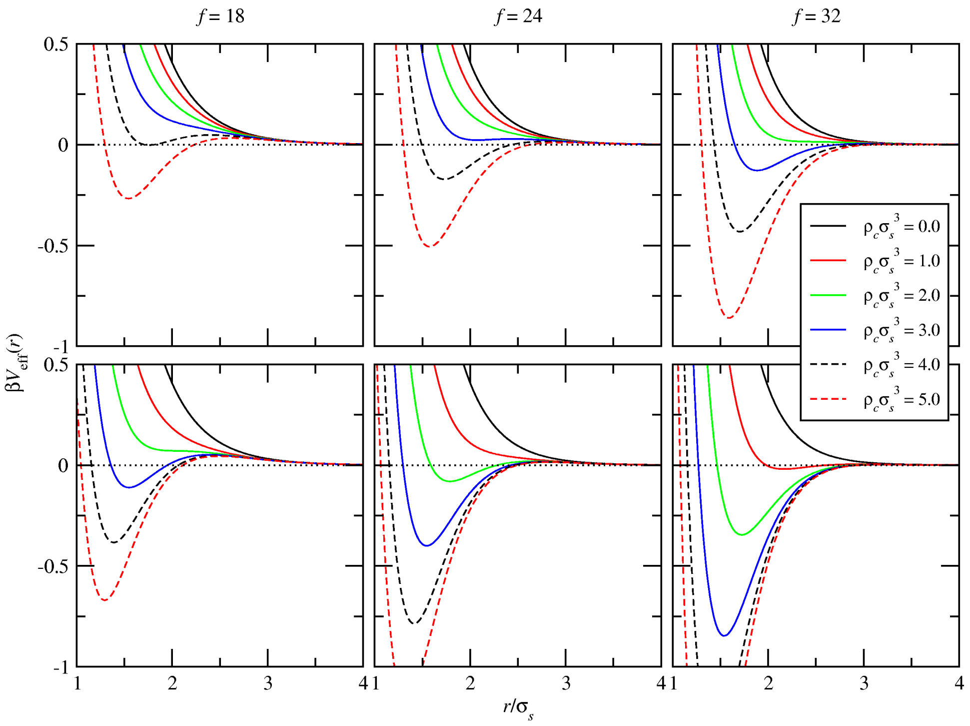

Figure 1.2: Chain-mediated effective star-star potential as obtained by inversion of the OZ equation. The influence of increasing the chain density is shown for functionalities $f = 18, 24, 32$ and size ratios $\xi = 0.1$ (upper row) and $\xi = 0.5$ (bottom row).

For all combinations of parameters considered, the effective potential $V_{\rm eff}(r)$ remains repulsive at large star-star separations. This fact induces the appearance of a repulsive hump together with the attractive well at intermediate distance ($r \gtrsim 2\sigma_s$), as a consequence of the interaction and correlations between the depletant particles; this effect is also present in highly asymmetric hard-sphere mixtures [45]. As can be seen in Fig. 1.2, the height of the repulsive hump decreases by increasing f. This is a direct consequence of the functional form of the star-star interaction $V_{ss}(r)$, which decays faster at large distances as the functionality becomes larger, see Eq. (1.1).

Some models of effective potentials featuring this *well-and-shoulder* form have been used in order to explain the formation of finite, stable clusters in soft matter systems [46, 47, 48, 49, 50, 51]. These structures can be built up due to the tendency

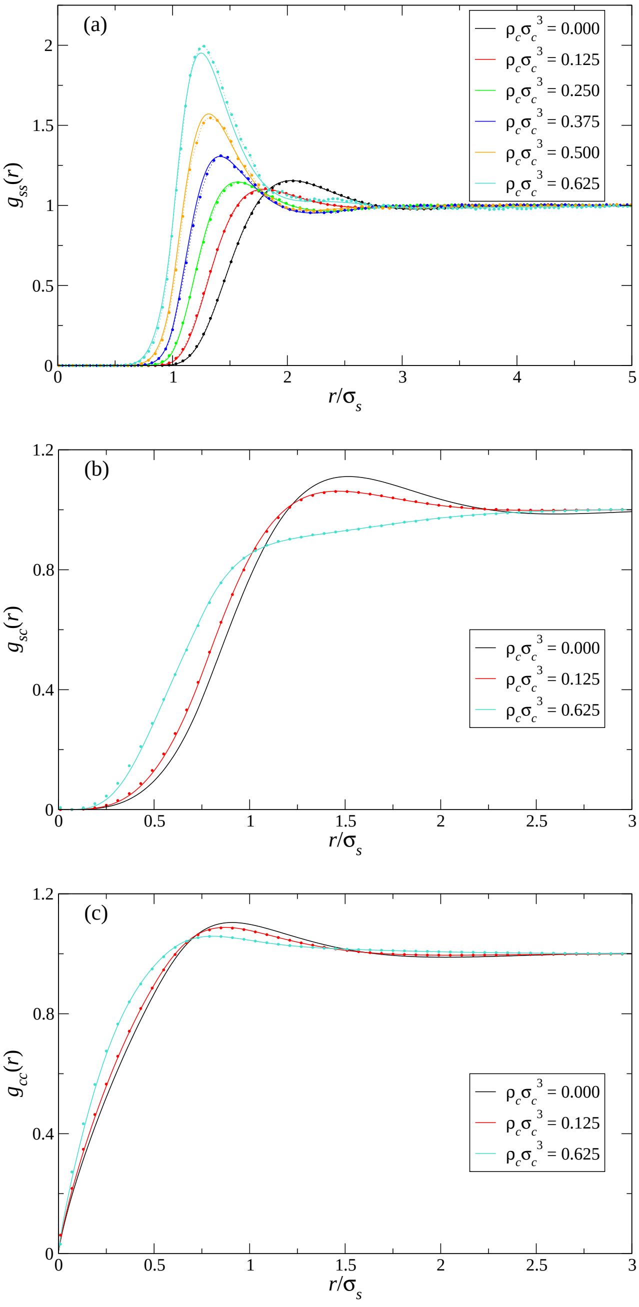

Figure 1.3: Partial radial distribution functions of the mixtures for different chain densities as obtained by solving the OZ equations with the RY closure. The system is characterized by functionality $f = 18$, size ratio $\xi = 0.5$ and star density $\rho_s\sigma_s^3 = 0.1$. The filled circles correspond to results from Monte-Carlo simulations.

of the attractive well to induce particle aggregates whose size is thereafter limited by the repulsive barrier preventing the growth of an infinite cluster. If such a barrier is rather low or narrow, the system would be driven to develop long-range fluctuations upon an increase of the chain concentration and therefore a fluid-fluid demixing transition of the two component mixture will be favored without a previous occurrence of clusters, as in colloid-polymer mixtures [16].

1.4.2 Structure of the mixture

We can describe the structure of the binary mixture either by the three partial radial distribution functions $g_{ij}(r)$ in real space or by the three partial static structure factors $S_{ij}(k)$ in wavenumber space. In Fig. (1.3) we present the evolution of the partial radial distribution functions for dilute star polymer solutions of functionality $f = 18$ and chain-to-star size ratio $\xi = 0.5$ upon the increase of the chain concentration.

Although for very small chain concentration $g_{ss}(r)$ has a relative weak peak at $r_0 \sim \rho_s^{-1/3}$, it rapidly develops a pronounced peak at smaller distance r_c when ρ_c increases further. This is a first indication of clustering of stars, which are brought together because the attraction induced by the smaller chains, since the distance r_c is set by the minimum in the effective potential $V_{\text{eff}}(r)$. By further increase of chain density the depression in $g_{ss}(r)$ at distance $2.0 < r/\sigma_s < 2.5$, which is directly connected to the repulsive hump in $V_{\text{eff}}(r)$, becomes less pronounced and eventually disappears. This effect can be explained because at high enough chain densities the strength of the repulsive hump goes down and it can no more limit the size of the cluster.

The previously described scenario can be further elucidated by considering the star-star structure factors $S_{ss}(k)$. In Fig. 1.4 we consider the structure factors for $f = 18$ and $\xi = 0.5$. As can be seen, $S_{ss}(k)$ develops a double-peak structure with two peaks corresponding to two independent length scales. Whereas a *particle peak* shows from $k\sigma_s \sim 4$ at zero chain density up to $k\sigma_s \sim 6$ for higher one, a *cluster pre-peak* appears at smaller wavenumber $k\sigma_s \sim 1.5$, suggesting the formation of finite clusters. The size growth of such clusters as well as the increase in the inter-cluster separation are then indicated by the shifting of the position of the cluster

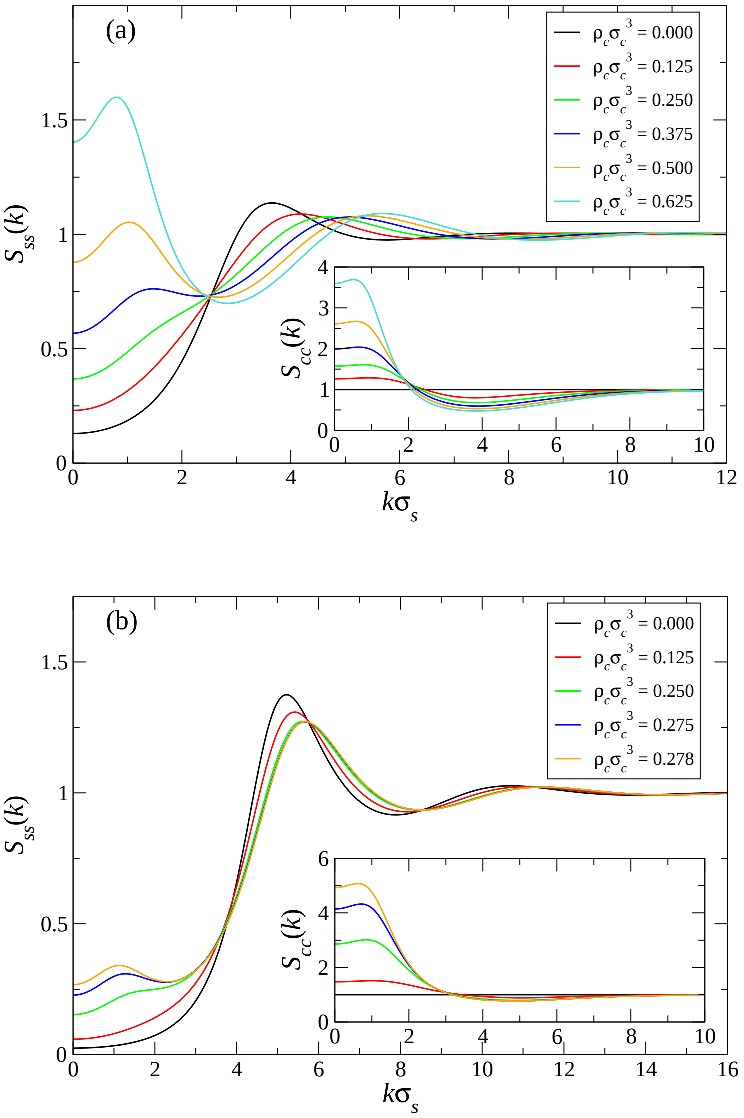

Figure 1.4: Star-star structure factors at densities (a) $\rho_s\sigma_s^3 = 0.1$ and (b) $\rho_s\sigma_s^3 = 0.4$ by increasing the chain density. The star functionality and size ratio are respectively $f = 18$ and $\xi = 0.5$. Corresponding chain-chain structure factors are shown in the insets.

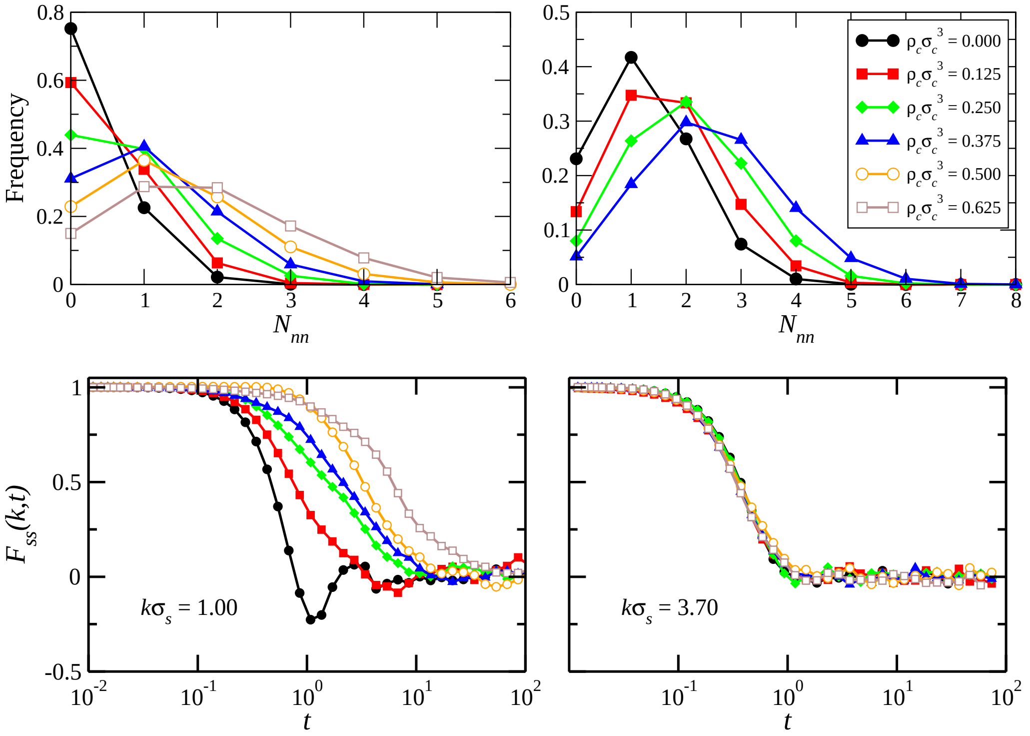

Figure 1.5: Top: Distribution of the number of star-star nearest-neighbors for $f = 18$, $\xi = 0.5$ and different chain densities. The star densities are $\rho_s\sigma_s^3 = 0.1$ (left) and $\rho_s\sigma_s^3 = 0.2$ (right). Bottom: Star-star coherent scattering function for $\rho_s\sigma_s^3 = 0.1$ at wave vectors $k\sigma_s \cong 1.00$ and $k\sigma_s \cong 3.70$, i.e., around the cluster and particle peaks. Legend is the same for all figures.

pre-peak to lower k-values. At the same time, the value of $S_{ss}(k = 0)$ increases demonstrating that the system is approaching the spinodal line and therefore, for high enough chain density, the fluid-fluid demixing transition will take place. This fact is confirmed by looking at the behavior of the limit of long wavelength of the chain-chain structure factor $S_{cc}(k = 0)$ as shown in the insets of Fig. 1.4.

As mentioned above, the particle peak of $S_{ss}(k)$ shifts to larger k as ρ_c increases, pointing out the distance between (star-star) nearest neighbors decreases. In addition, the height of the peak goes down but, upon an further increase of ρ_c, it slightly increases (see Fig. 1.4), which is an indication of the increase of the average number of nearest-neighbors. That this is indeed the case is demonstrated

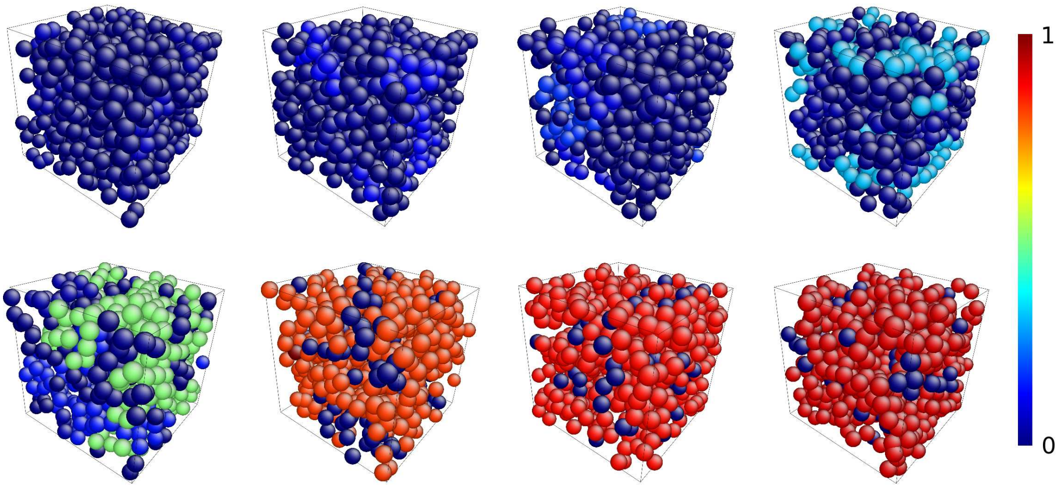

Figure 1.6: Simulation snapshots for $f = 18$, $\xi = 0.5$, $\rho_s \sigma_s^3 = 0.2$ and different chain densities. Color bar measures the fraction of connected stars in relation to their total number in the simulation box. From left to right and top to bottom, $\rho_c \sigma_c^3$ was increased from 0 to 0.4375 in steps of 0.0625. For sake of clarity, only stars are shown.

in Fig. 1.5, which displays the distribution of the number of (star-star) nearest-neighbors (N_{nn}) extracted from MD simulation snapshots. Two stars are considered as neighbors if the distance between them is smaller than $R_{\mathrm{cutoff}} = 1.5\sigma_s \cong 2R_g^{(s)}$. On the other hand, the size of the larger structure, i.e., the one corresponding to the cluster peak k, is measured by the number of connected stars. Following [52, 53], two stars are connected, i.e., they belong to the same cluster, if they are themselves nearest-neighbors and simultaneously nearest-neighbors of a third star. In Fig. 1.6 representative snapshots of the simulation box are presented, showing the number of connected particles. As can be seen, clusters of connected stars coarsen as the chain density increases and form a transient percolating network, as confirmed by looking at dynamical properties. For example, the coherent scattering function $F_{ss}(q,t)$ (see Appendix C) completely relaxes pointing out the star dynamics is ergodic at both the particle and the cluster scales (see Fig 1.5). This picture is completely analogous to the one found in colloid-polymer mixtures [53, 54]. However, there is an important difference; since there is no glass transition in pure suspensions of

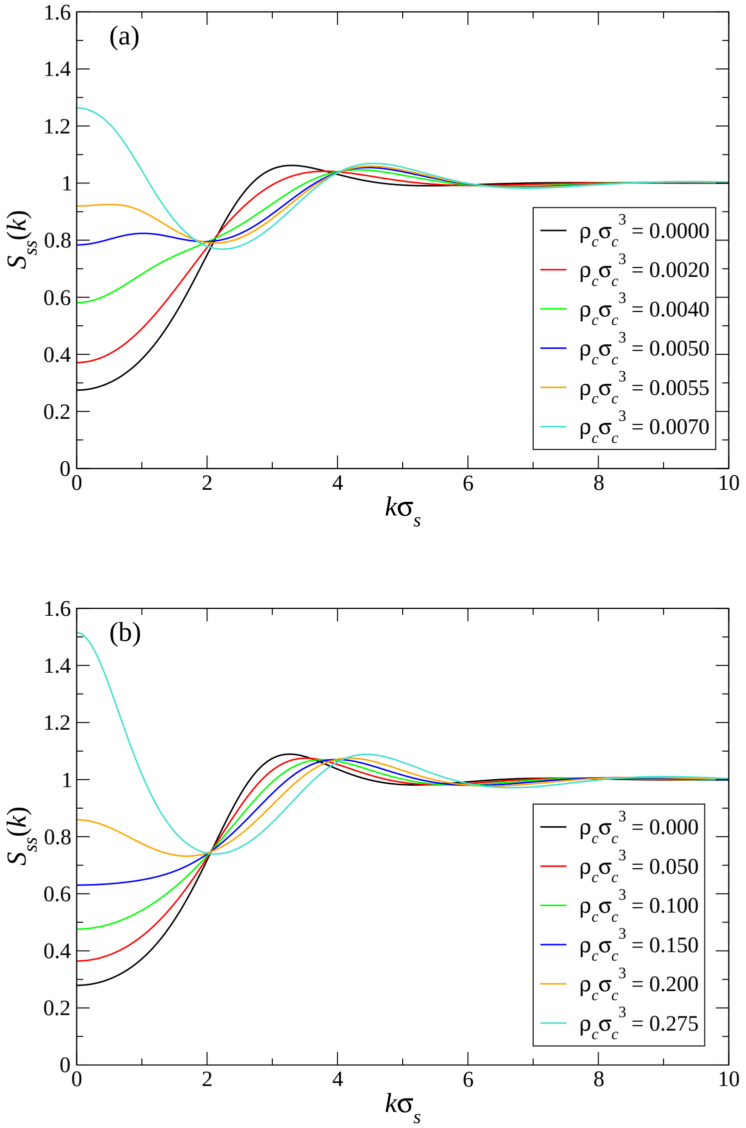

Figure 1.7: Star-star structure factors at star density $\rho_s\sigma_s^3 = 0.05$ for (a) $f = 18$, $\xi = 0.1$ and (b) $f = 32$, $\xi = 0.5$. By increasing the chain density ρ_c the partial structure factors grow for $k \to 0$, as indication the system is approaching to the demixing spinodal.

low-functionality stars, the percolating network in the mixture never undergoes a gel transition and therefore the spinodal decomposition will always take place at sufficiently high chain density. A deeper analysis of the dynamical properties will be subject of a future investigation.

Resuming back to the features of the structure factors, we have found a similar situation by decreasing the size ratio ξ, as shown in Fig. 1.7(a) for $f = 18$ and $\xi = 0.1$. However, in this case the position of the cluster pre-peak goes faster to $k = 0$ as ρ_c increases and the Lifshitz line for $S_{ss}(k)$ (where the local minimum of the structure factor at $k = 0$ turns into a maximum) is reached. On the other hand, by increasing the star functionality, the cluster pre-peak disappears and the system is driven directly to the demixing transition as ρ_c increases, as is shown in Fig. 1.7(b) for $f = 32$ and $\xi = 0.5$. In this way, we can state that the system at hand displays cluster formation as a precursor stage for the demixing transition for low enough functionality, $f \lesssim 24$. A more detailed description of this behavior will be discussed below.

1.4.3 Demixing transition

According to the previous discussion, we have good evidence that a demixing transition takes place in the studied system for certain ranges of chain densities. We can give a quantitative description of this transition by determining the phase boundaries as explained in Sec. 1.3.2. The results for the demixing binodal lines in the (ρ_s, ρ_c)-plane are presented in Fig. 1.8 for functionalities $f = 18, 24, 32$ and size ratios $\xi = 0.1, 0.2, 0.3$. In addition to the coexistence lines (thick lines) we show a few tielines (thin lines) connecting the coexisting star-rich and star-poor phases. By taking into account the tielines we also present a rough estimate of the position of the critical points in the same figure.

As can be seen, for a given size ratio ξ the binodal lines move toward lower star densities upon increasing the functionality f, meaning that the chains are more efficient depletants for “harder” stars. If we consider an extrapolation to mixtures in the limit $f \to 2$, this trend is in agreement with the fact that in this limit, the critical point lies beyond the overlapping concentration of stars [55]. On the other hand,

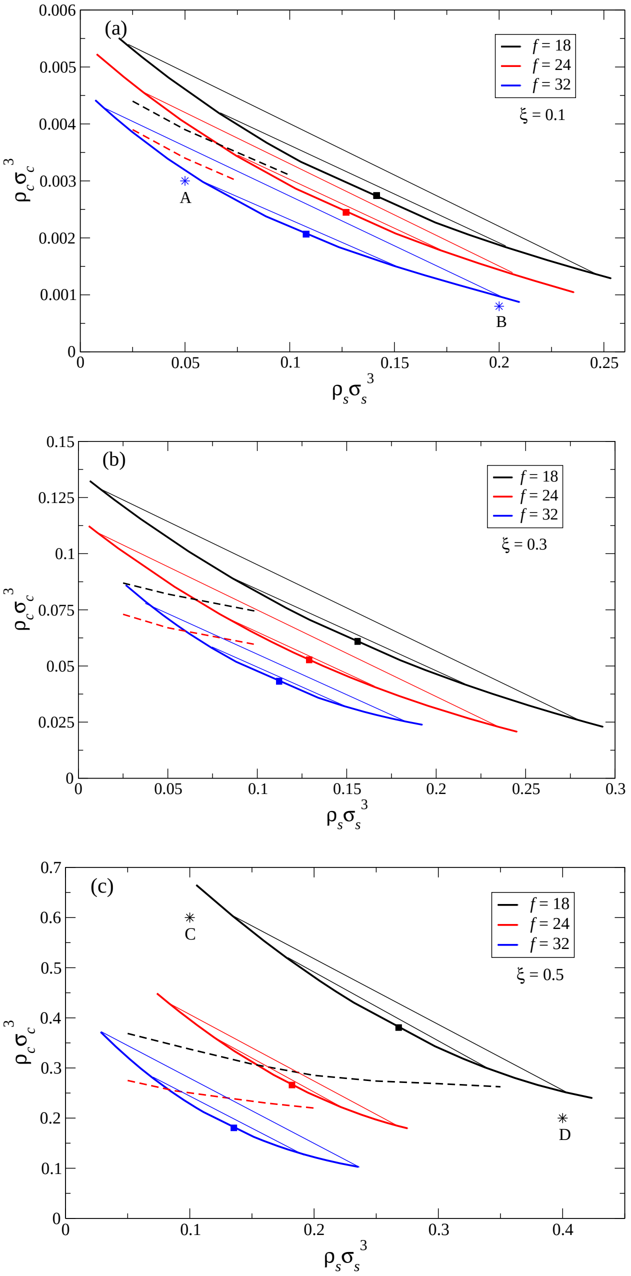

Figure 1.8: Demixing binodal lines for different values of star functionality f and size ratio ξ. The thin lines represent tie lines, whereas the filled squares correspond to the estimated positions of the respective critical points. The thick dashed lines indicate the *cluster lines* for $f = 18$ and $f = 24$.

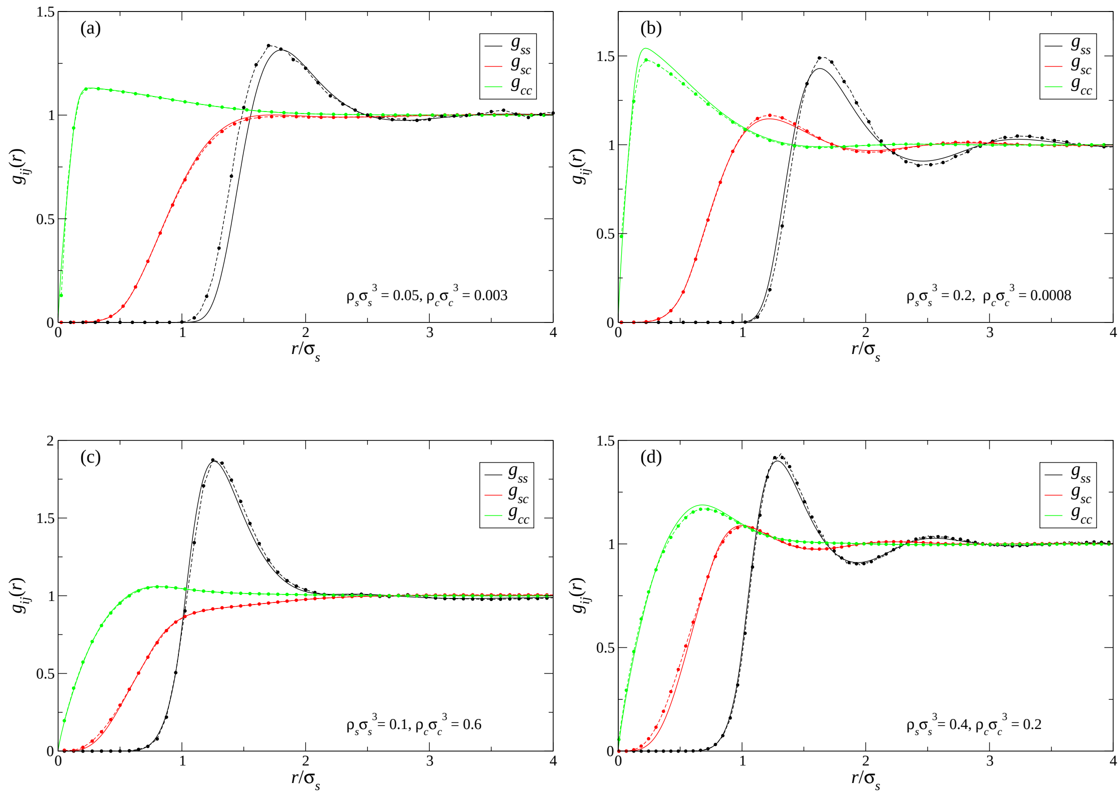

Figure 1.9: Comparison of the correlation functions obtained by solving OZ-RY equation (continuous lines) and those from Monte-Carlo simulations (dots) for (a)-(b) $f = 32$, $\xi = 0.1$ and (c)-(d) $f = 18$, $\xi = 0.5$. The (ρ_s, ρ_c)-pairs indicated in each panel correspond respectively to the points indicated by asterisk $(*)$ and marked as A, B, C and D in Fig. 1.8.

as ξ increases for fixed f, the coexistence lines shift to higher star densities, which is similar to that found in colloid-polymer mixtures [16]. However in the system at hand, such shift becomes comparatively smaller for larger f. This fact can be associated with the possibility to form finite clusters of stars when the functionality is sufficiently small, stabilizing the system against demixing at a given chain density.

Before we discuss that point, it is worth to take a look at the accuracy of the solution of the OZ-RY equations for the system at hand. In order to carry out a comparison, a number of Monte-Carlo simulations was performed for different combinations of densities, functionalities and size ratios. Some comparisons were already presented in Fig. 1.3 concerning the evolution of the radial distributions functions at fixed star density ρ_s by increasing the chain density ρ_c. In Fig. 1.9, a few representative comparisons for (ρ_s, ρ_c) pairs in the neighborhood of the binodal lines are shown for parameter combinations $(f = 32, \xi = 0.1)$ and $(f = 18, \xi = 0.5)$. It can be ascertained that the agreement of the two methods is quite good and, as the size asymmetry decreases, the discrepancies tend to disappear completely. Therefore, the OZ-RY method gives quite reliable results for the structural information, and consequently for the thermodynamics, of the system at hand, especially for low size asymmetry.

Concerning the stabilization of the mixture against the demixing transition by formation of finite clusters, whereby the emergence of a macrophase separation is precisely defined through the divergence of the structure factors $S_{ij}(k)$ at $k = 0$, cluster formation in a thermodynamically stable fluid is not associated with any accompanying phase transition. In this way, we have to resort the evidence about the occurrence of a cluster in some (arbitrary) structural criteria [28]. As previously discussed, in the case at hand the existence of a cluster is indicated by identifying a pre-peak in the star-star structure factor $S_{ss}(k)$. Following Ref. [51], in which the fluid phase of double-Yukawa (attractive/repulsive) systems was studied, a *cluster line transition* can be defined by determining the necessary chain density to generate an inflection point in the structure factor $S_{ss}(k)$ from which the pre-peak rise up. The cluster lines we have obtained by using this criterion are shown in Fig. 1.8 as dashed lines. Qualitatively speaking, we can consider the region between the dashed line and the binodal in Fig. 1.8, as a region of stability of the clusters. As can be seen in Fig. 1.8, for a given ξ the extension of the cluster region decreases as f increases, even vanishing at $f = 32$. As we mentioned above, in the frame of the effective star-star potential that effect is associated to the decrease of the range of the repulsive contribution to $V_{\text{eff}}(r)$ as f increases, rendering the repulsive hump narrower. On the other hand, for $f \leqslant 24$ the stability region increases for larger size ratio ξ, because the attractive well of $V_{\text{eff}}(r)$ becomes deeper as ξ grows for a fixed number of chains, whereas the range of the attraction remains practically the same, as can be seen in Fig. 1.2. Summarizing, for larger size ratio and lower functionality, the well-and-shoulder structure of $V_{\text{eff}}(r)$ appears to be well supported for a larger range of chain density, and therefore the cluster region gets wider.

The same phenomenology has been also described in one-component star polymer suspensions with additional Fermi-like attraction potential [28, 29] as well as for two-Yukawa systems upon variations of the repulsion and attraction ranges and strengths [51]. Given some adequate repulsive contribution, these systems sequentially reach the cluster line (as defined above) at first, then the Lifshitz line and finally the spinodal line by increasing the attraction strength. On the other hand, by changing the parameters describing the repulsive contribution, the cluster line can be suppressed and the system can be directly driven to the phase separation.

The case $f = 18$ and $\xi = 0.5$ is particular compared to the other ones, as far as the width of stability of the cluster-region is concerned (see Fig. 1.8). For this parameter combination, the star-chain interaction is soft enough to allow the chains to occupy the inter-star region as ρ_c is increased. As can be seen in Fig. 1.3(b), this fact is corroborated by the increase of the star-chain radial correlation function $g_{sc}(r)$ around $r \simeq \sigma_{sc} = (\sigma_s + \sigma_c)/2$ as the chain density grows. This enhanced chain penetration to the star interior appears at the expense of a decrease of the chain number around the position of the peak of the star-star correlation function $g_{ss}(r)$ as Fig. 1.3(a) shows; in other words, less chains remain in the region around the stars to osmotically compress them together. Although this effect is present for all the used functionalities provided the size ratio is relatively large, $\xi = 0.5$, it is much more pronounced for $f = 18$. For this functionality, it appears that a considerable fraction of the chains can be brought close enough to the stars, so that the regime where the cross interaction potential $V_{sc}(r)$ displays a logarithmic form is reached, see Eq. (1.3). In pure, dense star polymer solutions, the crossover of the interaction from a Yukawa to the logarithmic form causes the structure factor to show an anomalous behavior, and it also allows the system to remain fluid for large densities when $f \lesssim 32$ [56]. Taking this into account together with the behavior of $g_{ss}(r)$ and $g_{sc}(r)$, we can conclude that, at high enough chain density, the fraction of the chains penetrating the star prevent the growth of the depletion attraction arising from the excluded chains, thus hindering the already formed clusters from further rapid aggregation and consequently slowing down the phase separation process.

Finally, we emphasize a novel, unusual characteristic of our system, pertaining to the range of the chain-induced depletion attraction. For both binary hard-spheres mixtures and colloid-polymer mixtures, it is a well established fact that the range of the depletion interaction increases as the size ratio does [6, 45]. As briefly mentioned above, the attractive component of the chain-modified star-star effective interaction $V_{\text{eff}}(r)$ in the system at hand, displays an unusual feature for depletion-like potentials, namely its range is insensitive to the size of the depletant particles. In fact, this attractive component can be well-described by a Fermi-like potential [28, 29], whose length scales show a very weak dependence not only on the chain density ρ_c but also on the size ratio ξ, whereas its strength grows rapidly with ρ_c. This unusual behavior can be attributed to the ultra-soft nature of the considered interactions and will be analyzed in the following chapter.

1.5 Concluding remarks

We studied the structural and phase properties of star- and linear polymer mixtures by using a coarse-grained model for the interactions between the different species forming the system. We found evidence that addition of linear polymers to star polymer suspensions with small to intermediate functionality ($f \leq 32$) can lead to star cluster formation and, because the star-chain interaction is sufficiently repulsive, to bring about regions of instability towards a fluid-fluid (demixing) transition. The calculated coexistence data are very encouraging with respect to experimental realization: the binodal lines lie well below the overlap concentrations of both stars and chains, where the effective pair potential picture should bring a valid description of the mixture. Since there is a region in the (ρ_s, ρ_c)-plane where unstable clusters can be formed, which eventually aggregate, an increase of the characteristic forward scattering intensity and hydrodynamic radius [50] could be expected. The rate of increase as a function of the system parameters can be used to characterize and control the transition.

We have rationalized the phase behavior of the mixture by considering the chain-modified star-star effective interaction $V_{\text{eff}}(r)$, which features a short-range attraction and a large-range repulsive contributions. Since the strength of the attractive contribution to $V_{\text{eff}}(r)$ can be modified by changing the size ratio ξ and the chain density ρ_c, and the range of the repulsive tail is fixed by f, this kind of mixtures is a very flexible and tunable system. In previous works, the attractive contribution to $V_{\text{eff}}(r)$ was considered to be a Fermi-like potential [28, 29]. Since it is possible to relate the parameters characterizing that potential to physical parameters f, ξ and ρ_c, the star-chain mixtures open a door to the experimental verification of the predicted equilibrium and dynamical behavior of such systems [28, 29], as well as to its critical properties [57].

Future directions should focus on the dynamics of the mixture as well as the regime of high star densities, for which the Fermi-like model for attraction predicts crystal structures, which are not supported by the ultrasoft repulsion alone for low functionality. In this respect, a more quantitative understanding of the unusual properties of the depletion-like potential due to the chains will be necessary. On the other hand, the intermediate functionality regime ($32 \lesssim f \lesssim 50$) can be considered, in order to study the effect of the chains polymers on the reentrant melting featured in one-component systems [27].

Chapter 2

Depletion potential in ultrasoft mixtures

The aim of this chapter is to study the influence of addition of polymer chains on the effective interaction between star polymers, as model for depletion potential in ultrasoft mixtures. The effects of size ratio and chain polymer concentration on the chain-modified star-star interactions at good (athermal) solvent conditions are investigated. For both hard sphere mixtures and colloid-non adsorbing polymer mixtures the range of the depletion interaction increases with the size ratio. For the systems at hand, the range of the depletion potential is insensitive to the size of the depletant polymer. The physical origin of this and associated effects, as well as a mapping of the mixtures onto a one-component system are discussed.

2.1 Introduction

The capability to tune the interactions between colloidal particles from short-range repulsions to short-range attractions has become a valuable tool for the study of fundamental and practical problems in soft matter physics. The question is of high relevance to recent and ongoing work on cluster formation and stability [58], dynamical arrest [59] and gelation [53]. In most cases, these interactions are effective in the sense that microscopic degrees of freedom have been averaged out through a coarse-graining procedure [4]. A typical example of that is the introduction of the depletion potential V_{dep}. In the scope of the coarse-grained approaches, the best known depletion model is that of Asakura-Oosawa (AO), in which both range and strength of V_{dep} can be precisely tuned by varying the polymer-to-colloid size ratio and the polymer concentration [10, 11]. By using this simplified, one-component description, many insights have been gained about the equilibrium phase behavior of colloid-polymer mixtures [16, 60]. However, when interacting polymers are considered, the AO model breaks down as result of the sensitivity of V_{dep} to variations in the direct interactions among the components of the system [61, 62]. It is to be expected that a new range of possibilities emerges when the big hard colloids are replaced by soft ones; however, the AO-model is still the paradigm serving as the guiding prototype in this context.

In recent years, the study of particles interacting via soft potentials, which are realized by, for example, micelles, star polymers, dendrimers, or microgel particles, has gained a lot of attention. In analogy with hard-core colloidal systems, the depletion mechanism has been also introduced to rationalize the effect of short-range attractions on suspensions of soft particles [63, 64, 65]. For example, in block copolymer micellar suspensions, depletion forces affect not only the inter-micellar packing but also the intra-micellar one, and they can also induce the disordering of ordered microstructures [66, 67]. In multiarm star polymer solutions [26, 27, 68], osmotic forces due to the addition of small linear polymers lead to formation of thermodynamically stable star clusters at the low star density regime, while at high star density they cause melting of the dense glassy state [49, 50]. These findings provide physical mechanisms for tailoring the equilibrium and flow properties in a wide range of ultrasoft particle mixtures. From the theoretical point of view, they motivate us towards a better understanding of the depletion potential for such systems. In this chapter we consider the effective interaction between highly versatile model of soft colloids, i.e., star-polymers, resulting after the addition of small polymer chains by using coarse-grained representations of their mutual interactions [26, 34, 35, 36, 37].

2.2 Model

In its simplest realization, the system of interest consists of $N_s = 2$ star polymers and N_c chains enclosed in a volume V, which define the partial number densities $\rho_s = N_s/V \to 0$ and $\rho_c = N_c/V$. The star-chain size ratio is given by $\xi = \sigma_c/\sigma_s$ where σ_i is the so-called corona diameter, which scales as $\sigma_i \simeq (4/3)R_g^{(i)}$ $(i = s, c)$, with $R_g^{(i)}$ the corresponding radius of gyration [34]. As in the previous chapter, we consider the center of the stars and the middle monomer of the chains as effective coordinates, so that the components interact through the effective potentials given by Eqs. (1.1)-(1.3), displaying an ultrasoft logarithmic dependence at short distances and crossing over to an exponentially decay at large ones. We want to remark that the general scheme used to evaluate the effective potentials is consistent for arbitrary f and size ratio ξ, independently of the degrees of polymerization of the star and the chain; the only dependence on those comes implicitly through σ_s and σ_c.

We are interested in the effective interaction between star polymers immersed in a bath of smaller chains. From this perspective, the stars can be described by a renormalized, chain-modified effective potential $V_{ss}^{\mathrm{eff}}(r)$ in which the degrees of freedom of the chains have been traced out. The simplest way to achieve this mapping is to employ the inversion of the full, two component solution for the star-star radial distribution function $g_{ss}(r)$ in the limit of low star density [41]. Once $g_{ss}(r)$ is known by solving the Ornstein-Zernike (OZ) equations with the Rogers-Young closure, the effective star-star potential can be calculated as $\beta V_{ss}^{\mathrm{eff}}(r) = -\ln\left[g_{ss}(r; f, \xi, \rho_s \to 0, \rho_c)\right]$. By construction, this chain-modified interaction potential leaves the partial correlation functions $g_{ss}(r)$ and the structure factor $S_{ss}(k)$ between the stars invariant.

2.3 Results

In Fig. 2.1 some results for the effective star-star potential from the inversion procedure are displayed for different values of ξ. As expected, the increase in ρ_c reduces the range of repulsion and eventually leads to the emergence of an attractive well in $V_{ss}^{\mathrm{eff}}(r)$. It can be seen that, contrary to the AO-case, the depth of attractive well behaves non-monotonically with the size of the chains: at high enough but equal

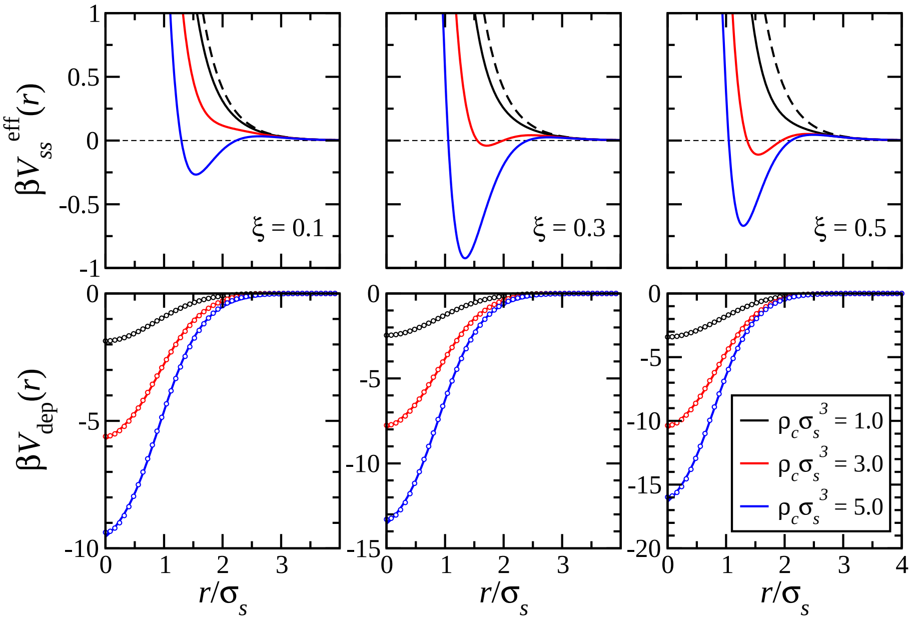

Figure 2.1: Upper row: Chain-mediated effective star-star potential as obtained by inversion of the OZ equation with $f = 18$ for different size ratios and chain densities. The pure star-star potential $V_{ss}(r)$ is represented by the dashed lines. Bottom row: Corresponding depletion potentials are indicated by open symbols while the continuous lines result from fitting to Eq. (2.3).

chain density the well becomes deepest at the intermediate size ratio, while, at the same time, its minimum appears to be located roughly at the same position independently of ξ. This feature is also noticeable when we focus our attention to the induced depletion potential $V_{\mathrm{dep}}(r) = V_{ss}^{\mathrm{eff}}(r) - V_{ss}(r)$: for all conditions considered in Fig. 2.1, $V_{\mathrm{dep}}(r)$ displays the same qualitative behavior irrespective of the size and concentration of the depletant polymers. The range of $V_{\mathrm{dep}}(r)$, Δ_{dep}, changes very little with ξ, which is counter-intuitive, as it would be normally expected that Δ_{dep} grows with the size ratio (and, in the case of the AO-model, in a linear fashion).

To check the validity of these results, we use as an alternative approach the superposition approximation (SA) [69]. Here, the depletion force is evaluated from

$$F_{\mathrm{dep}}(r) = -2\pi \int_0^\infty s^2 \frac{dV_{sc}(s)}{ds} \int_0^\pi \rho_c^{(1)}(\mathbf{s};\mathbf{r}) \cos\theta \sin\theta \, \mathrm{d}\theta \qquad (2.1)$$

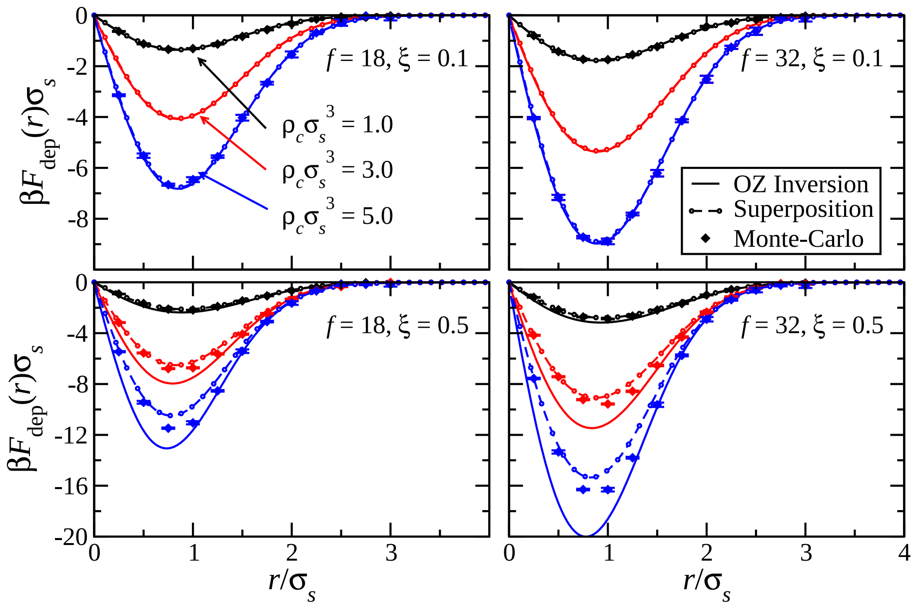

Figure 2.2: Depletion force between two stars immersed in a bath of smaller chains at different functionalities, size ratios and chain densities.

with $\rho_c^{(1)}(\mathbf{s};\mathbf{r})$ the one-body density profile of the chains at position $\mathbf{s}$ induced by the presence of two stars located at $\mathbf{r}_1$ and $\mathbf{r}_2$, where $\mathbf{r} = \mathbf{r}_2 - \mathbf{r}_1$ and $\hat{\mathbf{r}} \cdot \hat{\mathbf{s}} = \cos\theta$. Within the superposition approximation, $\rho_c^{(1)}(\mathbf{s};\mathbf{r})$ is decomposed as the product of the two chain-density profiles surrounding a single star polymer, i.e.,

$$\rho_c^{(1)}(\mathbf{s};\mathbf{r}) = \rho_c \;\; g_{sc}(r; f, \xi, \rho_s \to 0, \rho_c) \;\; g_{sc}(|\mathbf{s} - \mathbf{r}|; f, \xi, \rho_s \to 0, \rho_c) \tag{2.2}$$

where the star-chain radial distribution function, $g_{sc}(r; f, \xi, \rho_s \to 0, \rho_c)$, is readily available from the solution of the OZ equations.

In addition, standard NVT Monte Carlo (MC) simulations were performed on the coarse-grained two component system, see Eqs. (1.1)-(1.3), by placing two stars in a reservoir of chains, and measuring the depletion force $F_{\text{dep}}(r) = -\nabla V_{\text{dep}}(r)$. A comparison of results from these three different approximations is shown in Fig. 2.2. The three methods yield quite good agreement and, as ρ_c and ξ increase, the SA leads to better agreement with the simulation data than the OZ inversion. This implies that the cross-correlation between chains arising from their interaction $V_{cc}(r)$ is weak enough, so that we can still assume that the presence of a second star leads

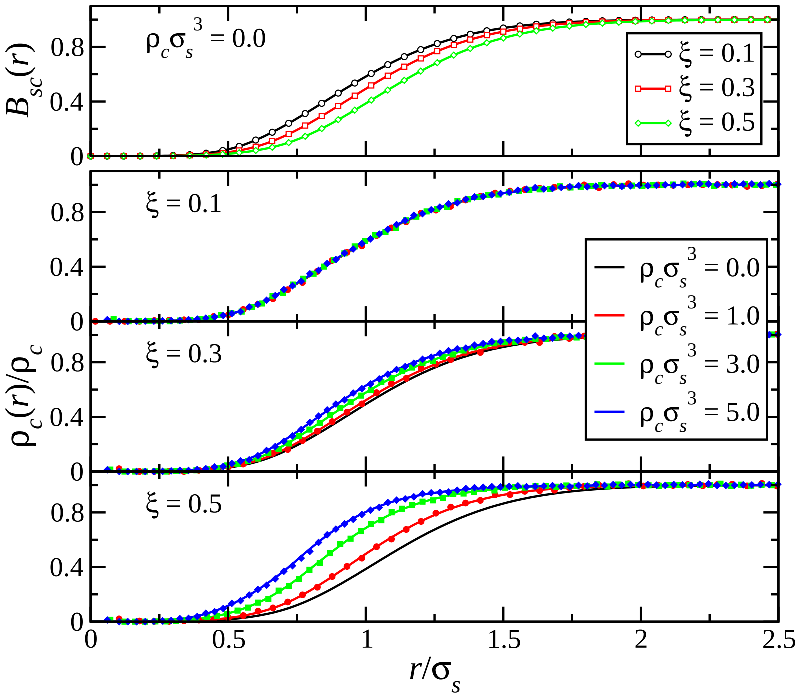

Figure 2.3: Upper panel: the Boltzmann factors $B_{sc}(r) = \exp[-\beta V_{sc}(r)]$ of the star-chain effective interaction potential. Lower panels: the normalized density profile of chains around one isolated star with $f = 32$. Continuous curves were calculated by solving the OZ equation while filled symbols correspond to results from MC simulations. The curves for $\rho_c = 0$ are the Boltzmann factors $B_{sc}(r)$.

to an overall chain density profile that is well approximated by the product of those originated from two isolated stars. Application of more sophisticated techniques based on a second-order expansion of a two-component density functional yield essentially identical results with those reported above.

To understand the physical origin of these unusual features, we look in detail at the chain density profile, $\rho_c(r)$ around a single, fixed star, as shown in Fig. 2.3. The depletion range can be estimated from there as $\Delta_{\text{dep}} \cong 2\Lambda$, where Λ is the length scale at which $\rho_c(r)$ reaches its asymptotic, bulk value. To begin with, we consider $\rho_c(r)$ at the limit of very low chain density, which is proportional to the Boltzmann factor of the star-chain cross interaction, i.e., $\rho_c(r) \cong \rho_c \exp[-\beta V_{sc}(r)]$. At this limit, as ξ increases, the thickness of the depletion layer becomes only slightly larger and clearly *not* in proportionality to ξ. Thus, for the system at hand, Δ_{dep} is just slightly influenced by the size of the depletant polymer chain, even at the limit $\rho_c \to 0$. For the case $\xi = 0.1$ there is no significant change in $\rho_c(r)$, and therefore neither in the size of the depletion zone, as the chain number density ρ_c increases. Concomitantly, only the strength of $V_{\text{dep}}(r)$ grows, as a consequence of the increase in the osmotic pressure $\Pi(\rho_c)$ of the chains. For larger ξ the size of the depletion zone decreases as ρ_c increases, as a consequence of the softness of the star: the chains access a region closer to the center of the star, due to the repulsive interactions with other chains. This penetrability of the star causes the shrinkage of the depletion layer around it and together with the stronger osmotic effects have as consequence a deeper and shorter-ranged depletion potential. Finally, since $V_{\text{dep}}(r)$ itself depends on $V_{sc}(r)$ and $V_{cc}(r)$, but not directly on $V_{ss}(r)$, an increase of the functionality f at fixed size ratio ξ renders $V_{sc}(r)$ more repulsive and therefore the depletion zone around each star widens. This effect results into a larger Δ_{dep} and a deeper attraction, for higher functionality stars, see Fig. 2.2. Contrary to colloid-polymer mixtures, the range of the depletion potential is primarily determined by the nature of the *depleted* particles themselves and *not* by the depletants.

As described in the previous chapter, for low and intermediate functionalities, i.e., $f \lesssim 32$, the star-linear mixtures feature star-cluster formation as a precursor stage for a fluid-fluid demixing transition [70]. This behavior resembles the one predicted via a one-component model of the star suspension, for which one attractive contribution $V_{\text{att}}(r)$ was added to $V_{ss}(r)$, and which had the form of a Fermi distribution [28, 29, 71, 72]:

$$V_{\text{att}}(r) = -\frac{C}{\exp\left[(r-A)/B\right]+1}. \tag{2.3}$$

The above form and the describing parameters was, however, introduced *ad hoc*, arguing on general grounds that depletion would be a mechanism to induce such attractions. Although other model could be used, this Fermi-like model (FLM) has been showed to provide a rather convenient parametrization of generic attractive contributions, which allows for changing the characteristics (range and depth) of the latter; the parameters A and B control the position and width of the well

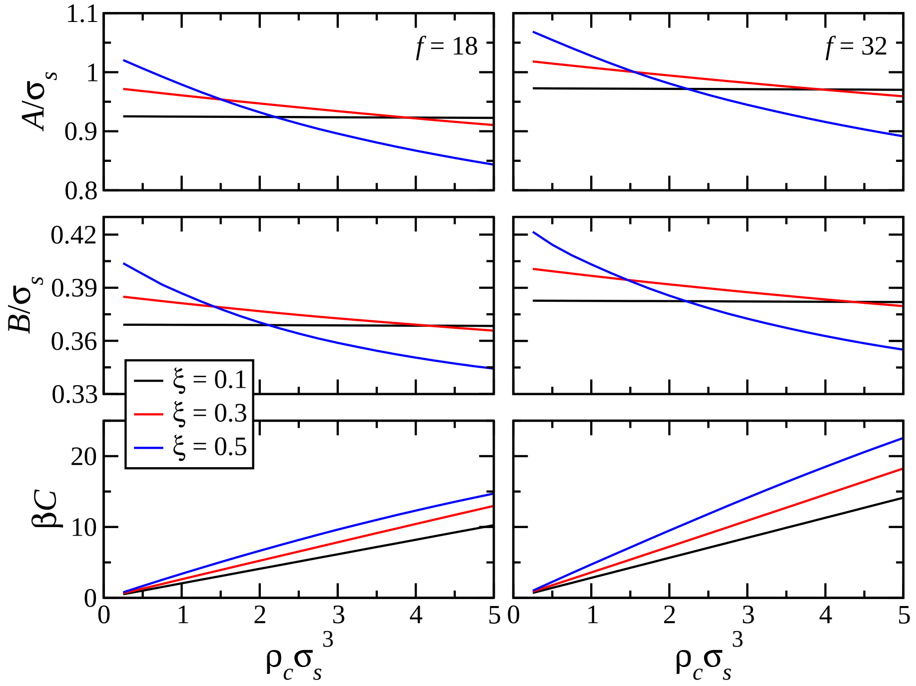

Figure 2.4: Fitting parameters of $V_{\rm dep}(r)$ from SA to the Fermi-like model, Eq. (2.3), as a function of the chain concentration.

potential and C its amplitude [71, 72]. It is thus tempting to see whether star-linear mixtures can be described by this model.

For the system at hand, the FLM indeed describes remarkably well the depletion interactions, as can be seen in the lower panels of Fig. 2.1. Representative results for the dependence of the parameters A, B, and C on the chain density ρ_c are shown in Fig. 2.4 for different size ratios ξ and functionalities f. It is immediately seen that the length scales show a weak dependence on the size ratio ξ: by increasing ξ by as much as a factor five (from 0.1 to 0.5), we obtain very weak changes in the parameters A and B, of order 10% at any given chain density. As the chain density increases, the parameters A and B decrease and the trend becomes *opposite* to what conventional wisdom asserts: long polymers induce *shorter-ranged* depletion potentials than short ones, in strong contrast with the AO case. On the other hand, the strength of $V_{\rm dep}(r)$ grows, as expected, with ρ_c, due to the increase in $\Pi(\rho_c)$.

2.4 Conclusions

In summary, in this chapter we described some remarkable characteristics of the depletion potential in a model soft mixture. We found its range to show a very weak dependence not only on the chain density ρ_c but also on the size ratio ξ. This is counterintuitive, since one would have expected the range to increase as the size of the depletant increases, and it is the result of the softness and penetrability characterizing the components and the ensuing effective interaction potentials of the system at hand. These two characteristics are not peculiar for star polymers but they are present in many other polymer-based colloidal systems. Microgels, micelles, polymer-grafted nanoparticles, dendrimers and, in general, hyperbranched polymers, are highly deformable systems whose topology can be well described through a core and shell structure. The size and softness of the latter one can be easily tuned by changing, for example, the cross-linking or the charge (microgels), the aggregation number (micelles), the grafted density (nanoparticles), and the generation number or the spacer between generations (dendrimers). We expect our results, which are based on the penetrability of the soft shell, to hold as long as the latter is thick enough to accommodate the chains in their full extent. As the range of the depletion potential exceeds that needed for phase separation and cannot be reduced by employing smaller depletants, we anticipate macroscopic, demixing ("liquid-gas") transitions to take place for this family of systems. Therefore, at sufficiently high soft-colloid concentrations, they are expected to undergo the recently reported "arrested spinodal decomposition" [53, 13], which constitutes a novel route to gelation. The mapping of the original full ultrasoft-colloidal mixture on the characteristic parameters of the FLM effective system turns this into a more tractable problem.

Acknowledgments: I thank Dr. Federica Lo Verso for helpful discussions. This work was partially supported by DFG-SFB TR6.

Chapter 3

Soft Colloid/Polymer Mixtures: Comparison with experiments

Binary mixtures of ultrasoft colloids and linear polymer chains were investigated by small angle neutron scattering (SANS) [1] and liquid state theory. We show that experimental data can be described by employing recently-developed effective interactions between the colloid and the polymer chains, in which both components are modeled as point particles in a coarse-grained approach, in which the monomers have been traced out. Quantitative, parameter-free agreement between experiment and theory for the pair correlations, the phase behavior and the concentration dependence of the interaction length is achieved.

3.1 Introduction

Hard spheres have been established in the past as model systems to investigate on a fundamental level the effective interactions and phase behavior of soft matter [16]. A higher level of complexity is introduced when hard sphere mixtures or hard spheres with added linear polymer chains are considered, in the context of depletion

---

[1] The entire set of experimental results showed in this chapter was acquired by Dr. Barbara Lonetti and Dr. Jörg Stellbrink (Institut für Festkörperforschung, Forschungszentrum Jülich).

forces, like the famous Asakura-Oosawa (AO) model for colloid-polymer mixtures [10]. Building on these simple models, great advances have been made in the study of gel and glass formation in colloidal systems [53, 59]. More recently, the interest of colloid scientists has shifted towards the study of soft particles, among which star polymers have emerged as a model for a wide class of soft spheres, including block-copolymer micelles [73, 74] and microgel particles [15]. For a star polymer, softness can be controlled by varying its number of arms (or functionality f), allowing to bridge the gap between linear polymer chains ($f = 2$) and hard spheres ($f \to \infty$) [26]. Therefore, star polymers can be viewed as ultrasoft colloids, whose softness is responsible for the observation of anomalous structural behavior [26] and favors the formation of several crystal structures [27, 73]. In this way, mixtures of soft particles offer a much higher versatility with respect to their hard counterparts, both in terms of structural and rheological properties [49, 50, 75] and of effective interactions [76]. In particular, mixtures of star polymers of different sizes and functionalities have been recently investigated in a joint theoretical and experimental effort, revealing the existence of multiple glassy states [77]. On the other hand, the paradigmatic case of a mixture of star polymers and linear chains (the direct soft counterpart of the AO model) has been investigated separately theoretically [31, 76] and experimentally by (mainly) macroscopic rheology [49, 50, 78]; however, detailed structural information is still missing. Indeed, only recently a microscopic theory [31, 76], capable to appropriately coarse-grain stars and chains, has been developed. Hence, an accurate comparison between theoretical predictions and experimental results for the structural correlations for star/chains mixtures has not been attempted so far.

Recently, we introduced kinetically frozen star-like micelles [74, 79] formed by the amphiphilic block copolymer poly(ethylene-alt-propylene)-poly(ethylene oxide), PEP-PEO, as a tunable model system for ultrasoft colloids [26]. In this chapter we study mixtures of star-like micelles and linear (PEO) chains and provide a systematic and quantitative characterization of structure factors and phase behavior in terms of effective interactions. By combining small angle neutron scattering (SANS) and liquid state theory, we measure and model the effective interactions between star-like micelles and linear chains. SANS measurements in core contrast allow a direct determination of experimental structure factors, $S(Q)$ [80], providing the basis for a comparison with the recently-developed theory, in which both components are modeled as point particles in a coarse-grained approach that traces out the monomeric degrees of freedom. A direct comparison without any adjustable parameters, i.e., using the quantities directly given by experiments, provides a very good agreement between experiment and theory for structure factors, phase behavior and concentration dependence of the interaction length σ. The comparison is done for a broad range of polymer volume fraction from dilute to concentrated conditions, i.e. $0.05 \leq \phi/\phi^* \leq 7$, where ϕ^* is the overlap concentration, and it brings forward the influence of the added chains on the larger star polymers. Our work provides a comprehensive structural characterization of soft binary mixtures in terms of a microscopic, effective potential and is therefore a further step forward in the understanding and modeling of complex soft matter systems in general.

3.2 Methods

Partially deuterated PEP-PEO block polymers, as well as partially deuterated PEO chains, were synthesized by anionic polymerization following established procedures [81]. Molecular details of the systems are given in Table 3.1. All polymers were dispersed in a H_2O/D_2O mixture (5:95, *v*:*v*) to ensure a PEO contrast matching (core contrast). SANS experiments were performed at D11, Institute Laue-Langevin (ILL), Grenoble. Raw data were corrected for detector efficiency and dead time, contributions resulting from empty cell, solvent and incoherent scattering were subtracted and corrected data finally normalized by a water standard to absolute units [cm^{-1}]. The characterization of the single star-like micelle was performed in dilute solution. The form factor $P(Q)$ obtained by SANS experiments was analyzed using a core-shell model, by assuming a star-like density profile in the shell [74]. Light scattering (SLS/DLS) and rheology were used in addition as complementary methods. A compilation of all experimental data gives a functionality $f = 91 \pm 5$ and the characteristic sizes shown in Table 3.1. The results for the gyration radii give in turn a chain-micelle size ratio $\xi = R_g^{(c)}/R_g^{(s)} \cong 0.3$, which was fixed for the subsequent theoretical analysis.

Our theoretical approach is similar to the employed in the previous chapters.

Table 3.1: Characterization of the used polymers.

Molecular characteristics ($[M_w] = \text{g/mol}$)				
Sample	$M_{w,PEP}$	$M_{w,PEO}$	M_w/M_n^{a}	x_D^{b}
hPEP1-dhPEO20	1100	21250	1.03	0.86
dhPEO20	-	21250	1.03	0.86

Characteristic sizes [Å]				
$R_g^{(s)}$	$R_{\text{core}}^{(s)}$	$R_{\text{shell}}^{(s)}$	$R_h^{(s)}$	$R_g^{(c)}$
218 ± 11	34 ± 2	248 ± 12	$317 \pm 16^{\mathrm{c}}$	67 ± 3

[a] Polydispersity by SEC

[b] Molar fraction of deuterated PEO

[c] Hydrodynamic radius obtained from DLS

The effective interactions between the components of the mixture are the same as before. We quote these again for sake of completeness. The star-star interactions reads as [26]:

$$\beta V_{ss}(r) = \frac{5}{18} f^{3/2} \begin{cases} -\ln\left(\frac{r}{\sigma_s}\right) + \frac{1}{1+\frac{\sqrt{f}}{2}} & r \leq \sigma_s \\ \frac{1}{1+\frac{\sqrt{f}}{2}} \left(\frac{\sigma_s}{r}\right) \exp\left[-\frac{\sqrt{f}}{2\sigma_s}(r-\sigma_s)\right] & r > \sigma_s \end{cases} \tag{3.1}$$

where f is the functionality, σ_s is a measure of the star extension and $\beta = (k_B T)^{-1}$ with k_B the Boltzmann constant and T the temperature. Similarly, polymer chains can be considered as two-arm stars interacting via [38, 39]

$$\beta V_{cc}(r) = \frac{5}{18} 2^{3/2} \begin{cases} -\ln\left(\frac{r}{\sigma_c}\right) + \frac{1}{2\tau^2\sigma_c^2} & r \leq \sigma_c \\ \frac{1}{2\tau^2\sigma_c^2} \exp\left[-\tau^2(r^2-\sigma_c^2)\right] & r > \sigma_c \end{cases} \tag{3.2}$$

with $\tau\sigma_c = 1.03$, which guarantees the correct value of the second virial coefficient of a polymer solution. As before, σ_c measures the size of the chain. The star-chain interaction results [31]

$$\beta V_{sc}(r) = \begin{cases} -\Theta(f) \ln\left(\frac{r}{\sigma_{sc}}\right) + K & r \leq \sigma_{sc} \\ v_0 \int \varrho_s(r') \varrho_c(|\mathbf{r}-\mathbf{r}'|) d\mathbf{r}' & r > \sigma_{sc} \end{cases} \tag{3.3}$$

where $\sigma_{sc} = \frac{1}{2}(\sigma_s + \sigma_c)$, $\Theta(f) = \frac{5}{36}\frac{1}{\sqrt{2}-1}[(f+2)^{3/2} - (f^{3/2} + 2^{3/2})]$ and v_0 is an excluded volume parameter. The latter comes from Flory-type arguments for the overlapping monomer density profiles $\varrho_i(r)$ $(i = s, c)$, which can be evaluated on the basis of the Daoud-Cotton blob model (see Appendix A) [31, 32]. We evaluated the density profiles $\varrho_i(r)$ following [31], by employing the fitting parameter $\kappa\sigma_i = 1.90$ (see Eq. (1.4)), which results in a better fit of $V_{sc}(r)$ given by Eq. (3.3) compared to simulation results as the functionality increases ($f \sim 100$). Once the three effective pair potentials V_{ss}, V_{sc} and V_{cc} are known, we can calculate the center-to-center structure factor of stars $S(Q)$ by solving the two-component Ornstein-Zernike (OZ, see Appendix B) equations within the hypernetted-chain (HNC) approximation [41].

3.3 Results and Discussion

For our quantitative comparison between experiments and theory the following quantities are necessary: the reduced number densities of star-like micelles, $\rho_s\sigma_s^3$, and of linear chains, $\rho_c\sigma_s^3$, unambiguously given by experimental concentrations in terms of volume fraction, as well as the functionality f and experimental ξ, both obtained from independent form factor analysis. Following [31, 38], we employ $\sigma_i = 4R_g^{(i)}/3$ $(i = s, c)$. According to the theoretical predictions, upon the addition of linear chains, a strong loss of star-star correlations results, insofar a drastic decrease of the peaks of $S(Q)$ is found in comparison to the structure factor of the pure star system. This change is accompanied by a shift of the peaks to slight higher Q and also by a slight increase of the $S(Q \to 0)$ value. These features can be well explained based on a depletion-like mechanics as described in [49]. The inset in Fig. 3.1 demonstrates the strong weakening of the peak of the star-like micelle scattering intensity upon increasing the chain density at fixed star density $\rho_s\sigma_s^3 = 0.37$. For direct comparison, theoretical $S(Q)$ were multiplied by experimental $P(Q)$ and convoluted with the instrumental resolution function [82].

Fig. 3.1 shows SANS intensities $I(Q)$ for selected concentrations below and around the overlap polymer volume fraction $\phi^* = (f\bar{M}_w/\bar{d}N_A)/(4\pi R_m^3/3) = 3\%$ (amounting to $\rho_s\sigma_s^3 = 0.220$), with $\bar{M}_w$ and $\bar{d}$ the average molar mass and mass density, and $R_m = R_{\text{core}}^{(s)} + R_{\text{shell}}^{(s)}$ (see Table 3.1). The precise value of σ_s was de-

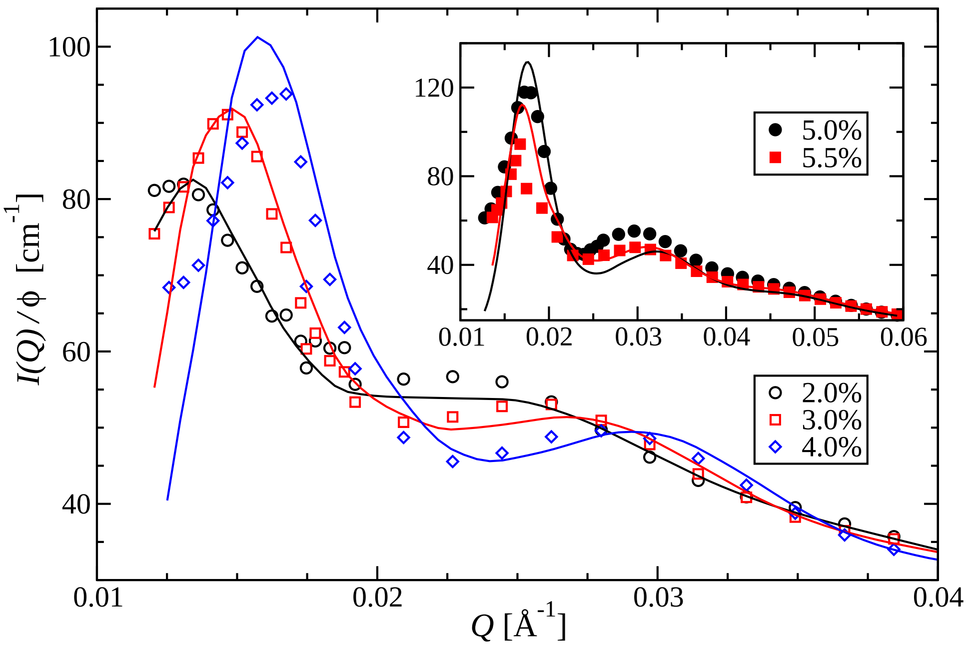

Figure 3.1: Normalized SANS intensity for intermediate polymer volume fractions. Inset: Effect of adding chains on $I(Q)$ at $\rho_s\sigma_s^3$ =0.37 for $\rho_c\sigma_s^3 = 0$ (circles) and $\rho_c\sigma_s^3 = 8.6$ (squares). Symbols and lines correspond respectively to experimental and theoretical results.

termined by optimizing the agreement between theory and experiment for $S(Q)$ at ϕ^*, resulting in $\sigma_s(\phi^*) = 305\,\text{Å}$, in good agreement with previous, independent estimates [26, 49] and within the experimental error bars of about 6% for $R_g^{(s)}$. The agreement between experiment and theory is very convincing. Position, height and width of first and second order peak of liquid-like experimental structure factors are indeed nicely described by the theory. Only at very low Q-vectors some deviations occur, most probably due to not-perfect contrast matching conditions. In addition, from concentration ϕ=5% ($\rho_s\sigma_s^3 = 0.367$) on, the experimental peak height of the first structure factor peak is overestimated by theory due to the expected shrinkage of the micellar corona following $\sigma_s \sim (\phi/\phi^*)^{-1/8}$ [32].

This effect is shown in more detail in Fig. 3.2 for higher concentrations well above ϕ^*. We point out that this shrinkage does not affect the size ratio ξ since the linear polymer also shrinks, following the same scaling relation. Consequently, the shrinkage is taken into account by re-adjusting the corresponding concentrations in terms of $\rho_s\sigma_s^3$ and $\rho_c\sigma_s^3$. The resulting theoretical $I(Q)$ are shown as continuous lines in Fig. 3.2 and clearly improve the agreement with experimental data. Similar effects are achieved for concentrations even as high as 20% ($\approx 7\phi^*$). Nevertheless, the description of experimental data slightly worsens with concentration, most probably due to three body forces, which become relevant for $\phi/\phi^* \gtrsim 5$ [83].

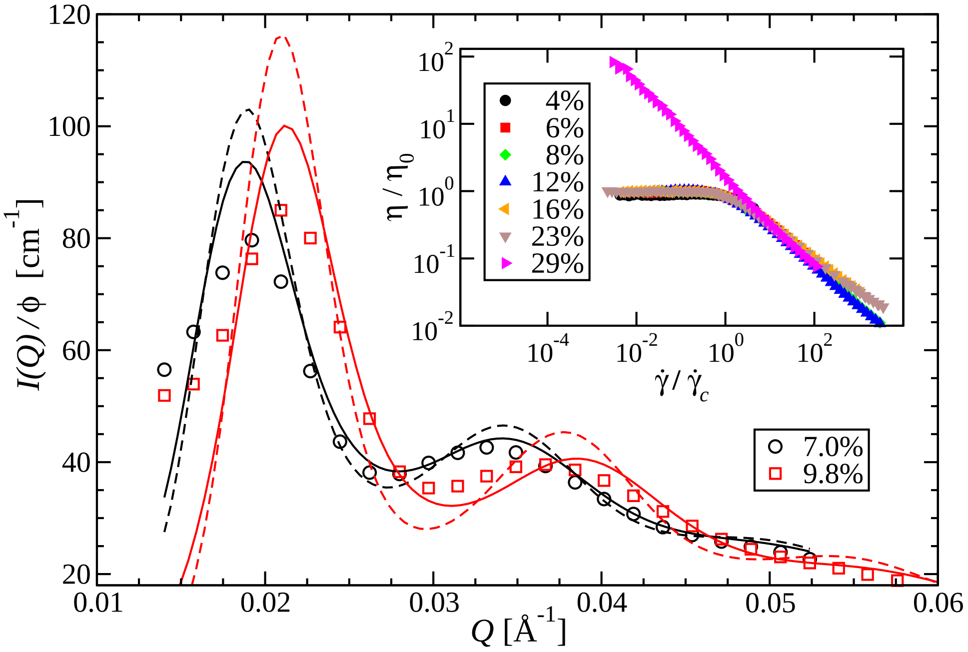

Figure 3.2: Normalized SANS intensity for volume fractions well above ϕ^*. Symbols correspond to experiments, dotted lines to theory with constant σ, and continuous lines to theory with decreasing $\sigma \sim (\phi/\phi^*)^{-1/8}$. Inset: Reduced viscosity as function of the reduced shear rate for selected volume fractions, with η_0 the zero shear viscosity and $\dot{\gamma}_c$ obtained from a Carreau-Fit [84].

To strengthen our quantitative comparison between experiment and theory, we also consider the phase behavior of the system. Indeed, while $S(Q)$ is only slightly affected by varying the size ratio ξ, the phase behavior can be sensitively altered by a small change in the same. Therefore, the agreement in phase behavior will provide an additional consistency check to narrow down the values of σ_s, σ_c and ξ and to establish the correctness of the effective interactions that we have adopted.

We investigated the rheological properties of the samples by means of both steady and oscillatory shear measurements. As can be seen in the inset of Fig. 3.2, most of viscosity curves display the Newtonian-plateau typical for a liquid, as well as the usual shear-thinning behavior at high shear rates. For larger concentration, namely $\phi = 29\%$ ($\rho_s \sigma_s^3 = 0.887$), we find a transition to a solid (glassy) state, clearly indicated by the absence of the Newtonian plateau. The formation of an arrested state was also verified for $\phi = 33\%$ ($\rho_s \sigma_s^3 = 0.966$) by tube inversion.

The theoretical phase diagram is shown in Fig. 3.3 for two different values of size ratios $\xi = 0.27$ and $\xi = 0.30$ in the (ρ_s, ρ_c) plane. To account for the possible existence of a demixing region, we make use of the fact that, although the HNC approximation is an accurate method to describe the one-phase region, it fails to converge in the neighborhood of a (gas-liquid) spinodal line [41]. In this way, the convergence line (CL) in Fig. 3.3, which denotes the region where HNC provides a convergent solution to the OZ equations, can be considered an estimate of the phase separation region. Hence, above the CL, we expect the homogeneous mixture to become unstable with respect to demixing. Although it is possible to determine the coexistence curve from the HNC results [55], this is beyond the scope of this chapter, and therefore we keep the CL as an indicator of the location of phase separation. To assess the existence of a freezing line, we use the Hansen-Verlet (HV) criterion. Thus, on the right of the HV line, the main peak of $S(Q)$ is larger than 2.85 which corresponds to crystallization of star-like micelles at $\rho_c = 0$ [74]. Finally, an (ideal) glass transition line (GL) is shown indicating vitrification at high concentrations [85]. This line was calculated by means of the (one-component) mode-coupling theory (MCT) [86], which uses as inputs only $S(Q)$ and number density of the stars (see Appendix C). Representative results from the solution of MCT equations are displayed in Fig. 3.3. As can be seen, the addition of polymer chains leads to glass melting, at fixed ρ_s, as previously demonstrated [50, 75].

The investigated experimental points are also reported on this phase diagram. Given the constant ratio between star-like micelles and linear chains, our experimental path through the phase diagram is a straight line with slope $x_n/(1 - x_n)$, with x_n the number density fraction of the linear chains. For all experimental samples under investigation, no macroscopic phase separation was observed, and hence

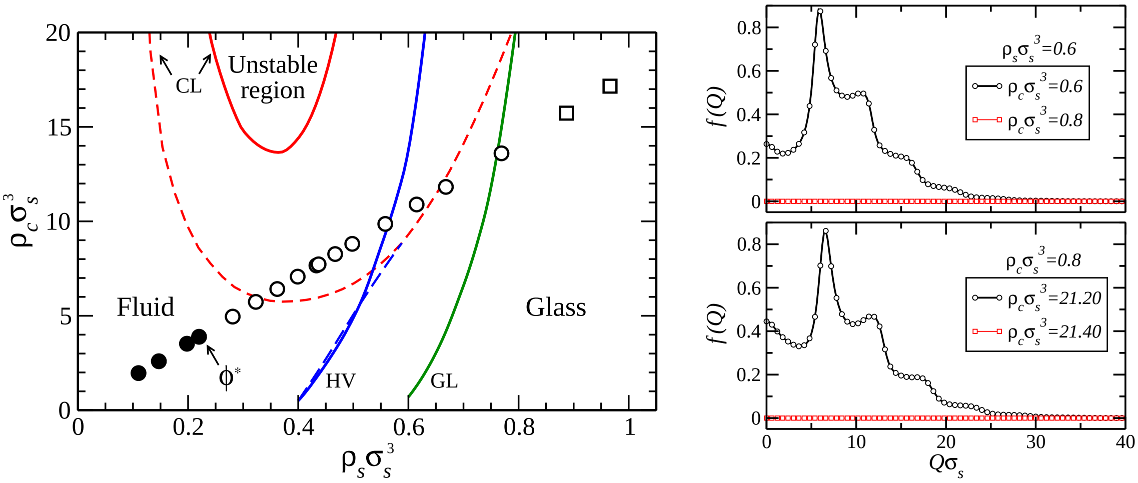

Figure 3.3: Left: Phase diagram: Symbols denote our experimental path (open symbols assuming shrinkage, open squares correspond to glassy samples) whereas lines are given by theory (CL, HV and GL represent respectively the convergence, freezing and glass lines). Full lines correspond to size ratio $\xi = 0.3$ (the actual experimental one), while the dashed lines provide a comparison for $\xi = 0.27$. Right: Non-ergodicity factors from MCT indicating the locus of the glass line in (ρ_s, ρ_c)-plane

they all lie in the one-phase region, in agreement with the theoretical CL results for $\xi = 0.30$. Therefore a crossing with the theoretical CL, which would happen for a smaller size ratio $\xi = 0.27$, must be excluded. This result confirms that the actual experimental size ratio is close to $\xi = 0.30$, as previously established by the $S(Q)$ analysis. At higher concentrations, our experimental path meets the HV line suggesting that an intervening liquid-solid transition might take place. However a large number of studies on star polymer systems has shown that it is quite difficult to nucleate a crystal, while instead solutions at high concentrations undergo a disordered arrested state [50, 87]. This was also the case for our star-like micelles in the absence of added chains at the same functionality as in the present study [74]. In the presence of chains, we also find that arrest is retarded to higher concentrations, in agreement with previous studies [50, 87]. Indeed, for the most concentrated samples, the dynamical arrest to an amorphous solid (glass) agrees with the phase diagram of Fig. 3.3.

3.4 Concluding remarks

In summary, we have described structural and phase behavior of binary mixtures of ultrasoft colloids and linear polymers. By combining small angle neutron scattering (SANS) and liquid state theory we offer robust experimental evidence to the accuracy of the coarse-graining procedure for developing effective interactions between the star-like micelles and the homopolymer chains, in a wide range of concentrated mixtures. Without any adjustable parameter we find quantitative agreement between experiments and theory for the influence of the added chains on the inter-micelle structure and on their phase behavior. Our work provides a comprehensive characterization of soft binary mixtures in terms of a microscopic, effective potential and is therefore a successful benchmark in the study of complex soft matter systems in general, opening the way for exploring experimentally the features of anomalous depletion predicted theoretically [76], and for studying even more versatile systems of soft particles, such as, e.g., mixtures of micelles with block copolymers [66, 73].

Acknowledgments: I am grateful to Dr. Barbara Lonetti and Dr. Jörg Stellbrink (Forschungszentrum Jülich) who carried out the experimental work described in this chapter. As well as, I thank Dr. Christian Mayer and Dr. Emanuela Zacarrelli for helpful discussions. This work was supported by DFG-SFB TR6 and by ITN-234810-COMPLOIDS (Marie Curie Training Network, EU).

Chapter 4

Interfacial and wetting behavior of phase-separating GEM mixtures

We apply density functional theory to study the interfacial properties of a phase-separating binary fluid of ultrasoft particles, whose interaction potentials belong to the family of the so-called generalized exponential models (GEM). By using the formalism of the density functional theory within the mean-field approximation, we investigate the equilibrium density profiles for each component at the free interface as well as at a repulsive, flat wall. We show that the studied system can lead to first-order wetting transition which is characterized by a layering-like behavior due to the clustering properties of GEM particles.

4.1 Introduction

In the last few years, a great deal of effort has been devoted to develop coarse-grained models of complex macromolecules of several architectures and a large number of internal degrees of freedom (e.g. linear and hyperbranched polymers, micelles, microgels, etc). In some cases, such models allow to represent the macromolecular entities as effective particles interacting via an effective, isotropic potential $V_{\text{eff}}(r)$ [4]. On the opposite extreme of the hard-sphere colloidal interaction, many of the aforementioned effective potentials $V_{\text{eff}}(r)$ belong to the family of the so-called ultrasoft interactions [5]. Examples of potentials belonging to this class are the gaussian-like interactions between polymer coils, dendrimers and charged microgels in the center-of-mass representation (gaussian core model) [35, 36, 88] as well as the effective interaction between star polymers and polymer chains in the midpoint representation [26, 38].

The first example is particular because, when the center of mass of the aggregates can overlap, $V_{\text{eff}}(r)$ turns out to be not only ultrasoft but also free of divergences (bounded). A particular mean-field "ideal-gas" behavior has been found for a large class of such bounded potentials, meaning that the mean-field approximation (MFA) becomes asymptotically exact for large densities and does give accurate results for finite densities both in uniform and non-uniform phases [89, 90, 91, 92]. The MFA pertains, in this context, to set $c(r) = -\beta V_{\text{eff}}(r)$, where $c(r)$ is the Ornstein-Zernike direct correlation function. Furthermore, bounded potentials may lead to novel phenomena, provided $V_{\text{eff}}(r)$ belongs to the so-called $Q^{\pm}$-class, i.e., the Fourier transform $\hat{V}_{\text{eff}}(q)$ displays an oscillatory decay around zero, whereas interactions with positive Fourier transform are referred as Q^{+} potentials. In the $Q^{\pm}$-case, the fluid features a Kirkwood instability (also called λ-line) and therefore undergoes a microphase ordering to crystals with multiply-occupied lattice sites (cluster crystals) at high enough density [92, 93, 94, 95].

Extensive simulation studies of both amphiphilic dendrimers and ring polymers of different knotedness demonstrate that such system might be experimental realizations for macromolecules featuring an effective interaction of the $Q^{\pm}$ class [96, 97, 98, 99]. From the theoretical point of view, a particular example of $Q^{\pm}$ potentials is given by the generalized exponential model of index m (GEM-m), for which the interaction is described by $u(r) = \epsilon \exp\left[-\left(r/\sigma\right)^{m}\right]$ where r is the interparticle distance, σ is a measure of the particle's size, ϵ is the interaction strength, and $m > 2$. Note that a particularly important member of this family is the penetrable sphere model [100], which features a finite overlap energy penalty ϵ and which corresponds to the limit $m \to \infty$. Recently, the phase behavior of systems composed by GEM particles has been extensively investigated by making use of the above mentioned mean-field character.

Concerning pure GEM systems, the phase diagram shows a first-order transition from a fluid of clusters to a cluster bcc-crystal above the triple temperature and a subsequent structural phase transition from a cluster bcc to a cluster fcc crystal as density increases for arbitrarily high temperatures [92, 94]. A remarkable property of the cluster fcc crystals is that, upon increasing the density, the lattice constant approaches a constant value and therefore the population of each lattice site scales proportionally with density. This behavior is completely different from the "normal" crystallization in colloidal systems, in which the relevant role is playing by packing effects. On the other hand, when binary mixtures containing a non-clustering component ($m = 2$) and a clustering component ($m = 4$) were considered, evidence was found suggesting a quite sensitive interplay between crystallization induced by the clustering specie and macrophase separation [101, 102], depending on both energy and length parameters of the cross-interaction between the two species.

A systematic analysis concerning both the interfacial and the wetting properties of GEM-mixtures across their coexisting line is still lacking. In this chapter we aim to study the interfacial properties and the wetting behavior of a demixing, binary fluid of GEM particles by means of the density functional theory. We follow the same line of ideas used to study these phenomena in other ultrasoft systems, namely mixtures of gaussian core particles and star-polymers mixtures [55, 103, 104]. The rest of the chapter is organized as follows: In Sec. 4.2 we present the employed model and a brief survey on density functional theory. The calculation of the free interface properties and the ensuing wetting properties follows in Sec. 4.3. Finally, in Sec. 4.4, we summarize and draw our conclusions.

4.2 Model and Method

We consider a binary mixture of particles interacting through GEM potentials given by

$$u_{ij}(r) = \epsilon_{ij} \exp\left[-\left(\frac{r}{\sigma_{ij}}\right)^{m_{ij}}\right], \qquad i,j = A, B, \tag{4.1}$$

where the following interaction parameters were adopted: $\epsilon_{ij} = \epsilon = 1.0$, $\sigma_{ii} = \sigma$, $\sigma_{AB} = 1.07\sigma$, and $m_{AA} = 2$, $m_{AB} = 3$, $m_{BB} = 4$. The energy parameters are given in units of the thermal energy k_BT with k_B the Boltzmann constant and T the absolute temperature. In this way, the mixture contains a non-clustering component (GEM-2, in the following referred as A-species) and a cluster-forming component (GEM-4, in the following referred as B-species). The cross-interaction was chosen to be a GEM-3 potential, which also displays cluster formation in a pure system. As mentioned above, our main interest is to study the surface and wetting properties of this system. In this way, the inhomogeneous phases will be considered within the framework of the density functional theory (DFT) for a flat geometry.

In DFT the grand potential of a binary system becomes a functional of the one-particle density profiles $\rho_i(\mathbf{r})$ $(i = 1, 2)$ and can be expressed as [105]:

$$\Omega[\{\rho_i\}] = F[\{\rho_i\}] - \sum_{i=1}^{2} \int d\mathbf{r}\rho_i(\mathbf{r}) \left[\mu_i - V_i(\mathbf{r})\right], \tag{4.2}$$

where $F[\{\rho_i\}]$ is the intrinsic Helmholtz free energy, $V_i(\mathbf{r})$ is the external potential acting on species i and μ_i the corresponding chemical potential. Once $F[\{\rho_i\}]$ is known, the equilibrium density profiles of the system can be determined by minimizing $\Omega[\{\rho_i\}]$ with respect to $\rho_i(\mathbf{r})$. The free energy is normally expressed as a combination of the ideal part $F_{id}[\{\rho_i\}]$ and the excess contribution $F_{exc}[\{\rho_i\}]$, the latter arising from the interaction between particles. The first contribution to the free energy is exactly known and can be expressed as:

$$F_{id}[\{\rho_i\}] = \beta^{-1} \sum_{i=1}^{2} \int d\mathbf{r}\rho_i(\mathbf{r}) \left\{\ln\left[\rho_i(\mathbf{r})\Lambda_i^3\right] - 1\right\}, \tag{4.3}$$

where Λ_i is the thermal de Broglie wavelength for species i and $\beta = (k_BT)^{-1}$. On the other hand, the excess part of the free energy has to be constructed in an approximate way. As mentioned above, for the type of potentials considered here, the mean-field approximation provides an accurate functional for $F_{exc}[\{\rho_i\}]$, namely

$$F_{exc}^{(\mathrm{MFA})}[\{\rho_i\}] = \frac{1}{2} \sum_{i,j=1}^{2} \int\int d\mathbf{r}d\mathbf{r}'\rho_i(\mathbf{r})\rho_j(\mathbf{r}')u_{ij}(|\mathbf{r} - \mathbf{r}'|) \tag{4.4}$$

where $u_{ij}(r)$ is the interaction potential between species i and j. Within the MFA the minimization of (4.2) with respect to $\rho_i(\mathbf{r})$ leads to

$$\mu_i - V_i(\mathbf{r}) = \sum_{j=1}^{2} \int d\mathbf{r}' u_{ij}(|\mathbf{r} - \mathbf{r}'|)\rho_j(\mathbf{r}') + \beta^{-1} \ln\left[\rho_i(\mathbf{r})\Lambda_i^3\right], \qquad i, j = 1, 2, \tag{4.5}$$

an equation system that can be solved for the equilibrium density profiles according to the appropriate boundary conditions.

4.3 Results

4.3.1 Bulk properties

The system defined above satisfy the condition of the MFA for fluid-fluid phase-separation at constant pressure, i.e., $\hat{u}_{AB}^2(0) > \hat{u}_{AA}^2(0) + \hat{u}_{BB}^2(0)$, where $\hat{u}_{ij}(0)$ is the Fourier transform of the potential at $q = 0$. In the case of GEM particles the latter is given by

$$\hat{u}_{ij}(0) = \int u_{ij}(r)d\mathbf{r} = \frac{4\pi}{3}\epsilon_{ij}\sigma_{ij}^3\ \Gamma\left(\frac{3+m_{ij}}{m_{ij}}\right), \tag{4.6}$$

with $\Gamma(x)$ the Gamma function. By using the double-tangent construction on the Gibbs free energy per particle [89, 103], the corresponding fluid-fluid coexistence line was determined. The latter is shown in Fig. 4.1 in the plane (x, ρ) defined by the relative composition $x = \rho_B/\rho$ and the total number density $\rho = \rho_A + \rho_B$. In the system at hand, fluid-fluid demixing occurs for total densities in the range $4.0 \lesssim \rho\sigma^3 \lesssim 5.0$. At larger total density, the liquid-liquid demixing is pre-empted by liquid-solid transitions which are explained in detail in [101].

Additional information concerning the asymptotic form of the pair correlation functions $h_{ij}(r)$ for the fluid phase, which is relevant to the understanding of some aspects of the interfacial phase behavior, can be obtained by the analysis of the complex poles in the corresponding Fourier transforms $\hat{h}_{ij}(q)$. Pure imaginary ($q = i\alpha_0$) and complex ($q = \mathrm{i}\alpha_0 + \alpha_1$) poles give rise, respectively, to pure exponential and damped oscillatory decays (note that the special case of a pole at zero wavenumber delineates the demixing spinodal). In particular, the poles $\mathrm{i}\alpha_0^* + \alpha_1^*$ with the smallest imaginary part α_0^* will set up the longest range part of *all* pair correlations functions, namely $rh_{ij}(r)|_{r\to\infty} \cong A_{ij}^* \exp(-\alpha_0^* r)\cos\left(\alpha_1^* r + \theta_{ij}^*\right)$, with the amplitude A_{ij}^* and the phase θ_{ij}^*, as demonstrated in [106, 107]. The locus of state points where the crossover from pure exponential to a damped oscillatory decay takes place, defines the so-called Fisher-Widom line (FWL).

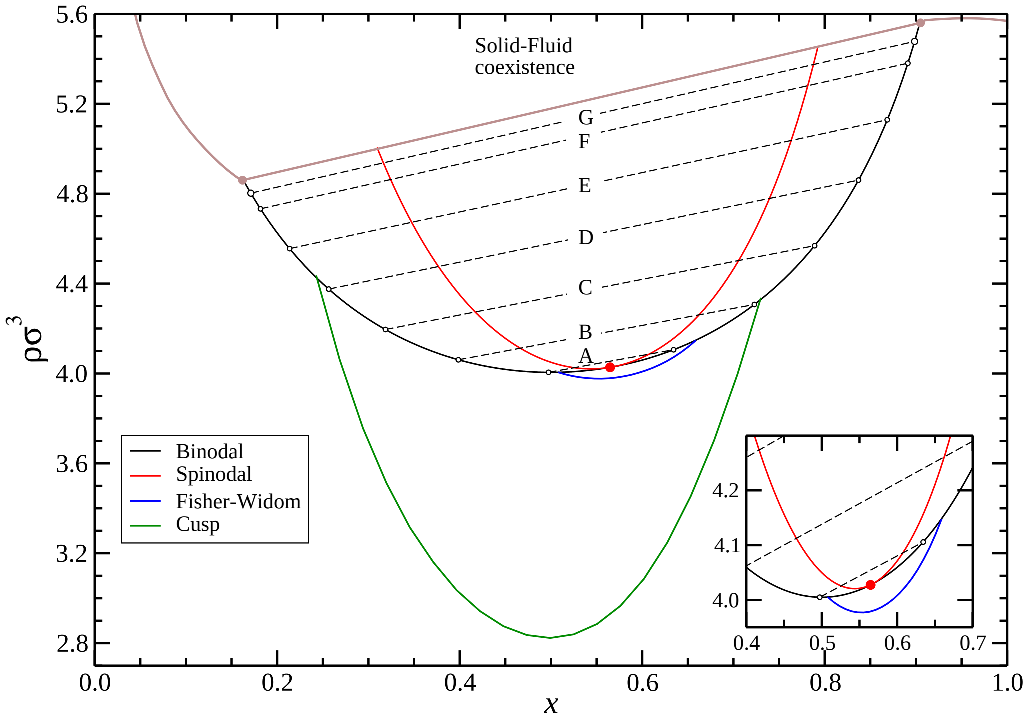

Figure 4.1: Fluid-fluid coexistence line (binodal) for the system at hand. Tie lines joining coexisting points are represented by dashed lines. They are labeled from A to G and correspond, respectively, to the reduced pressures $P\sigma^3/k_BT =$ 43.5, 46, 50, 55, 60, 65, 67. For larger densities, the phase separation is preempted by fluid-solid transitions (see [101]). The inset displays the region close to the critical point, in which the locus of the Fisher-Widom line lies. States located outside the small region between the binodal and the Fisher-Widom lines will feature correlation functions with damped oscillatory decay. Two regimes of oscillatory decay are found, which are separate by the cusp line.

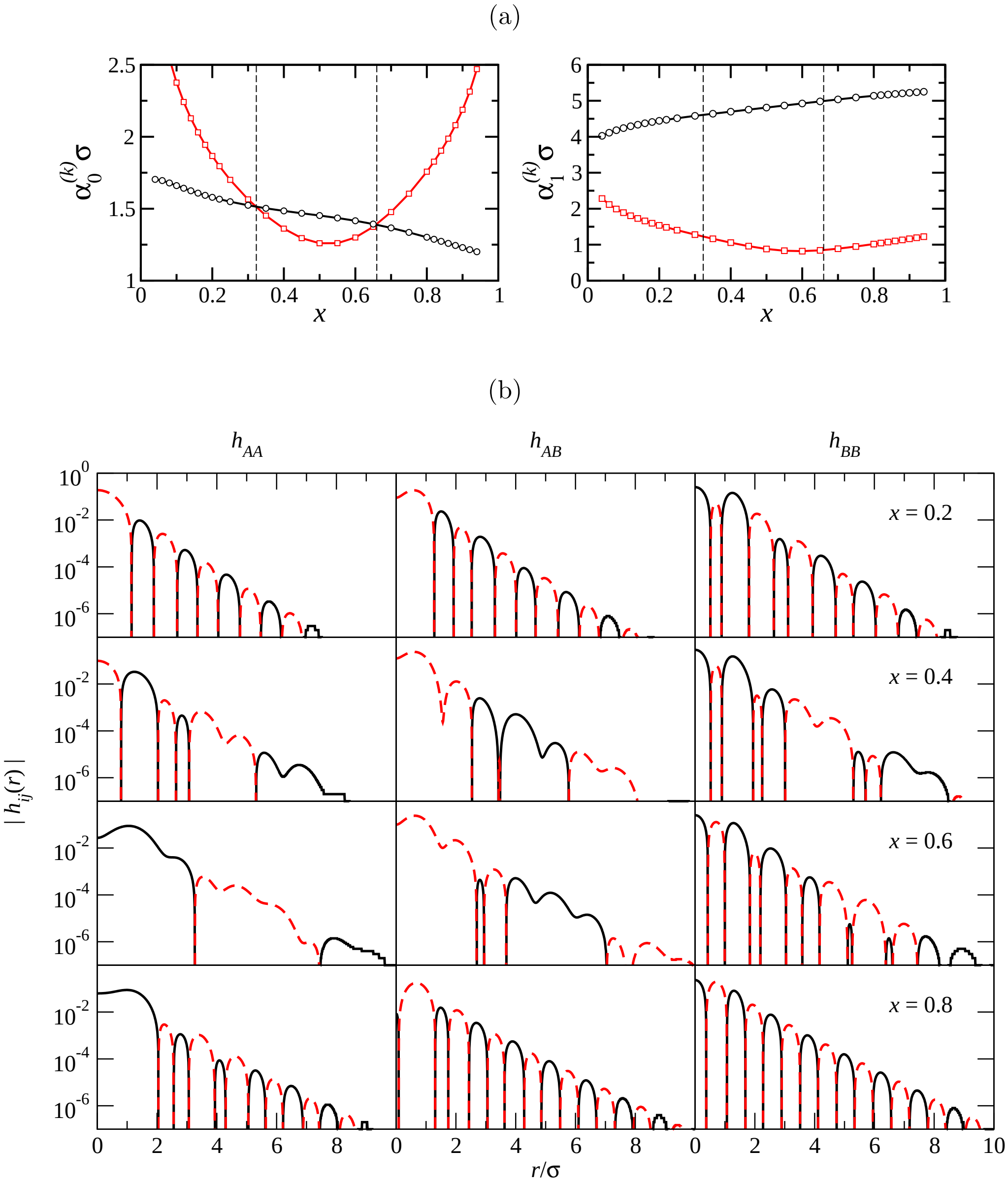

Figure 4.2: (a) The imaginary and real parts of the complex roots of $D^{(\mathrm{MFA})}(\alpha_1+\mathrm{i}\alpha_0)$ with the two smallest imaginary parts $\alpha_0^{(k)}$ $(k=1,2)$, for fixed total density $\rho\sigma^3=3.5$ and different relative compositions. The vertical dashed lines indicate the occurrence of the cusp line. (b) Absolute values of the pair correlation functions for $\rho\sigma^3=3.5$ and various relative compositions x, as indicated in the legends. The dashed segments represent the negative parts of $h_{ij}(r)$.

According to the Ornstein-Zernike equation in Fourier space, the correlation functions of a homogeneous fluid take the generic form $\hat{h}_{ij}(q) = N_{ij}(q)/D(q)$, where the mean-field denominator results

$$D^{(\mathrm{MFA})}(q) = 1 + \beta\rho\hat{U}_s(q) + (\beta\rho)^2\, x(1-x)\hat{U}_d(q), \tag{4.7}$$

with $\hat{U}_s(q) = (1-x)\hat{u}_{AA}(q) + x\hat{u}_{BB}(q)$ and $\hat{U}_d(q) = \hat{u}_{AA}(q)\hat{u}_{BB}(q) - \hat{u}^2_{AB}(q)$ [101]. The FWL for the system at hand was determined by finding the roots of Eq. (4.7) and the result is shown in Fig. 4.1. The qualitative form of the FWL is reminiscent of that for symmetric gaussian mixtures, see Figs. 4 and 5 in [103]. However, and in contrast to that case, in the present model the FWL turns out to lie quite close to the consolute point ($x_c \cong 0.5648, \rho_c\sigma^3 \cong 4.0274$) and a cusp line does show up. The latter marks a crossover between regions of the plane (x, ρ) with two different types of oscillatory decays of the correlations functions (see Fig. 4.1). As Fig. 4.2(a) shows, for states between the binodal line and the cusp line, the damped oscillatory decay of $h_{ij}(r)$ is determined by two similar decay lengths $\lambda_0^{(k)} = 1/\alpha_0^{(k)} \sim 0.7\sigma$ and two different wavelengths $\lambda_1^{(1)} = 2\pi/\alpha_1^{(1)} \sim \sigma$ and $\lambda_1^{(2)} = 2\pi/\alpha_1^{(2)} \sim 6\sigma - 7\sigma$.

In asymmetric gaussian mixtures a cusp line is also found, but there this is a consequence of the size difference between the particles. In the present model, the two oscillatory components appear as a consequence of the spatial growth of intercalated domains of similar particles, as demonstrated by the cross correlation function $h_{AB}(r)$ in Fig. 4.2: around any one A particle, it is more likely to find other A particles up to a distance $\sim 2\sigma$ beyond which a shell of clustered B particles is located ($\sim 4\sigma$). Besides, due to the $Q^{\pm}$ character of B particles, the corresponding domains (clusters) present some degree of polydispersity, as can be noted from functions $h_{BB}(r)$. The merging and coarsening of the aforementioned domains will lastly lead to the macrophase separation (demixing transition) as the total density increases.

4.3.2 Interfacial properties

In this section the density profiles across the free planar interface between the two coexisting demixed phases are considered. By imposing $V_i(\mathbf{r}) = 0$, $\rho_i(z \to -\infty) =$

$\rho_i^{(A)}$ and $\rho_i(z \to +\infty) = \rho_i^{(B)}$, with $\rho_i^{(\alpha)}$ the coexisting density of component i in the α-rich phase, Eq. (4.5) can be expressed as

$$\rho_i(z) = \rho_i^{(B)} \exp\left(\sum_{j=1}^{2} \int_{-\infty}^{\infty} dz' \Delta\rho_j(z') \phi_{ij}(|z - z'|) \right), \tag{4.8}$$

where $\Delta\rho_i(z) = \rho_i(z) - \rho_i^{(B)}$ and

$$\phi_{ij}(|z|) = \beta \int_{|z|}^{\infty} \xi u_{ij}(\xi) d\xi = \frac{\epsilon_{ij}\sigma_{ij}^2}{m_{ij}}\, \Gamma\left(\frac{2}{m_{ij}}, |z|^{m_{ij}} \right), \tag{4.9}$$

with $\Gamma(a, x)$ being the incomplete Gamma function [108]. The coupled equation system (4.8) was numerically solved by using a standard Picard's iterative procedure. The resulting solutions for the equilibrium density profiles at different coexistence points, denoted as A-G in Fig. 4.1, are displayed in Fig. 4.3.

As expected, the density profiles are smooth close to the consolute point and, as the density increases, non-monotonic profiles can be observed for both species on both sides of the interface. By defining the relative densities $\rho_A^* = (\rho_A^{(B)} - \rho_A(z))/\delta_A$ and $\rho_B^* = (\rho_B(z) - \rho_B^{(A)})/\delta_B$, with $\delta_i = \rho_i^{(B)} - \rho_i^{(A)}$, the latter behavior can be made more transparent, as shown in the insets of Fig. 4.3. As can be seen, with the exception of the coexisting states A, the profiles for all others tested points feature oscillations whose relative amplitude is much larger on the A-rich phase. Besides, closer inspection indicates that the oscillatory behavior can be observed at larger distances into the B-rich side.

Since it is expected that $\Delta\rho_i(z \to \pm\infty)$ exhibits the same type of behavior of $h_{ij}(r \to \infty)$ for the fluid bulk at the same pressure [106], the previously mentioned characteristics of the density profiles are easily rationalized by looking at the Fisher-Widom line. In this way, since the state A is the only located inside the FWL (see inset in Fig. 4.1), the corresponding density profiles are the only ones featuring monotonic decay on both sides of the interface for both species. On the other hand, as x increases the decay parameter α_0 decreases (see Fig. 4.2(a)), so that the decay length is larger for the density profiles on the B-rich side. This behavior is similar to that found in the binary gaussian core model and in star polymers mixtures [55, 103]. Finally, the fact that the relative amplitude of the oscillations on the

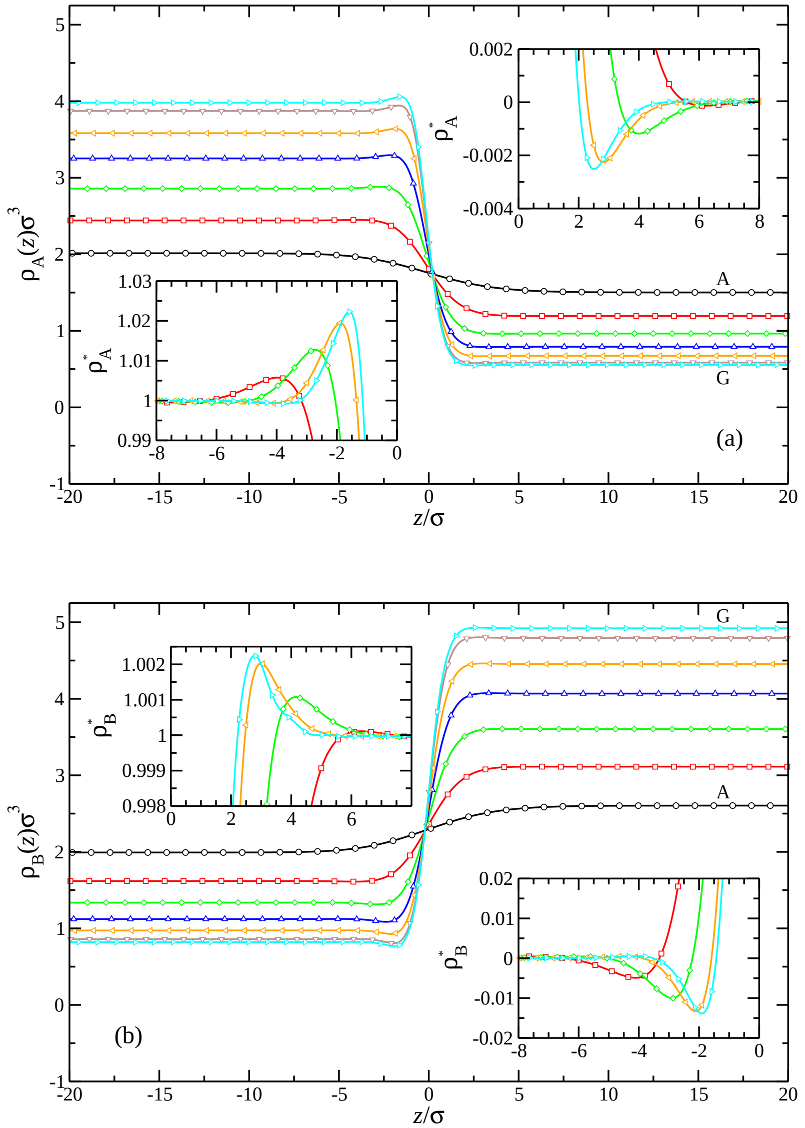

Figure 4.3: Fluid-fluid interface density profiles of gaussian (left) and GEM-4 particles (right) calculated at points A-G on the phase diagram (see Fig. 4.1). The insets show the behavior of the relative densities ρ_A^* and ρ_B^* on either side of the interface.

A-rich side are larger that on the B-rich side can be attribute to packing effects, which are much stronger for the gaussian particles than for GEM-4 particles, due to the $Q^{\pm}$ character of the latter ones. Note also that the majority of B-particles in the B-rich phase creates a "planar wall" for the A-rich phase, which is harder than the opposite one.

Once the density profiles are known, the surface tension γ between the coexisting phases can be calculated by replacing them in Eq. (4.2). According to the mechanical definition of the surface tension [105, 109], γ is related to the difference between the normal and the tangential components of the pressure tensor and can expressed as

$$\gamma = \int_{-\infty}^{\infty} \left[\omega(z) + P\right] dz, \tag{4.10}$$

where P and $\omega(z)$ are respectively the pressure at coexistence and the grand-potential density, i.e., $\Omega[\{\rho_i\}] = \int \omega(z) d\mathbf{r}$ [see Eq. (4.2)].

Figure 4.4(a) displays the resulting surface tension as a function of the order parameter $\delta_B = \rho_B^{(B)} - \rho_B^{(A)}$. This figure also shows that, as predicted by mean-field considerations, a cubic dependence of γ on the density difference between the two phases results [109]. By using the maximum value of $\beta\gamma\sigma^2$ in Fig. 4.4(a) and taking the typical values $\sigma \sim 20$ nm and $T \sim 300$ K, we estimate $\gamma_{\max} \sim 10$ μN/m, which is of the same order of magnitude as the one obtained for colloid-polymer mixtures, but several order of magnitude below the one corresponding to molecular liquids [110].

To shed some light into the origin of the surface tension in the demixing fluid, it is helpful to consider the total density number $\rho(z) = \rho_A(z) + \rho_B(z)$ and the (symmetrized) surface segregation $\Delta(z)$ [111, 112]. The latter measures the variation of the local concentration through the interface and is given by

$$\Delta(z) = \frac{1}{a_A a_B} \left(a_B \left[\rho_A(z) - \rho_A^{(B)} \right] - a_A \left[\rho_B(z) - \rho_B^{(B)} \right] \right), \tag{4.11}$$

where $a_i = \delta_i/(\delta_A + \delta_B)$. In Fig. 4.4 the integrand of Eq. (4.10), i.e., the surface excess tangential pressure as well as the functions $\rho(z)$ and $\Delta(z)$ are plotted. According to the square-gradient approximation to the interfacial free energy, it turns out that both the excess tangential pressure and the surface tension can be expressed as

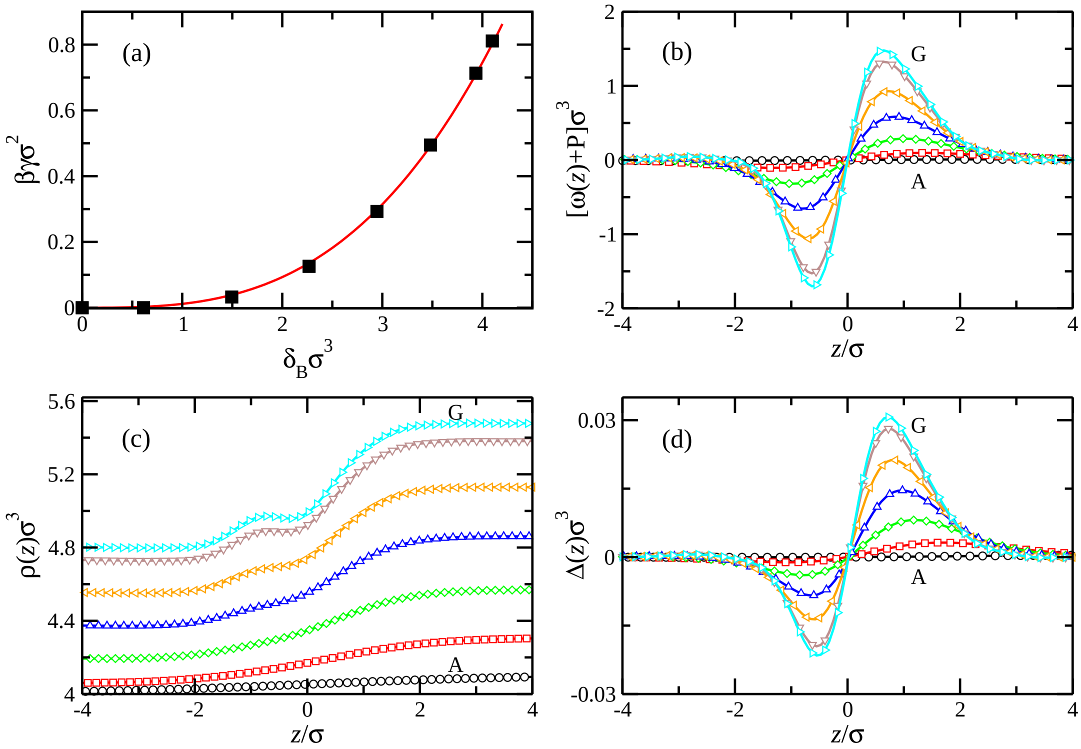

Figure 4.4: (a) Surface tension as a function of the order parameter $\delta_B = \rho_B^{(B)} - \rho_B^{(A)}$. The continuous line corresponds to a fit of the obtained data (filled symbols) to a cubic dependence, i.e., $\gamma \propto \delta_B^3$. (b) Difference between the normal and the tangential components of the pressure tensor across the interface for points A-G (see Fig. 4.1). (c)-(d) Total number density and symmetrized surface segregation for the same states.

a combination of three terms γ_{ab} $(a, b = \rho(z), \Delta(z))$, each depending on integrals over the gradients of a and b [111, 112]. Since $\omega(z) + P$ and $\Delta(z)$ share the same qualitative behavior, as can bee seen in Fig. 4.4, we speculate that the dominant contribution to γ arises from the segregation term. On the other hand, the surface segregation has been also used as an appropriate measure for the interfacial thickness τ, by considering the latter to be the range in z where $|\Delta(z)|$ deviates more than a few percent ($\sim 5\%$) from its maximum [113]. By using this criterion, we found $\tau \gtrsim 5\sigma$ for the considered values of total density.

Thermal fluctuations give rise to the existence of capillary waves along the interface, which have as a consequence the broadening of the free surface between the coexisting phases. Since DFT is a mean-field treatment, it does not account for such effects and therefore one has to resort to another approach in order to incorporate them into the analysis. One way is to consider a gaussian renormalization (smearing) of the "bare" profiles, i.e., those obtained from DFT, over the thermal roughness $\xi_\perp$. In the capillary wave spectrum, each Fourier component $h_\mathbf{q}$ of the interface displacement (perpendicular to the z-direction) contributes according to $\langle |h_\mathbf{q}|^2 \rangle = (2k_BT/\gamma)(L/q)^2$, with γ the surface tension and L the system size [109, 114]. This result leads to $\xi_\perp^2 = \langle |h_\mathbf{r}|^2 \rangle = (k_BT/2\pi\gamma)\ln(L/\lambda_0)$ with $\lambda_0 = 1/\alpha_0$ the bulk correlation length. The main effect of the broadening is to renormalize the amplitude of the oscillatory profile tails by a factor $\exp(-\alpha_R^2 \xi_\perp^2/2)$, where $\alpha_R^2 = \alpha_1^2 - \alpha_0^2 \sim 1/\sigma^2$ is characteristic of the corresponding bulk fluid. In this way, a parameter measuring the strength of the capillary-waves can be defined as $\omega = (4\pi\beta\gamma\sigma^2)^{-1}$. Using typical numerical values, we obtain $\omega \sim 0.1$ for the largest calculated γ, suggesting that the fluctuations should not bring about significant broadening of the interface for the system at hand.

4.3.3 Wetting

In order to study the wetting properties of the considered system close to a rigid wall, we postulate a repulsive external potential, which the wall exerts on particles of species i, having the form:

$$V_i(z) = \begin{cases} \infty & z \leq 0 \\ \Phi_i \frac{\exp(-z/\lambda_i)}{z/\lambda_i} & z > 0 \end{cases} \tag{4.12}$$

where $\Phi_i \approx k_B T$ and λ_i is a parameter of order σ_i. The Yukawa-like form of $V_i(z)$ is motivated by the effective wall-polymer potential obtained from Monte Carlo simulations via the inversion of the center-of-mass distribution function of self-avoiding-walk (SAW) polymers at a hard wall. Since a SAW polymer can be effectively described by a gaussian particle, it was demonstrated that the density profile of gaussian particles at a Yukawa-like wall mimics the SAW polymer center of mass profile at a hard-wall [35, 89]. Qualitatively similar effective wall-particle interactions have been described by recent simulations of both athermal and amphiphilic dendrimers at planar walls [96, 98].

The inhomogeneous density profiles imposed by the presence of the wall can be calculated from Eq. (4.5). By replacing the chemical potential in favor of the bulk densities, we obtain the coupled equations:

$$\rho_i(z) = \rho_i^{(b)} \exp\left[-\beta V_i(z) + \sum_{j=1}^{2} \int_0^\infty dz' \Delta\rho_j(z')\phi_{ij}(|z'-z|)\right], \tag{4.13}$$

where $\Delta\rho_i(z) = \rho_i(z) - \rho_i^{(b)}$ and $\rho_i^{(b)} = \rho_i(\infty)$ is the density of species i ($i = A, B$) in the bulk. We choose to fix the total density ρ and approach the bulk phase boundary (i.e., the binodal line) from the A-rich (B-rich) side by increasing (decreasing) x toward its value at coexistence x_{coex}. For the approaching paths, we solve Eq. (4.13) and determine the corresponding (Gibbs) adsorption on the wall, which is defined by

$$\Gamma_i = \int_0^\infty dz \left[\rho_i(z) - \rho_i^{(b)}\right]. \tag{4.14}$$

Wetting by gaussian particles

By choosing a B-rich mixture as the bulk fluid, we studied the wetting of the wall by the A-rich phase for several sets of the parameters determining the wall potential given by Eq. (4.12). Since both considered species have the same size, it is natural to

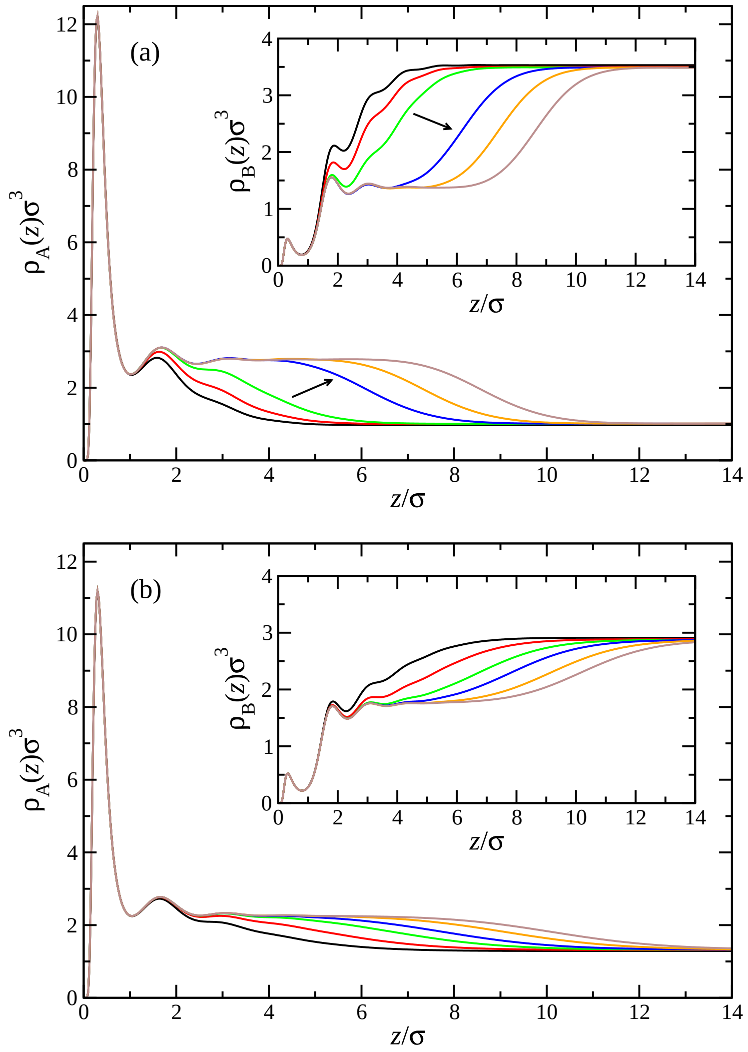

Figure 4.5: Density profiles of species A adsorbed at the wall along the constant densities (a) $\rho\sigma^3 = 4.5$ and (b) $\rho\sigma^3 = 4.2$, as the coexistence state is approached from the B-rich side. The parameters defining the wall potential, Eq. (4.12), are $\Phi_A = \Phi_B = \epsilon$, $\lambda_A = \sigma$ and $\lambda_B = \sigma_{AB}$. In each figure, the profiles correspond, from left to right, to $|x - x_{\text{coex}}| = 10^{-2}, 3.5\times10^{-3}, 1.2\times10^{-3}, 5.0\times10^{-4}, 1.0\times10^{-4}, 5.5\times10^{-6}$. The insets show the corresponding density profiles of species B, in which the depletionof B particles from the wall is clearer as the A-rich film grows. For the case $\rho\sigma^3 = 4.5$, the arrow marks the discontinuous jump in the thickness of the film which is found when the pre-wetting line is crossed.

take $\lambda_i = \sigma$. With this choice, incomplete wetting is found for all tested $\Phi_A/\Phi_B \lesssim 1$ and $\Phi_B \approx \epsilon$ as $x \to x_{\mathrm{coex}}^{+}$. A different situation is obtained if the wall potential is chosen to be somewhat longer-ranged for the species B, i.e., to slightly favor wall contact with the A particles. By setting up the parameters to $\Phi_i = \epsilon$, $\lambda_A = \sigma$ and $\lambda_B = \sigma_{AB}$, a similar scenario to the one obtained for asymmetric gaussian mixtures is found [55, 104].

In this case, a pre-wetting transition is present, as first revealed by inspection of the density profiles. At high enough total density ($\rho\sigma^3 \gtrsim 4.8$) the profile of the species A saturates as the binodal is approached and no thick film is formed, indicating that such density is above the wetting point. On the other hand, as $x \to x_{\mathrm{coex}}^{+}$ at lower ρ ($4.3 \lesssim \rho\sigma^3 \lesssim 4.7$) the thickness of the adsorbed film starts to grow slowly, then it features a discontinuous jump and finally it grows up continuously, as shown in Fig. 4.5(a) for $\rho\sigma^3 = 4.5$. This behavior is consistent with the pre-wetting scenario, in which the jump in the density profile occurs when the pre-wetting line is crossed and subsequently the thickness of the film diverges as the coexistence line is reached [115]. Eventually, at a further lower total density ($\rho\sigma^3 \lesssim 4.3$), the adsorbed film grows up continuously as $x \to x_{\mathrm{coex}}^{+}$ suggesting that such a path is located below the pre-wetting critical point, as Fig. 4.5(b) shows for $\rho\sigma^3 = 4.2$. We postpone for the last section a discussion of the nature of this wetting transition, i.e., whether the film that grows is truly infinite or we rather have a first-order thin-to-thick-film transition with the latter having a large but finite thickness.

The above-described features can be also observed in Fig. 4.6(a), where the corresponding adsorption curves for the A specie are plotted as a function of the quantity $\ln|x - x_{\mathrm{coex}}|$. As can be seen, for the largest total density the absorption saturates in the limit $x \to x_{\mathrm{coex}}^{+}$. On the other hand, for lower densities (below the wetting point) both discontinuous and continuous rises in adsorption can be distinguished. As before, the discontinuity is related to the pre-wetting line and once this line is crossed the adsorption grows in a similar way for all curves as x goes toward the coexistence value. By using the discontinuous jump both in density profiles and adsorption curves, we have estimated semi-quantitatively the locus of the pre-wetting line by taking into account that it joints the binodal tangentially[1].

---

[1] A more rigorous procedure involves the evaluation of the two branches of solutions which

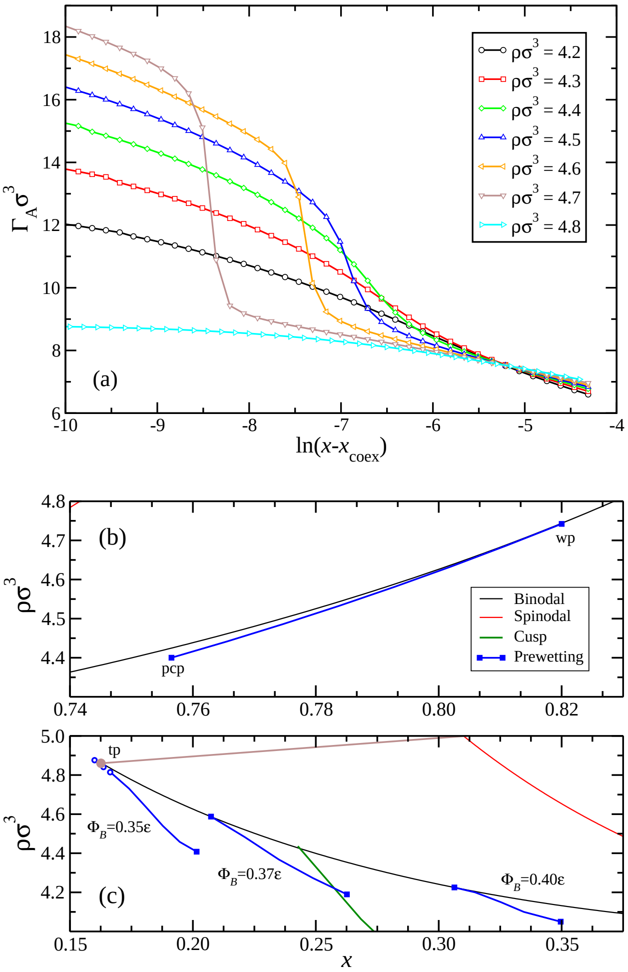

Figure 4.6: (a) Adsorption of species A at the wall along several paths of constant density, as the binodal line is approached from the B-rich side. It saturates for $\rho\sigma^3 = 4.8$ and grows discontinuously for $\rho\sigma^3 = 4.7$, indicating that the wetting point is located between these two densities and that a pre-wetting transition takes place for the latter one. The parameters defining the wall potential, Eq. (4.12), are $\Phi_A = \Phi_B = \epsilon$, $\lambda_A = \sigma$ and $\lambda_B = \sigma_{AB}$. (b) Magnification of the phase diagram (Fig. 4.1) for the high-x region in which the pre-wetting line for the A specie lies. This line meets the binodal in the wetting point (wp) and ends in the pre-wetting critical point (pcp). (c) Magnification of the phase diagram for the low-x region in which the pre-wetting lines for the B specie corresponding to different Φ_B values are shown. The wetting point for $\Phi_B/\epsilon = 0.35$ lies beyond the triple point (tp).

The resulting curve lies very close to the binodal and extends from the wetting point ($x_{wp} \approx 0.8198, \rho_{wp}\sigma^3 \approx 4.74$) until the pre-wetting critical point ($x_{pcp} \approx 0.7665, \rho_{pcp}\sigma^3 \approx 4.4$), as displayed in Fig. 4.6(b).

Wetting by GEM-4 particles

Having evaluated the wetting properties by the gaussian particles, in this section we turn our attention to the properties of the other component of the system. Again the total density is fixed but now the binodal is approached from the A-rich side. The parameters defining the wall-particle interaction are the same as before, except for Φ_B which is tuned in order to make the wall less repulsive to B particles.

When $\Phi_B/\epsilon \gtrsim 0.5$ is considered, incomplete wetting is found for all tested total densities, indicating that the wetting point would be located very close to the consolute point. On the other hand, by taking $0.35 \lesssim \Phi_B/\epsilon \lesssim 0.45$ evidence for pre-wetting transition is obtained, as revealed by the jump in the adsorption curves and the subsequent continuous growth as $x \to x_{\text{coex}}^{-}$, as shown in Fig. 4.7. As Φ_B is further decreased, the effective attraction between GEM-4 particles and the wall becomes strong enough to guarantee complete wetting at all densities over the left branch of the binodal; for all tested densities the adsorption diverges continuously as the coexistence line is approached, as shown in Fig. 4.7 for $\Phi_B/\epsilon = 0.3$.

In order to have a better description of the transition represented by the discontinuity in the adsorption curve, we consider the corresponding density profiles. As a representative sample, in Fig. 4.8(a) the density profiles of both species for $\Phi_B/\epsilon = 0.35$ are plotted at $\rho\sigma^3 = 4.5$. Concomitantly with the discontinuous jump in Γ_B, the density profile $\rho_B(z)$ displays a substantial increase in both the first and the second peaks and afterwards the thickness of the film increases continuously. This feature contrasts with the case of wetting by the A-rich phase, where the first peak of $\rho_A(z)$ remains unaltered once the pre-wetting line is crossed, i.e., once the discontinuity in adsorption is found, as can be seen in Fig. 4.5. Of course, note has to be taken that, in the present case, the wall is comparatively more attractive for

---

minimize the grand potential, i.e., one branch for a thin adsorbed film and other for a thick adsorbed film. The points where the two branch intersect determine the pre-wetting line [55, 104].

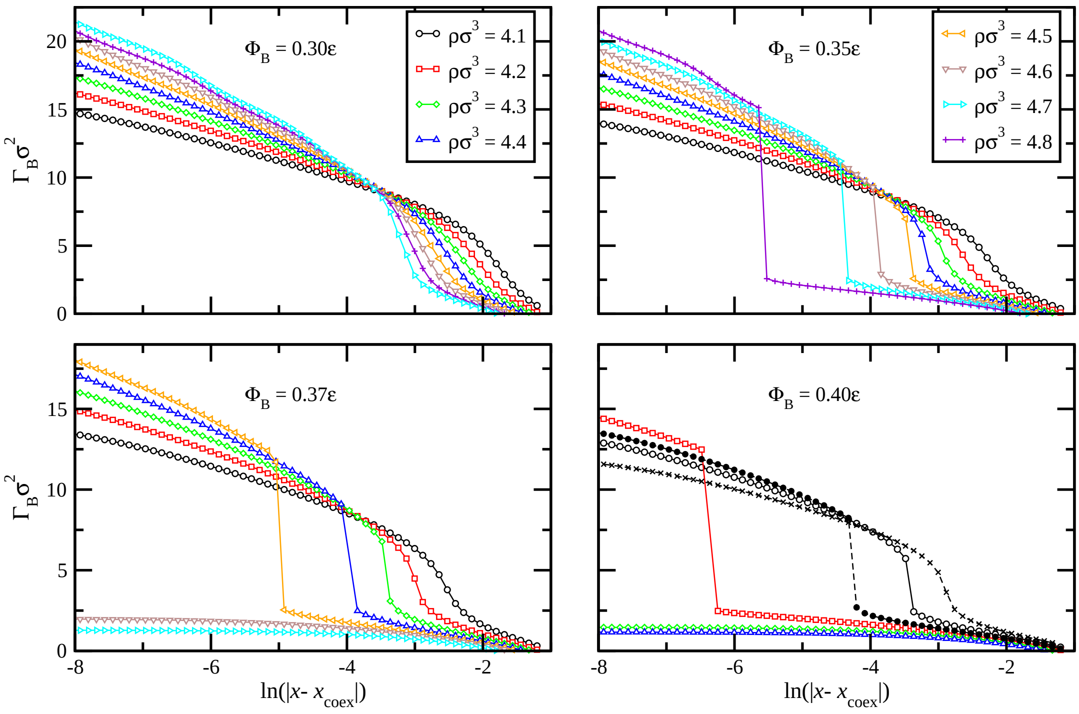

Figure 4.7: Adsorption of species B at the wall along several paths of constant density, as the binodal line is approached from the A-rich side. The parameters defining the wall potential, Eq. (4.12), are $\Phi_A = \epsilon$, $\lambda_A = \sigma$ and $\lambda_B = \sigma_{AB}$. By decreasing Φ_B, particles B will be preferentially adsorbed by the wall, moving the wetting point towards the triple point. In the last panel, the full-circle line corresponds to $\rho\sigma^3 = 4.15$ and the line with crosses to $\rho\sigma^3 = 4.05$.

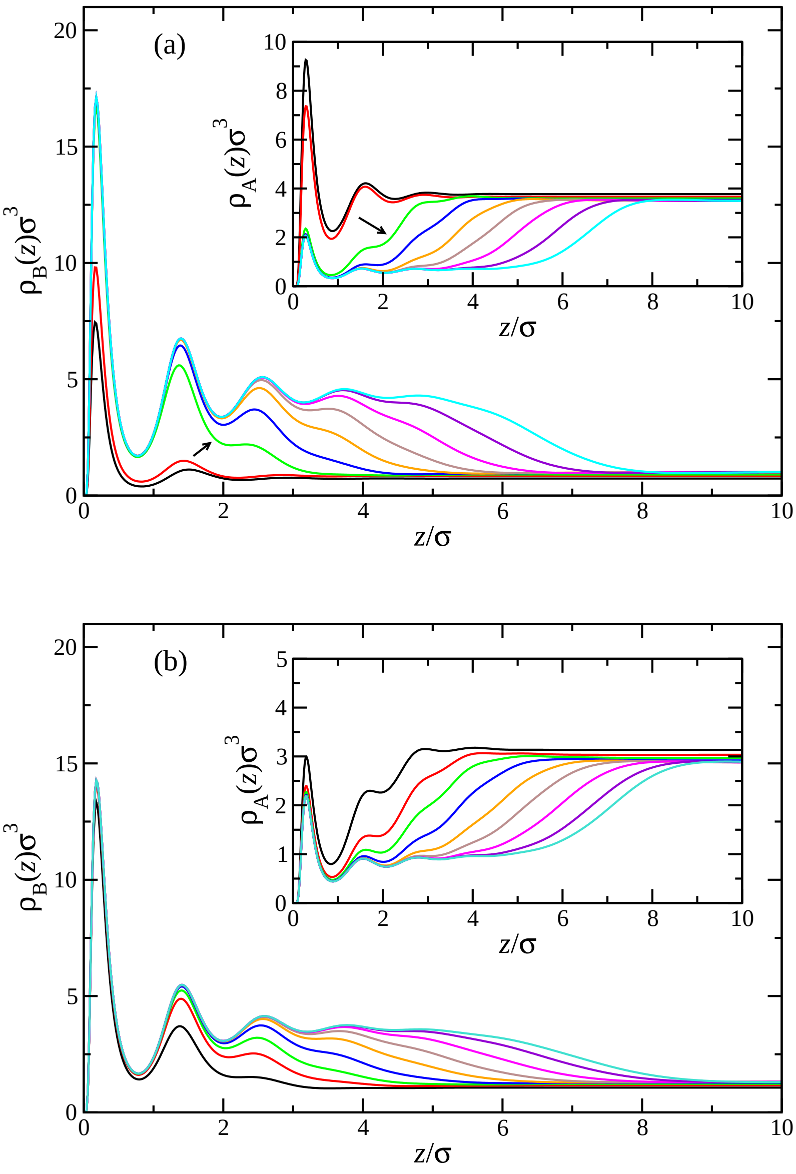

Figure 4.8: Density profiles of specie B adsorbed at the wall along the constant densities $\rho\sigma^3 = 4.5$ (a) and $\rho\sigma^3 = 4.2$ (b) as the coexistence state is approached from the A-rich side. The parameters defining the wall potential, Eq. (4.12), are $\Phi_A = \epsilon$, $\Phi_B = 0.35\epsilon$, $\lambda_A = \sigma$ and $\lambda_B = \sigma_{AB}$. In each figure, the profiles correspond, from left to right, to $|x - x_{\text{coex}}| = 6.3 \times 10^{-2}, 4.0 \times 10^{-2}, 2.4 \times 10^{-2}, 1.2 \times 10^{-2}, 4.5 \times 10^{-3}, 1.7 \times 10^{-3}, 5.2 \times 10^{-4}, 1.0 \times 10^{-4}, 1.4 \times 10^{-5}$. The insets show the corresponding density profiles of specie A.

B particles than it was for A particles in the previous case.

On the other hand, at $\rho\sigma^3 = 4.2$ the first peak of $\rho_B(z)$ remains unmodified and the second one reaches its maximum value continuously, as well as the thickness of the adsorbed film, as Fig. 4.8(b) shows. This is an indication that the path for constant density $\rho\sigma^3 = 4.2$ is located below the pre-wetting critical point. The estimated pre-wetting lines for different values of Φ_B are plotted in Fig. 4.6(c). As expected, the localization of the pre-wetting line is quite sensitive to changes in the parameters defining the wall potential. As can be seen, as Φ_B decreases the wetting point moves towards the triple point and the pre-wetting line becomes larger and does extend over a wider range of relative composition x.

The sudden change in the peak structure of $\rho_B(z)$ is reminiscent of the one found for a single layering transition [115, 116], whereby a new peak, corresponding to an adsorbed layer, does develop at the transition point and the adsorption jumps by an amount equivalent to the extra layer of particles. A similar transition has been reported in mixtures of colloid-polymer mixtures at a hard wall, where the wall effectively attracts the colloids stronger that the polymers via the depletion mechanism, giving rise to a very strong "capillary condensation"-like shift of the coexistence chemical potential of the colloids [117, 118]. However, in strong contrast with that case, in the ultrasoft mixture the adsorption does not remain finite as x goes towards x_{coex} but it does diverges exponentially leading at last to complete wetting, as Fig. 4.7 shows. Besides, no additional layering-like transitions were detected when Eq. (4.13) was solved along the coexistence curve.

From Fig. 4.8, it is clear that once the discontinuity is left behind, the adsorbed film is not only thick but it also presents a strong oscillatory structure. The latter feature becomes more pronounced as the tested state moves closer to the triple point, as reflected in the enhancement of the slight bumps in the adsorption curve, see e.g., the adsorption curves for $\Phi_B = 0.35\epsilon$ at $\rho\sigma^3 = 4.7$ and 4.8. Although no jump is apparent indicating other transitions close to the triple point, it must be noted that the present approach gives no information on the lateral structure of the adsorbed layers, since it assumes density profiles $\rho_i(z)$ that are modulated in the direction perpendicular to the wall *only*. Therefore, the possibility of crystallized layer can no be ruled out, as discussed below.

4.4 Concluding remarks

By means of a mean-field density functional theory, the interfacial and wetting properties of a binary mixture of non-clustering particles (A species) and clustering particles (B species) have been investigated. In the case of the free interface, it was found that the density profiles of both species display oscillatory decay on both sides of the interface. This characteristic was associated to the small region of the phase space enclosing by the binodal and the Fisher-Widom line (FWL). Moreover, an estimation of the surface tension and the effect of the capillary-waves on the broadening of the interface was discussed.

Concerning the wetting properties of the mixture at a repulsive Yukawa-like wall, we found pre-wetting transition when the binodal is approached from either the A-rich or from the B-rich side. When short-ranged particle-particle and wall-particle interaction potentials are considered, it is expected that $\Gamma \propto \ln|x - x_{\text{coex}}|$ as the coexistence line is approached below the wetting point, i.e., the adsorption diverges logarithmically, similar to the thickness of the film [55]. This is indeed the trend observed in the considered cases, as Figs. 4.6(a) and 4.7 show. However, from a formal point of view the formation of a macroscopically wetting film can only occur when the corresponding bulk correlation functions decay monotonically, i.e., for states on the monotonic side of the FWL. Otherwise, an oscillatory effective interface potential (excess grand potential per unit area) will develop, which can stabilize thick but finite films ($\sim 10\sigma - 20\sigma$) [114]. Since the total densities of all the state points considered in Fig. 4.6(a) and 4.7 are located outside of the corresponding FWL (see Fig. 4.1), then only pseudo-wetting can be expected to happen in the system at hand. Accordingly, the prewetting lines should be considered as first-order transition lines between a thin and a thick film, where the thickness of the latter does not diverge as the binodal is approached. However, the infinitely thick layer is still a metastable state [114].

It is interesting to note that when simple fluids with an infinitely repulsive core and an attractive tail are adsorbed at attractive walls, complete wetting could take place by means of a sequence of many layering transitions. However, when comparable wall-particle interactions but softer particle-particle interactions are employed, less defined peaks are found in the density profiles $\rho(z)$ and therefore fewer layering transitions can be identified [116]. Following this idea and having in mind that in our particular case, all the particle-particle interactions are "ultrasoft", if more layering-like transitions are present in our system as the binodal is approached from the A-rich side, then they become much more difficult to identify.

One question is still to be answer concerning the high value of the first peak of $\rho_B(z)$ seen in Fig. 4.8(a) and the possibility to have a two-dimensional crystallization of the first layer. Although this effect can not be captured with the approach employed here, we still can discuss some indications in this direction by taking advantage of one analogous system. When a one-component fluid of clustering particles (GEM-8) is considered in planar confinement due to Lennard-Jones walls, the freezing in terms of the symmetry breaking in the plane parallel to the walls is mainly due to a single-wall effect [119]. By taking the limit of large confinement distance, for which the (local) density of the fluid in the middle of the confining region is very close to that of a semi-infinite fluid reservoir on a single LJ wall, it was found that an increasing number of layers starts to grow continuously, each having a smaller cluster population (number of particles per cluster) than the previous one, as the bulk freezing chemical potential is approached from below. Sequentially, the xy-symmetry is broken in each layer and finally the walls are completely wetted by the crystal. The growth of the wetting film is lastly interrupted by capillary condensation. A similar scenario can happen in our system if we assume that the B-rich film is asymmetrically confined by the solid wall and the "flat wall" provided by the A-rich phase [118].

Finally, although there is clear evidence that ultrasoft potentials of the $Q^{\pm}$ class accurately model the interactions between real macromolecules in dilute systems, the validity of these potentials in dense systems has yet to be verified. The results presented in this paper add to a growing body of work which suggests that the search for dense systems where ultrasoft potentials remain valid is a worthwhile pursuit.

Acknowledgments: I would like to thank Dr. Sarah Overduin for helpful discussions. This work was supported by ITN-234810-COMPLOIDS (Marie Curie Training Network, EU).

Chapter 5

Dynamics in binary cluster crystals

Recent studies on the phase behavior of binary mixtures of GEM particles have provided evidence for the formation of novel kinds of alloys, depending on the cross interactions between the two species. In this chapter we study the dynamic behavior of such binary mixtures by means of extensive molecular dynamics simulations. Particularly, we analyze the effect of the addition of non-clustering particles on the dynamic scenario of one-component cluster crystals.

5.1 Introduction

Coarse-graining procedures provide a general way to represent mesoscopic aggregates of several architectures (e.g., linear and hyperbranched polymers, micelles, microgels, etc.) as particles interacting via an effective, isotropic potential $V_{\text{eff}}(r)$. When the center of mass of such aggregates can coincide without violating excluded volume interactions, $V_{\text{eff}}(r)$ turns out to be ultrasoft and bounded [35, 36, 88]. These characteristics may lead to cluster formation providing $V_{\text{eff}}(r)$ belongs to the so-called $Q^{\pm}$-class, i.e. its Fourier transform (FT) $\hat{V}_{\text{eff}}(q)$ displays an oscillatory decay around zero (potentials with positive FT are referred as Q^{+} potentials) [91, 93]. Recent numerical investigations of amphiphilic dendrimers and of ring polymers with different degree of knotedness demonstrate that such macromolecules are candidates for experimental realizations of the former clustering scenario, since their effective interactions are indeed of the $Q^{\pm}$-class [97, 98, 99].

A particular theoretical realization of $Q^{\pm}$ potentials is given by the generalized exponential model (GEM-m), for which the interaction is described by the potential $v(r) = \epsilon \exp\left[-(r/\sigma)^m\right]$, where r is the interparticle distance, σ is a measure of the particle size, ϵ is the interaction strength and $m > 2$,. As density increases, the GEM-m system shows, for $m > 2$, a first-order transition from a fluid of clusters to a cluster bcc-crystal above the triple point temperature, and a subsequent structural phase transition from a cluster bcc to a cluster fcc crystal. This occurs at arbitrarily high temperatures [92, 97], contrary to the case of Q^{+}-systems, which exhibit reentrant crystallization in the temperature-density plane [90]. A remarkable feature of the cluster fcc crystals is that upon increasing the density the lattice constant approaches a constant value $a_{\text{fcc}} = 2\pi\sqrt{3}/q^*$, with q^* the wave vector at which $\hat{v}(q)$ takes its absolute minimum. An obvious consequence of the density-independent value of a_{fcc} is that the population of each lattice site scales proportionally with density. These properties are rather different from usual crystallization features in colloidal systems. Moreover, these differences are not restricted to the structural properties but also to the dynamical ones. Regarding the slow dynamics in such cluster crystals, incessant hopping between clusters has been revealed, which fully changes the initial identity of the clusters without altering the lattice structure. Another peculiar dynamic feature of these systems is a decoupling between self- and collective out-of-lattice correlations [120, 121].

Recently, the phase behavior of mixtures containing a non-clustering component ($m = 2$) and a clustering component ($m = 4$) has been investigated within the framework of the Density Functional Theory (DFT) [101, 102]. For the case of non-demixing systems, evidence was found for the formation of novel kinds of alloys, i.e. mixed cluster crystals [102]. Though static features of these mixtures have been studied in detail, to the best of our knowledge no information has been reported on the corresponding dynamical aspects. This article aims to shed light on such aspects. By means of extensive molecular dynamics (MD) simulations, the findings displayed by one-component cluster crystals [120, 121] are extended to mixtures of clustering and non-clustering particles. Analogies and differences with the one-component case are revealed and discussed by analyzing self- and collective dynamic correlators. This chapter is organized as follows: Model and simulation details are given in Sec. 5.2. The static and dynamic features are presented and discussed in Sec. 5.3. Finally, some concluding remarks are given in Sec. 5.4.

5.2 Model and Simulation

We are interested in the dynamical behavior of non-demixing systems, i.e., binary mixtures for which the fluid-fluid macrophase separation (demixing) is preempted by crystallization. In this way, the first step was to study the stability limits of the homogeneous fluid against either macrophase separation or crystallization for representative examples of the former class of mixtures. The aim was to find a system whose demixing binodal line lies well above the λ-line in the concentration-density plane. A precise definition of the λ-line is given below. Both binodal and λ lines were obtained by solving the Ornstein-Zernike equation within the mean field approximation (MFA, see Appendix B) [41]. Based on such results, the specific systems to be simulated were determined and thus the parameters defining the mixture (relative particle size, mixture compositions, temperature and density, self- and cross-interactions) were chosen in such a way as to avoid the region of demixing in the phase diagram. Because of the high total densities to be considered, the former parameters were also selected with the goal of reducing computational expense.

The investigated system was a mixture of big GEM-8 particles and small GEM-2 (gaussian) particles. This mixture contains a non-clustering component (GEM-2, in the following referred as A-particles) and a cluster-forming component (GEM-8, in the following referred as B-particles). The dynamic features of this system were investigated at fixed temperature T for a broad range of densities $\rho = \rho_A + \rho_B$ and several relative compositions $x = \rho_B/\rho$. The former densities are defined as $\rho_\alpha = N_\alpha/V$, N_α being the number of particles of the species α and V the total volume. In what follows, we choose units in which Boltzmann's constant k_B has the value $k_\mathrm{B} = 1$. The cross-interaction was chosen to be a GEM-4 potential, which also displays cluster formation. In this way, for the interaction potential,

$$v_{\alpha\beta}(r) = \epsilon_{\alpha\beta} \exp\left[-\left(\frac{r}{\sigma_{\alpha\beta}}\right)^{m_{\alpha\beta}}\right], \tag{5.1}$$

we used the following parameters: $\epsilon_{\alpha\beta} = \epsilon = 1.0$, $\sigma_{AA} = 0.3\sigma$, $\sigma_{AB} = 0.6\sigma$, $\sigma_{BB} = \sigma = 1.0$, and $m_{AA} = 2$, $m_{AB} = 4$, $m_{BB} = 8$. With these parameters, a common cutoff range $R_c = 1.5\sigma$ was introduced in the simulation for all the interactions.

MD simulations were performed in a cubic box with periodic boundary conditions. The equations of motion were integrated in the velocity Verlet scheme [122], with a time step $\Delta t/\tau$ ranging from 0.001 to 0.005, where $\tau = \sqrt{m\sigma^2/\epsilon}$ and a common mass $m = 1$ was used for all the particles. The size of the simulation box, L_{box}, was typically of 7 or 8 times the lattice constant a_{fcc} of the considered mixture. The value of a_{fcc} was obtained from DFT as explained in [101, 102]. In the following, density, time, distance, and wave vector will be given, respectively, in units of σ^{-3}, τ, σ, and σ^{-1}. Initial configurations were generated by placing the particles uniformly at the sites of the fcc lattice defined by a_{fcc}. An equilibration run was performed in which the system was thermalized at temperature $T = 0.30$ by periodic velocity rescaling. Typical equilibration times ranged from 2×10^5 to 2×10^6 time steps according to the studied density. After reaching equilibrium, manifested by the absence of any drift in internal energy and pressure, a production run was performed in the microcanonical ensemble, at different densities, for compositions $x = 0.65$, 0.80 and 0.95. Typical production runs ranged from 10^6 to 10^8 time steps.

5.3 Results and Discussion

5.3.1 Phase diagram and static structure

The partial structure factors $S_{\alpha\beta}(q)$ $(\alpha, \beta \in \{A, B\})$ are related to the propensity of a fluid to sustain spontaneous density fluctuations of wave vector q. They are defined as

$$S_{\alpha\beta}(q) = \frac{\langle \rho_\alpha(\mathbf{q}, 0)\rho_\beta(-\mathbf{q}, 0)\rangle}{\sqrt{N_\alpha N_\beta}} \tag{5.2}$$

x	ρ^*	q^*	a_{fcc}	L_{box}
0.65	1.68	5.64	1.9296	13.5070
0.80	1.46	5.74	1.8960	15.1677
0.95	1.29	5.84	1.8635	14.9079
1.00	1.25	5.86	1.8571	14.8571

Table 5.1: For each investigated composition x, density ρ^* for the λ-line, parameters defining the fcc lattice ($D(q^*) = 0$, $a_{\mathrm{fcc}} = 2\pi\sqrt{3}/q^*$, see [101]) and box size L_{box} used in the MD.

with $\rho_\alpha(\mathbf{q}, t) = \sum_{j=1}^{N_\alpha} \exp[i\,\mathbf{q}\cdot\mathbf{r}_j^\alpha(t)]$ and the sum is performed over the coordinates $\mathbf{r}_j^\alpha$ of all particles belonging to the species α.[1] According to the OZ equations, they take, in the homogeneous phase, the generic form $S_{\alpha\beta}(q) = N_{\alpha\beta}(q)/D(q)$ where, within the MFA, the denominator depends on the Fourier transform of the interaction potentials according to

$$D(q) = 1 + \frac{\rho}{T}\hat{U}_s(q) + \left(\frac{\rho}{T}\right)^2 x(1-x)\hat{U}_d(q), \tag{5.3}$$

where $\hat{U}_s(q) = (1-x)\hat{v}_{AA}(q) + x\hat{v}_{BB}(q)$ and $\hat{U}_d(q) = \hat{v}_{AA}(q)\hat{v}_{BB}(q) - \hat{v}_{AB}^2(q)$ [101]. Due to their generic form, the partial structure factors will diverge for all those conditions where $D(q) = 0$, and therefore the homogeneous fluid will be unstable. If the divergence takes place at $q = 0$, demixing occurs and the spinodal line denotes the locus of state points where $D(0) = 0$. On the other hand, a divergence at some $q^* > 0$ signals an instability in the fluid (which is referred as Kirkwood instability) with respect to a periodic modulation of the density. The locus of state points where this instability takes place corresponds to the so-called λ-line [102].

For the system at hand, the last scenario is indeed the case, where the instability dominating the phase behavior is mainly due to the $Q^\pm$-nature of the species

---

[1] For uniform phases, the statistical average $\langle\cdots\rangle$ in the right hand side of Eq. (5.2) above renders its left hand side a function of $q = |\mathbf{q}|$ only. For the crystalline phases to be considered in what follows, we have performed an additional rotational average over symmetry-related values of the reciprocal vectors, so that the resulting quantities (static and time-dependent correlation functions) are shown as functions of q only.

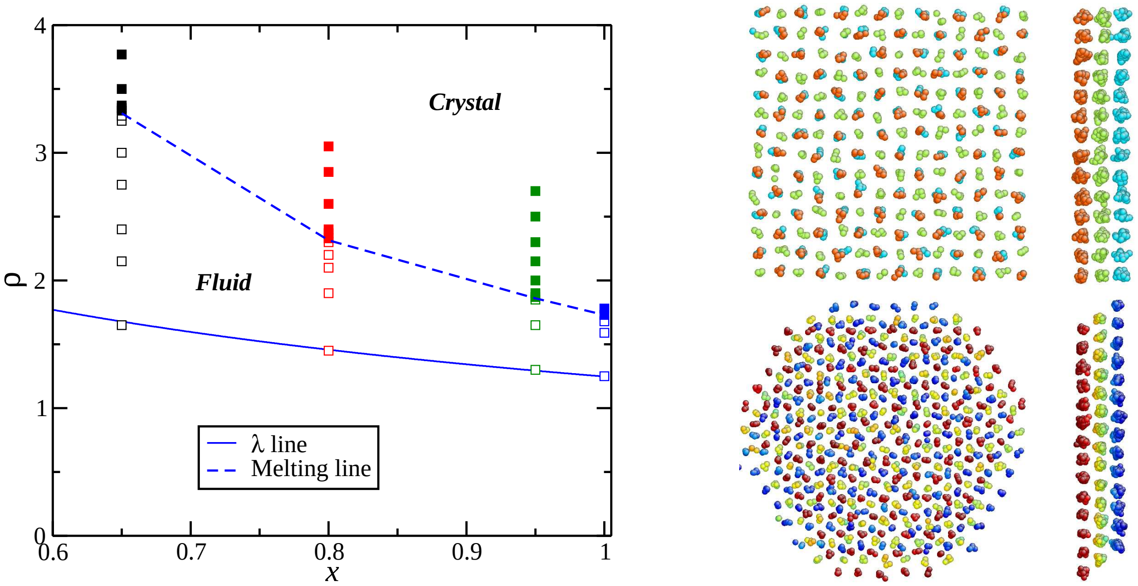

Figure 5.1: Left: A segment, at the high-x/moderate ρ region, of the phase diagram of the studied ultrasoft mixture. Empty and filled symbols indicate the simulated state points in the (ρ, x)-plane, at both sides of the melting line. The latter is displayed as a dashed guideline for the eyes. It is estimated from the emergence of Bragg peaks in the partial static structure factors (see below). The solid line is the λ-line, obtained from the OZ-MFA equations. Right: Slabs of the simulation box for $x = 0.65$ and $\rho = 3.50$, parallel to the (001)-plane (top) and to the (111)-plane (bottom). For the sake of clarity, only GEM-8 particles are displayed, in both frontal and lateral views, with a size much smaller than the real σ. Particles in different layers are represented with different colors.

B. Figure 5.1 displays the corresponding λ-line in the (x, ρ)-plane estimated from MFA. Since this line is related to the limit of stability for the homogeneous fluid phase, it is expected that close to it the system will tend to crystallize into solids whose lattice constant will be dictated by q^* (see Table 5.3.1). By visual inspection of the configuration snapshots, state points for which the initial crystal structure was stable were discriminated from those for which the latter melted. The melting line estimated in this way was consistent with the analysis of Bragg peaks in the partial structure factors (see below). No transition to other crystalline structures was observed during the simulations, confirming the fcc structure as the underlying lattice in the investigated crystalline states. The typical snapshots of Fig. 5.1 indeed exhibit the expected ABC staking of the (111)-planes. It should be noted that the apparent contradiction of having, in Fig. 5.1, a fluid phase that is stable *beyond* the λ-line is an artefact arising from applying the MFA in calculating the latter. The MFA becomes increasingly accurate at T grows, whereas we are working here at $T = 0.3$. Nevertheless, this has no consequences in what follows, since we are employing the MFA λ-line merely as an indicator of the region in which alloy formation (crystallization) is expected, without basing any further quantitative predictions on its precise location.

More detailed structural information can be gained by considering the partial radial distribution functions $g_{\alpha\beta}(r)$, which measure the probability to find a pair of particles, of species α and β, at a mutual distance r. In Fig. 5.2 these quantities are displayed for $x = 0.80$ and different densities. As expected, $g_{BB}(r)$ exhibits a large peak at $r = 0$ (namely $g_{BB}(r \to 0) \sim 30$), indicating the formation of clusters, whose size extends up to $d_{\mathrm{c}} \sim 0.75$. The second peak at $r \sim 1.34$ corresponds to the nearest-neighbor distance in the fcc crystal, $d_{\mathrm{nn}} = a_{\mathrm{fcc}}/\sqrt{2}$. The radial distribution function for distinct pairs, $g_{AB}(r)$, displays rather different features. The correlation hole at $r \to 0$ indicates that the small A-particles avoid the lattice sites and tend to localize in the interstitials between B-clusters. Concerning correlations between pairs of A-particles, $g_{AA}(r)$ displays finite small values (~ 0.2) at $r \to 0$. This means that for the considered conditions, no appreciable clustering of the species A is induced by the clustering of the species B.

On increasing the density, a significant structural change occurs in the system,

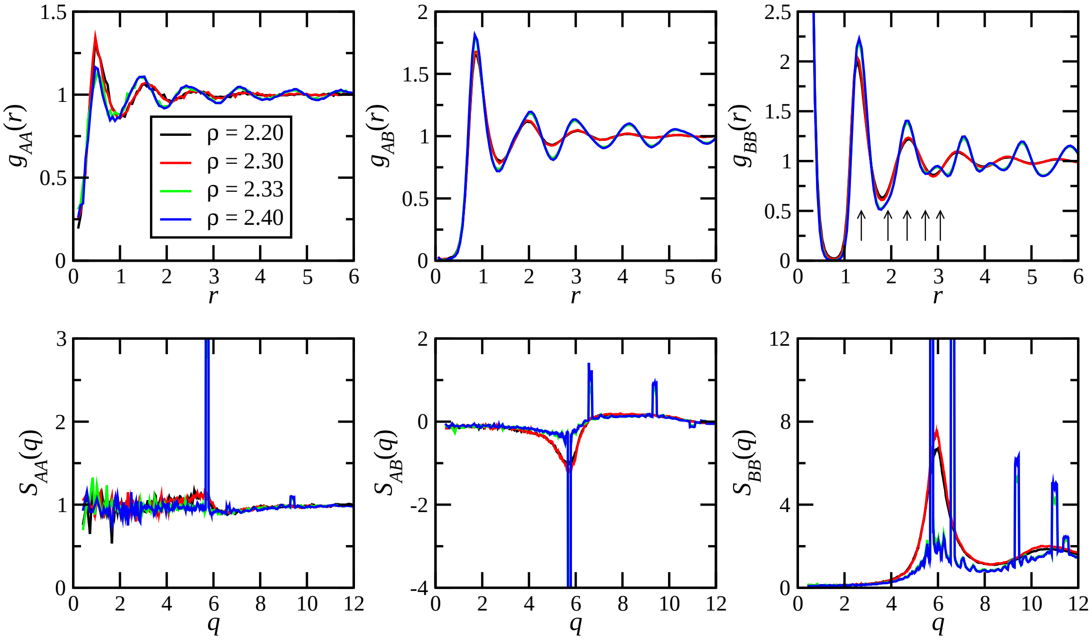

Figure 5.2: Radial distribution functions (top) and structure factors (bottom) for $x = 0.80$ and different densities. The arrows in the plot of $g_{BB}(r)$ indicate the position of the kth-neighbor in a fcc lattice, i.e., $d_k = \sqrt{k}d_{\rm nn} = \sqrt{k/2}\ a_{\rm fcc}$. The values of the selected densities are the same in all panels (see legend for $g_{AA}(r)$).

which is evidenced by the emergence of well-defined peaks of all $g_{\alpha\beta}(r)$ at large distances (see top panels of Fig. 5.2). This change is better reflected in the corresponding partial structure factors $S_{\alpha\beta}(q)$. As shown in bottom panels for the largest densities, the emergence of Bragg peaks in $S_{BB}(q)$ indicates a rather ordered structure, which still retains some characteristics of the fluid phase. On the other hand, the nearly flat structure of $S_{AA}(q)$ clearly suggests the presence of a, nearly ideal, fluid phase of A-particles. This fluid phase is immersed in the crystalline matrix of clusters of B-particles. Strictly speaking, the A-particles form a very weakly modulated fluid, so that the mixture of localized B-particles and delocalized A-particles forms a sublattice melt phase. The one-particle density of the A-particles, however, cannot be strictly uniform, since the crystallized B-particles act on the A-species as a periodically modulated external potential. This structural scenario has its dynamic counterpart, as will be shown below.

The occupation number n of a given lattice site, i.e., the number of B-particles in the associated cluster, is obviously an integer number. The *average* occupation is in general non-integer, as a result of (at least two) significant contributions of distinct values of n all over the lattice. For example, in the crystalline system of composition $x = 0.80$ and density $\rho = 2.40$ around the 65% and 25% of the clusters are composed respectively by three and four B-particles. This percentages were estimated by counting the coordination number of each particle for $r < d_{\mathrm{c}} \sim 0.75$. On passing, it was also estimated by using the same criterion that around 90% of the A-particles are isolated from particles of the same species. The former results reflect that the lattice is full of defects which might be expected to break its stability. As discussed in Ref. [121] for the one-component cluster crystal, the stability of the lattice is actually maintained by incessant hopping of the B-particles between distinct clusters. This is also the case in the mixtures considered here, as discussed in the next subsection.

5.3.2 Dynamics in real space

A first step to gain some insight into the transport properties of the system is provided by the mean squared displacement $\langle \Delta r_{\alpha}^{2}(t) \rangle$ (MSD). This quantity is shown in Fig. 5.3 for different densities and relative compositions $x = 0.65$ and $x = 0.95$. In the case of the A-particles, a rapid crossover is observed for all the investigated densities, between short-time ballistic motion ($\langle \Delta r_{\alpha}^{2}(t) \rangle \propto t^{2}$) and long-time diffusion ($\langle \Delta r_{\alpha}^{2}(t) \rangle \propto t$). This is the usual dynamic behavior of a highly mobile fluid phase. Thus, as anticipated by the static correlations, the mixture reaches a phase in which the species A shows a fluid-like behavior in a crystalline matrix of clusters of B-particles. This behavior is reminiscent of that of the superionic phase of AgI and CuI, which is characterized by a dynamic disorder of cations between the tetrahedral interstices formed by the fcc anion sublattices [123, 124, 125].

The MSD of the B-particles shows a similar behavior in the fluid phase. However, an abrupt dynamic change is revealed by crossing the crystallization point. Thus, an intermediate plateau regime arises between the ballistic and diffusive limits, ex-

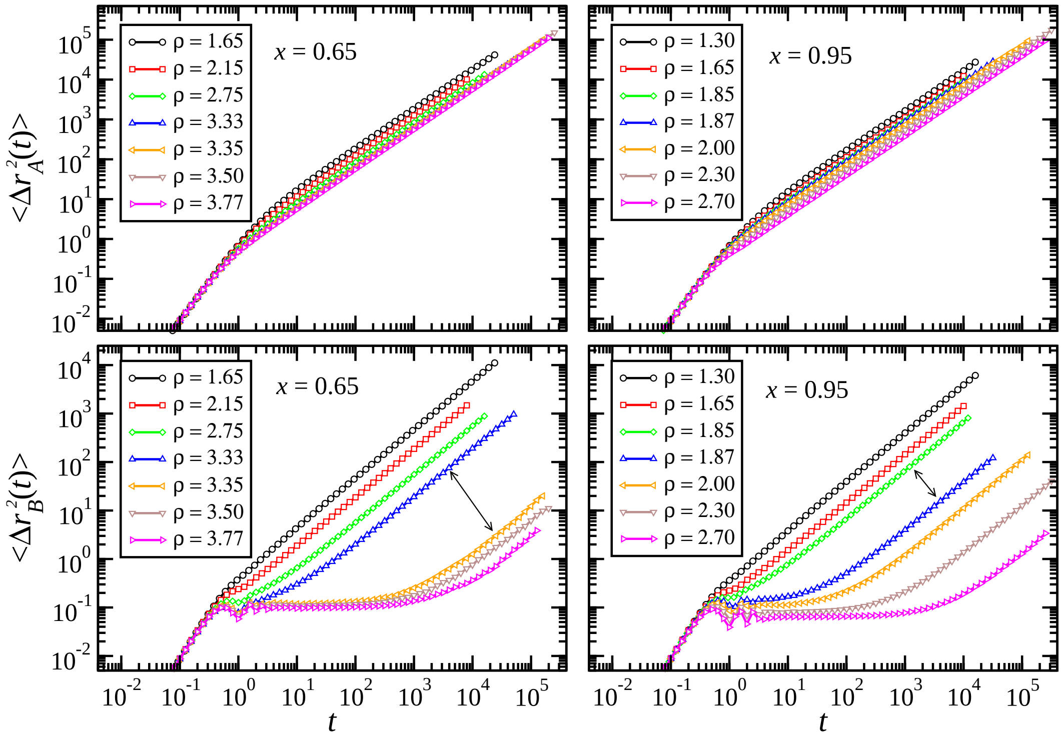

Figure 5.3: MSD of both species for $x = 0.65$ (left panels) and $x = 0.95$ (right panels). The arrows in bottom panels separate fluid states for the B-particles from crystal clusters (see also Fig. 5.1).

tending over longer time intervals as density increases. This regime is associated with the temporary trapping of the B-particles within the clusters [120, 121]. The large oscillations at the beginning of the plateau regime are the signature of strong intracluster vibrational motion. Such short-time strong oscillations are an artifact of the simulated Newtonian dynamics. They are expected to be strongly damped under more realistic Brownian dynamics (BD); it has been shown that they even vanish in Monte Carlo (MC) simulations [126]. Finally, at long times, the MSD displays a crossover to diffusive behavior. This scenario, which has been previously observed in the cluster crystal phase of the pure GEM-8 system [120, 121], does not originate from the contribution to the MSD of rare events involving a few diffusing B-particles. As anticipated above, it is the result of incessant hopping of B-particles between neighboring lattice sites. Thus, the hopping mechanism fully changes the

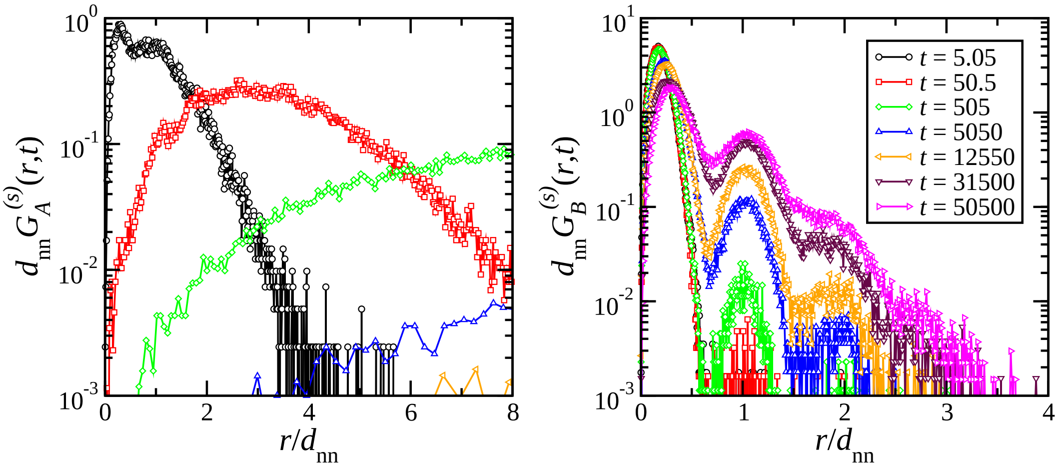

Figure 5.4: Van Hove self-correlation function at different times for $x = 0.80$ and $\rho = 3.05$ (left: A-particles, right: B-particles). Distances are rescaled by $d_{\rm nn}$.

initial identity of each cluster without altering the overall crystalline lattice structure [120, 121].

This hopping mechanism is clearly reflected in the van Hove self-correlation of the B-particles, which can be evaluated from

$$G_\alpha^{(\mathrm{s})}(r,t) = \frac{1}{N_\alpha}\left\langle \sum_{j=1}^{N_\alpha} \delta\left[\mathbf{r} - \mathbf{r}_j^\alpha(t) + \mathbf{r}_j^\alpha(0)\right]\right\rangle . \tag{5.4}$$

Figure 5.4 shows a representative example for composition $x = 0.80$ and density $\rho = 3.05$. A sequence of well-defined peaks is present in $G_B^{(s)}(r,t)$, corresponding to different distances between lattice sites. With increasing time, the first peak in $G_B^{(\mathrm{s})}(r,t)$ decreases while peaks located at larger distances grow progressively, corresponding to particles moving away from their original home clusters. By simple integration of $G_B^{(s)}(r,t)$ from its first minimum to $r \to \infty$, it is found that only the 30% of the B-particles are located at $t \sim 5 \times 10^4$ in their initial home cluster. As expected from the observations in the MSD (see above) the van Hove self-function for the non-clustering species A displays a simpler behavior. For $t \sim 50$ the initial peak at $r \approx 0.3$ has already vanished. At that time scale almost all the A-particles have left their initial interstitial positions and $G_A^{(\mathrm{s})}(r,t)$ exhibits simple Gaussian behavior.

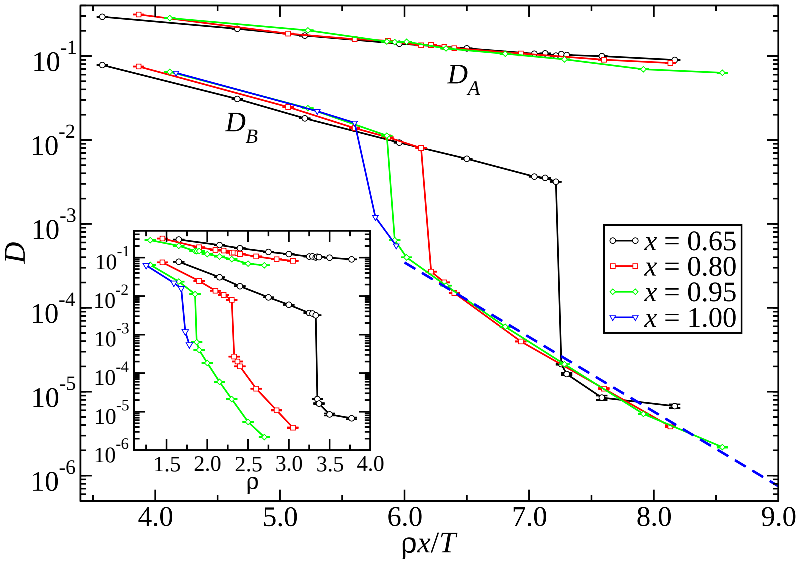

Figure 5.5: Diffusivities of the A- and B-particles as a function of the density (inset) and of the combined variable $\rho x/T$ (main panel). Solid lines are guides for the eyes. The dashed line in the main panel indicates approximate Arrhenius behavior $D_B \sim \exp[-2.3\rho_B/T]$.

We can estimate the diffusivity of each species from the Einstein relation $D_\alpha = \lim_{t\to\infty} \langle \Delta r_\alpha^2(t) \rangle /6t$. Figure 5.5 shows the obtained results as a function of the quantity $\rho_B/T = \rho x/T$. For each composition x, an abrupt drop in the diffusivity of the B-particles is observed in a narrow range of density. This drop reflects the transition of the species B from the fluid to the cluster crystal, and it is indeed expected from the previous observations in the MSD (see Fig. 5.3). The approximate scaling behavior for D_B in the cluster crystal phase generalizes the observation for the pure GEM-8 system [120, 121]. The latter was rationalized as the result of activated hopping motion between minima of the local potential energy U, i.e, that experienced by a test particle in the system[2]. By computing the map of U along

---

[2] This hopping scenario shows striking analogies, both for van Hove functions and potential energy profiles, with the layer-to-layer diffusion of rods in smectic phases (see Ref. [129, 130, 131]). In such systems the corresponding energy barriers separate minima located *in the centers* of the layers. The incoherent scattering functions of the rods and the B-particles (see Sec. 5.3.3) also exhibit similar trends [131, 132, 133].

the simulation box, it was found that such minima are placed at the lattice sites [120, 121, 127, 128, 129, 130, 131, 132, 133]. It was also found that the separating energy barrier between neighboring sites scales as $\Delta U \approx 2.3\rho_B$, leading to Arrhenius behavior $D_B \sim \exp[-\Delta U/T]$ [120, 121]. Data in Fig. 5.5 show that this observation is not altered in the mixture over a broad range of values of $\rho x/T$. The introduction of the non-clustering A-particles does not even change significantly the former activation energy ΔU.

5.3.3 Scattering functions

Relaxation of density fluctuations of wave vector q are evaluated by means of the intermediate coherent and incoherent scattering functions. The coherent function is defined as

$$F_{\alpha\beta}(q,t) = \frac{\langle \rho_\alpha(\mathbf{q},t)\rho_\beta(-\mathbf{q},0)\rangle}{\langle \rho_\alpha(\mathbf{q},0)\rho_\beta(-\mathbf{q},0)\rangle} \tag{5.5}$$

and characterizes collective α-β correlations, whereas the incoherent function accounts for self-correlations and is given by

$$F_\alpha^{(\mathrm{s})}(q,t) = \frac{1}{N_\alpha}\left\langle \sum_{j=1}^{N_\alpha} \exp\{i\,\mathbf{q}\cdot[\mathbf{r}_j^\alpha(t) - \mathbf{r}_j^\alpha(0)]\}\right\rangle . \tag{5.6}$$

With the used normalizations $F_{\alpha\beta}(q,0) = F_\alpha^{(\mathrm{s})}(q,0) = 1$. Figure 5.6 shows results of the scattering functions for composition $x = 0.95$ at densities above and below the crystallization line. The selected value of $q = 4.0$ is not a reciprocal lattice vector (RLV) and therefore data in this figure reflect relaxation of out-of-lattice correlations. Consistently with the observations in the real space, both incoherent and coherent functions for the species A exhibit a fast decay at all the investigated densities, also for those where the B-particles form a cluster crystal. This is reminiscent of the scenario presented for the small particles in Yukawa mixtures immediately below the crystallization temperature [134]. In close similarity to the aforementioned work, our data reveal, for the crystalline phase, a weak oscillation at $t \sim 2$, immediately after the microscopic decay. It reflects short-time vibrational dynamics of the A-particles within the interstitials. This effect was not detected in

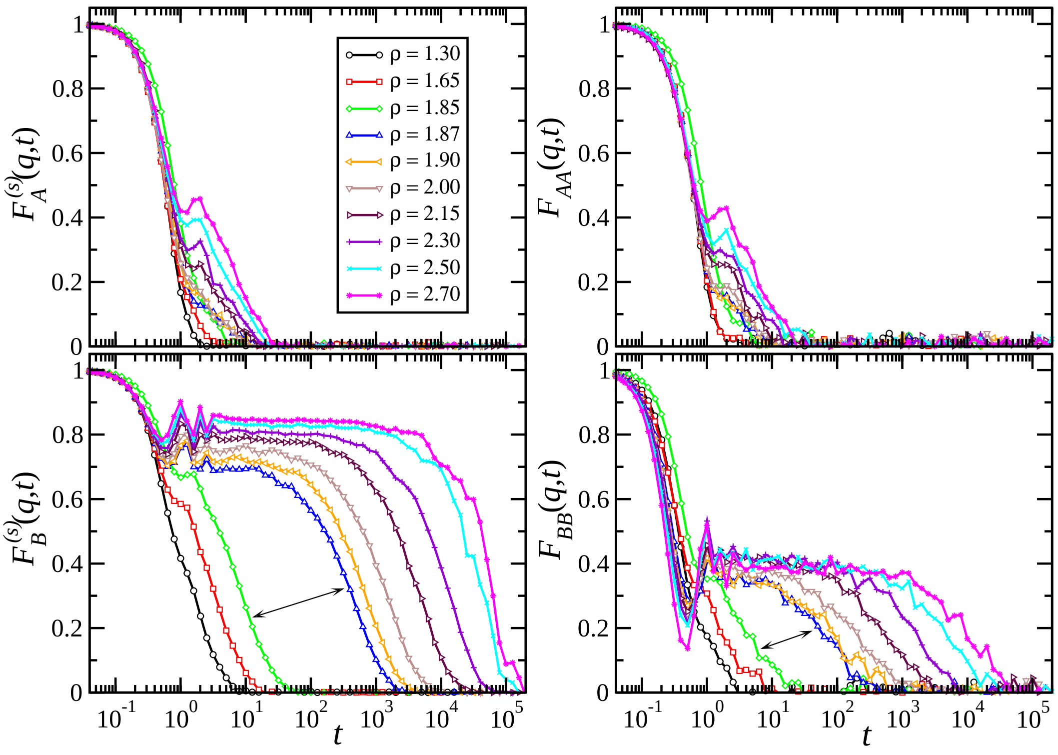

Figure 5.6: Intermediate incoherent and coherent scattering functions for fixed $x = 0.95$ and $q = 4.0$, at different densities. The arrows in bottom panels separate fluid states for the B-particles from crystal clusters (see also Fig. 5.1).

the respective MSD, possibly because contrary to the scattering functions, the former is generally dominated by fast contributions, which may mask the oscillations. As discussed above, these short-time oscillations and the similar ones observed for the scattering functions of the B-particles (Figs. 5.6 and 5.7) are artifacts of the Newtonian dynamics and will be strongly damped or even vanish for BD and MC simulations.

Concerning the dynamics of the clustering B-particles, the present system exhibits more complex features than usual crystals. As in real-space quantities, coherent and incoherent functions reflect an abrupt slowing down of the dynamics by crossing the crystallization point. The intermediate plateau regime extends over longer time intervals as density increases, before the ultimate relaxation at long times. This observation is reminiscent of the usual dynamic scenario associated to the glass transition. Having noted this, distinct features are revealed by inspection of incoherent and coherent functions. Thus, the relaxation of the coherent function $F_{BB}(q,t)$ in the cluster crystal phase is consistent within statistics with a same plateau height (Debye-Waller factor, f_q) for all the investigated densities. This is not the case for the incoherent function $F_B^{(\mathrm{s})}(q,t)$, where the plateau height (Lamb-Mössbauer factor, $f_q^{(\mathrm{s})}$) clearly grows up as density increases.

The usual observation in glass-forming systems is that both Debye-Waller and Lamb-Mössbauer factors remain constant on approaching the glass transition from the ergodic phase. On crossing the transition and moving deep into the glassy phase, the former factors f_q and $f_q^{(\mathrm{s})}$ progressively increase. This feature reflects the progressive decrease of the localization length respectively associated to collective and self-motions. With these ideas in mind, the increase of the plateau height in the incoherent functions for the B-particles (see Fig. 5.6) suggests that a localization transition has occurred for the self-motions, tentatively at the crystallization density. On the contrary, such a transition is not detected for out-of-lattice collective correlations at any of the investigated crystalline states. This dynamic decoupling, in the meaning of a different locus for the localization transitions of self- and out-of-lattice collective motions, is also present in the pure cluster crystal [120, 121]. Having noted this, the ergodicity of self-motions is, as in the pure GEM-8 system, restored at long times. This is reflected in the full decay of $F_{\mathrm{B}}^{(\mathrm{s})}(q,t)$. In other words, the localization transition for self-motions of the B-particles is actually avoided. The mechanism which restores ergodicity of self-motions is naturally the incessant hopping between neighboring clusters discussed above. Qualitatively similar findings are observed for the other studied compositions $x = 0.8$ and $x = 0.65$. Thus, the addition of non-clustering A-particles, even up to a 35% of the total, does not alter the former scenario of dynamic decoupling in the B-particles, and the (avoided by hopping) localization transition for self-motions still occurs at much lower densities that for out-of-lattice collective correlations.[3]

---

[3] It should be mentioned, however, that although the A-particles constitute 35% of the *number density* of the system, they only account for less that 1% of its *volume fraction* due to their much smaller size.

As discussed in Refs. [120, 121], the former scenario has similarities and differences with the dynamics in plastic crystals, where molecules are constrained to vibrate around lattice sites, but perform full rotations which relax out-of-lattice collective correlations. In the case of cluster crystals, cluster deformation constitutes an additional mechanism of relaxation for such correlations. However, contrary to the case of plastic crystals, self-motions can explore arbitrarily long distances in cluster crystals by means of activated hopping. This leads to non-zero diffusivities (Fig. 5.5) and full relaxation of incoherent scattering functions (Fig. 5.6).

As discussed above, the data presented in Fig. 5.6 for a selected non-RLV $q = 4.0$ display similar features, in the case of the species B, to those of the pure GEM-8 system. Novel features are revealed for both species when the scattering functions are represented as a function of q. This is demonstrated in Fig. 5.7 for a fixed crystalline state point, $x = 0.95$, $\rho = 2.70$, and for different values of q, including RLVs and non-RLVs. In the case of the A-particles, the incoherent function displays no signatures of glassy dynamics, but a fast decay for all the wave vectors. This is also the case for the coherent function at non-RLVs. Indeed the respective time scales are very similar for common q. However, a strong decoupling between self- and collective dynamics is observed for RLVs. Contrary to the incoherent case, the coherent function exhibits a plateau over several decades before relaxation at long times.

This dynamic decoupling is rather different from that above discussed for the species B at non-RLVs. On the contrary, it is somewhat reminiscent of the scenario displayed by the small particles in *disordered* binary mixtures for certain ranges of composition and size ratio [135, 136]. In such systems the small particles move along a channel-like structure, formed by the interstitials of a matrix of large particles which relaxes in a much longer time scale, or which is even in the glassy state. As a consequence of the quasistatic arrangement of the interstitials, collective correlations of the small particles decay very slowly, despite fast self-motions are performed, allowing for the exploration of large distances. Thus, decoupling of incoherent and coherent scattering functions of the small particles is observed in all the range of low and moderate wave vectors which probe the matrix structure [135, 136]. As discussed above, for the species A of the mixtures here investigated, the former decoupling is

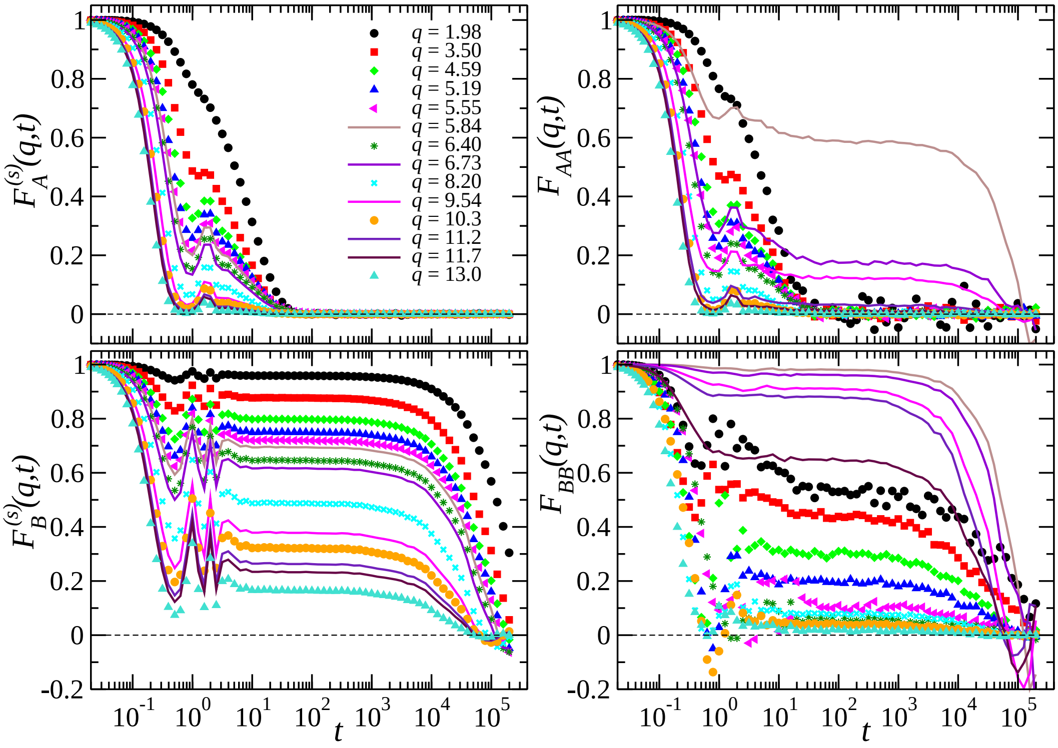

Figure 5.7: Intermediate incoherent and coherent scattering functions for fixed $x = 0.95$ and $\rho = 2.70$, at different wave vectors. Solid lines and symbols correspond respectively to RLVs and to non-RLVs. The dashed lines indicate the zero value of the correlators.

only observed for RLVs. This reflects the fact that the non-clustering particles are preferentially located at the interstitials between the B-clusters, as was seen in the static correlation functions (Fig. 5.2), and therefore also move preferentially between them. Since collective correlations between interstitial positions are probed by the RLVs, a decoupling between incoherent and coherent dynamics is observed for such wave vectors, in analogy with the scenario discussed above for disordered mixtures.

Concerning the scattering functions of the clustering species B, slow relaxation is observed for the incoherent and coherent cases, and both for RLVs and non-RLVs. As usual, Lamb-Mössbauer factors show a monotonic q-dependence, while Debye-Waller factors follow the modulations of the structure factor. Having noted this, coherent functions reveal non-trivial differences between RLVs and non-RLVs at the longest times of the simulation window. Namely, $F_{BB}(q,t)$ exhibits, for RLVs, an oscillation around $t \sim 10^5$. This oscillation is apparently absent for non-RLVs.

For the sake of clarity, the former data for the RLVs are shown separately in Fig. 5.8 over a time window $t > 10$. Given the large amplitude of the long-time anticorrelations, reaching values of $F_{BB}(q,t) \cong -0.2$ at the minimum, it is improbable that the oscillation around $t \sim 10^5$ is an statistical artifact. The figure also includes coherent data, at its respective RLVs, of the pure GEM-8 system at $\rho = 3.0$ and $T = 0.40$. The rather different behavior in the pure system and in the mixture, even with only a 5% of A-particles in the latter, becomes evident. While full relaxation followed by oscillation is observed in the mixture, no decay is present in the pure cluster crystal. It must be stressed that this difference is not related to a much slower intrinsic dynamics of the pure system for the selected state point $\rho = 3.0$ and $T = 0.40$. Indeed, by inspection of all the other dynamic observables introduced above, including coherent functions *for non-RLVs*, it is found that the pure system shows a faster dynamics than the mixture at the former state points. For example $D_B \approx 2 \times 10^{-6}$ and 10^{-5} respectively for the mixture and the pure system. Therefore, the oscillatory feature observed at long times in the mixture is induced by the addition of the gaussian A-particles.

The presence of negative correlations in the collective dynamics of B-particles at near RLV-wavevectors, reached at typical times $\tau_a \sim 10^5$, is a particular feature of the mixture, which is absent for the pure B system within the simulated time window. Physically, it describes a process by which a positive density correlation at $t = 0$ at a distance of the order of the lattice constant turns negative at time scales τ_a. As such, it points to the existence of some characteristic oscillation frequency $\omega_a \sim \tau_a^{-1}$, which corresponds to wavevectors lying at the edge of the Brillouin zone, i.e., a short-wavelength acoustical mode. Although such a process has not been seen for the pure B-system, phonon excitations exist for the pure system as well; it is thus reasonable to assume that the corresponding frequency for the pure system is much smaller that ω_a, so that the time required for this relaxation process to be seen in the coherent scattering intensities is much longer. A detailed calculation of the phonon spectra of the mixture at hand, along parallel lines to the one recently carried out

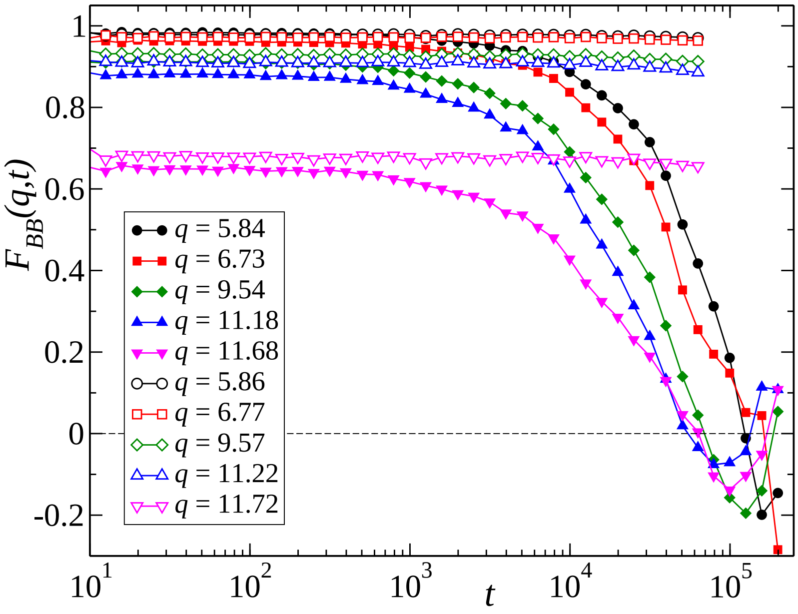

Figure 5.8: Intermediate coherent scattering functions of B-particles for several RLVs. Filled symbols correspond to the mixture with $x = 0.95$, $\rho = 2.70$, and $T = 0.30$. Empty symbols correspond to the pure GEM-8 system with $\rho = 3.0$ and $T = 0.40$. Solid lines are guides for the eyes. The dashed line indicates the level $F_{BB}(q,t) = 0$.

for pure systems [137] would shed light into this question, it is however cumbersome and it will be left as the subject of a future investigation. Nevertheless, in view of the fact that the A-particles provide additional repulsions to the B-species and thus enhance the restoring forces that act on the latter, it appears plausible that in the mixture the phonon frequencies are larger than those in the pure system and thus the characteristic time τ_a becomes visible within the simulation window. Alternatively, the issue could also be resolved by performing very long simulations for the pure B-system.

5.4 Conclusions

The dynamic aspects of binary mixtures of ultrasoft (GEM-8 and gaussian) particles have been studied by means of MD. The present work extends previous results for the cluster crystal phase of the pure GEM-8 system, and investigates the effects of the addition of the non-clustering gaussian particles on the corresponding dynamic scenario. The obtained results show that as the total density increases at fixed composition, the GEM-8 species builds cluster crystals with a relatively high localization. As in the one-component system, the incoherent scattering functions indicate a localization transition for self-motions of the GEM-8 particles, which is avoided by incessant hopping motion between clusters. This transition seems to occur at lower densities than for out-of-lattice collective correlations, confirming in the mixture the dynamic decoupling observed in the one-component cluster crystal.

On the other hand, the gaussian particles remain delocalized in the periodic potential induced by the GEM-8 clusters and display fast self-motions. However, slow collective dynamics is observed for specific wave vectors, namely those belonging to the reciprocal lattice. This feature reflects the preferential motion of the gaussian particles over the interstitials, confirming the expectations from static correlations. A striking feature is revealed by the analysis of collective correlations of the GEM-8 particles, for wave vectors at the reciprocal lattice, a feature which we attribute to the stiffening of an acoustical mode at the edge of the Brillouin zone, caused by the presence of the A-particles.

An additional open question that should be the subject of future investigations is the influence of the *type* of elementary processes employed to model the dynamics in the mixture, along the lines of the work by Coslovich *et al.* carried out for pure systems [126]. Here, it should be examined which of the features discovered by means of our MD approach survive if one employs Monte Carlo moves instead, which are expected to mimic better the overdamped, Brownian Dynamics of the system. Another fundamental question to investigate is how the distinct aspects revealing dynamic heterogeneities in glass-formers [138] are modified in cluster crystals.

Finally, though a direct experimental evidence is still lacking, a very recent simulation study indeed demonstrates the predictions based on the (zero-density limit) GEM potential in the case of amphiphilic dendrimers [139]. By means of monomer-resolved MC simulations, it was found that they form a homogeneous fluid at low density, which, upon a density increase, spontaneously transforms into a fluid of clusters. A clear signature of an active exchange of single dendrimers between different clusters was also reported. These conclusions make us quite confident of the reliability of the coarse-grained results for dense systems presented in this section.

Acknowledgments: I would like to express my gratitude to Dr. Angel Moreno for his hospitality at Donostia International Physics Center (DIPC, San Sebastian, Spain), where simulations were carried out. This work has been supported by the projects NMP3-CT-2004-502235 (Network of Excellence SoftComp, EU) and ITN-234810-COMPLOIDS (Marie Curie Training Network, EU).

Chapter 6

Conclusion and Overview

In this thesis we presented two coarse-grained models for binary mixtures of soft-colloids. The corresponding effective interaction potentials have been used to predict theoretically both the structural correlations and the phase states of the mixtures. Our work was motivated by the growing field of research in which deformable and penetrable (spherical) colloids are mixed with macromolecular additives.

The first considered system was a star-linear polymer mixture in good solvent conditions, which was modeled by means of a recently-developed coarse-grain approach [31]. In this case, the softness of the colloid depends on a single, well-defined parameter, i.e. the functionality of the star (f). We have restricted ourselves to the low/intermediate functionality regime ($f < 32$), which until now was not systematically explored. For this regime, fluid-fluid separation (demixing transition) was found at high enough chain density, which proceeds from a previous clustering. Upon the addition of linear chains, stars begin to form clusters, which in response to a further increase of the chain density, *loosely* bond each other completing a transient non-percolating network. This network becomes unstable and eventually the mixture will phase-separate.

In a similar way that in the conventional realm of colloid-polymer mixtures, we carried out a second coarse-graining and introduced a chain-modified star-star effective interaction, which brings out a depletion-like picture. The resulting depletion potentials have ranges that exceed those needed for phase separation and they can become very deep under addition of sufficient polymer. Furthermore, in strong contrast with both hard sphere mixtures and colloid/non-adsorbing polymer mixtures, the range of the depletion interaction did not show a pronounced dependence on the size of the depletant polymer.

Out results directly imply that mixtures of soft colloids with linear polymer will undergo a fluid-fluid phase separation independently of the polymer size and, subsequently will also show arrested spinodal decomposition, provide that the colloid density is high enough [13]. Naturally, the latter scenario will disappear when the (soft) colloids themselves do not arrest, which is indeed the case for low-functionality stars. We expect these results to hold for most core-shell particle systems, inasmuch as they can be interpreted in terms of the penetrability of the star soft-shell, as long as it is thick enough to accommodate the small chains in their full extent.

In addition, we successfully tested theoretical results of our model against experimental measurements of mixtures of star-like micelles and linear polymers. Without any adjustable parameter, i.e., all quantities entering the theory (sizes of the two components, star functionality and their concentrations) being simply read-off from experiments, we find quantitative agreement between experiments and theory for the influence of the added chains on the the structural correlations and the rheological states of the mixture. In this way, the accuracy of the coarse-graining procedure has been demonstrated for a range of concentrated mixtures with nontrivial spatial correlations, clearly corroborating the success of coarse-graining beyond simulations, in which a full, monomer-resolved, concentrated solution is unfeasible.

On the other hand, the second model studied here was a phase-separating binary mixture of GEM particles, in which one component tends to self-assemble into clusters at high density. At the first instance, taking advantage of the mean-field character of the GEM potential, we employed density functional theory, to investigate the interfacial and wetting properties of a (size-symmetric) GEM-2/GEM-4 fluid, which might represent athermal dendrimer/amphibilic dendrimer [96, 97], or linear polymer/ring polymer [35, 99] mixtures. For the free interface, we found that the density profiles of both species display oscillatory decay on both sides of the interface, what was associated to the location of the Fisher-Widom line (FWL). Regarding the wetting of a Yukawa-like repulsive wall, we described a first-order wetting transition which features a layering-like behavior as consequence of the clustering properties of GEM-4 particles. Although our approach can not fully account for it, the possibility to have a cluster two-dimensional crystal close to the wall was discussed.

Finally, we present a simulation study on the dynamics of a binary cluster crystals. With the experience gained in one-component cluster crystals, we carried out a systematic investigation regarding the effect of the addition of a smaller non-clustering component. As the system was made denser, the cluster component can feature a strong change in its dynamics, while the non-clustering one is hardly affected. The latter remains delocalized in the periodic structure of the clustering component and display fast self-motions. Nevertheless, slow collective dynamics is observed for the wave vectors belonging to the reciprocal lattice, reflecting the preferential motion of the small particles over the interstitials. We formulated some analogies and differences with the one-component case, as well as with superionic crystals and smetic liquid crystals. Although evidence of an experimental realization of formation of cluster crystals is still lacking, most recent monomer-resolved simulation results point out that amphiphilic dendrimers are eligible molecules to accomplish this purpose [139].

A current line of intense work concerning coarse-graining techniques is that of the multi-blob representation, whereby a polymer chain is divided into a certain number of blobs. The latter are chosen in a such way that they interact through density-independent, effective pair interactions, allowing to extend all the gained experience in the dilute regime to the semi-dilute/concentrated regimes [140]. The same approximation have been successfully to describe the phase behavior of diblock copolymers, which, in a minimum model, can be mapped onto soft dumbbells [141]. In this way, the different ultrasoft models presented in this work could be useful to further extend the achievements of the multi-blob representation to, e.g., more complex molecular architectures, anisotropic [142] or functionalized particles [143], and their generalization to non-equilibrium situations [144].

Bibliography

[1] A. C. Balazs and J. M. Yeomans, Soft Matter **6**, 703 (2010).

[2] M. A. Cohen Stuart *et al.*, Nature Materials **9**, 101 (2010).

[3] L. Belloni, J. Phys.: Condens. Matter **12**, R549 (2000)

[4] C. N. Likos, Phys. Rep. **348**, 267 (2001)

[5] C. N. Likos, Soft Matter **2**, 478 (2006)

[6] A. R. Denton, in *Nanostructured Soft matter: Experiment, Theory, Simulation and Perspectives*, Ed. AV Zvelindovsky (Springer, Dordrecht, 2007)

[7] M. Wilson, Soft Matter, **5**, 4355 (2009).

[8] C. Peter and K. Kremer, Soft Matter, **5**, 4357 (2009)

[9] Y. Levin, Rep. Prog. Phys. **65**, 1577 (2002)

[10] S. Asakura and F. Oosawa, J. Polym. Sci. **33**, 183 (1958)

[11] A. Vrij, Pure Appl. Chem. **48**, 471 (1976)

[12] V. J. Anderson and H. N. W. Lekkerkerker, Nature **416**, 811 (2002)

[13] E. Zaccarelli, J. Phys.: Condens. Matter **19**, 323101 (2007)

[14] D. Gottwald *et al.*, Phys. Rev. Lett. **92**, 068301 (2004)

[15] F. Scheffold *et al.*, Phys. Rev. Lett. **104**, 128304 (2010)

[16] W. C. K. Poon, J. Phys.: Condens. Matter **14**, R859 (2002)

[17] D. Vlassopoulos, J. Polym. Sci. Part B: Polym. Phys. **42**, 2931 (2004)

[18] B. M. Mladek, *Exotic phenomena in the phase behavior of soft matter systems*, PhD Thesis, Vienna University of Technology (2007)

[19] G. Malescio, J. Phys.: Condens. Matter **19**, 073101 (2007)

[20] M. Dijkstra, J. M. Brader, and R. Evans, J. Phys.: Condens. Matter **11**,10079 (1999)

[21] C. Bechinger *et al.*, Phys. Rev. Lett. **83**, 3960 (1999)

[22] D. Rudhardt, C. Bechinger, and P. Leiderer, J. Phys.: Condens. Matter **11**, 10073 (1999)

[23] R. Roth, R. Evans, and S. Dietrich, Phys. Rev. E **62**, 5360 (2000)

[24] A. A. Louis and R. Roth, J. Phys.: Condens. Matter **13**, L777 (2001)

[25] P. G. Bolhuis and A. A. Louis, Macromolecules **35**, 1860 (2002)

[26] C. N. Likos *et al.*, Phys. Rev. Lett. **80**, 4450 (1998)

[27] M. Watzlawek, C. N. Likos, and H. Löwen, Phys. Rev. Lett. **82**, 5289 (1999)

[28] F. Lo Verso, C. N. Likos, and L. Reatto, Prog. Colloid Polym. Sci. **133**, 78 (2006)

[29] F. Lo Verso *et al.*, Mol. Phys. **104**, 3523 (2006)

[30] A. K. Kandar *et al.*, J. Chem. Phys. **130**, 121102 (2009)

[31] C. Mayer and C. N. Likos, Macromolecules **40**, 1196 (2007)

[32] M. Daoud and J. P. Cotton, J. Phys. (Paris). **43**, 531 (1982)

[33] T. A. and P. A. Pincus, Macromolecules **19**, 2509 (1986)

[34] A. Jusufi, M. Watzlawek, and H. Löwen, Macromolecules **32**, 4470 (1999)

[35] A. A. Louis *et al.*, Phys. Rev. Lett. **85**, 2522 (2000)

[36] P. G. Bolhuis *et al.*, J. Chem. Phys. **114**, 4296 (2001)

[37] V. Krakoviack, J. P. Hansen, and A. A. Louis, Europhys. Lett. **58**, 53 (2002)

[38] A. Jusufi *et al.*, J. Phys.: Condens. Matter **13**, 6177 (2001)

[39] R. L. C. Vink *et al.*, Phys. Rev. E **72**, 030401(R) (2005)

[40] J. Dzubiella, C. N. Likos, and H. Löwen, J. Chem. Phys. **116**, 9518 (2002)

[41] J. P. Hansen and I. R. McDonald, *Theory of simple liquids* (Academic Press, London, 2006)

[42] A. B. Bathia and D. E. Thornton, Phys. Rev. B **2**, 3004 (1970)

[43] C. N. Likos and N. W. Ashcroft, J. Chem. Phys. **97**, 9303 (1992)

[44] M. Konieczny and C. N. Likos, J. Phys.: Condens. Matter, **19**, 076105 (2007)

[45] M. Dijkstra, R. van Roij, and R. Evans, Phys. Rev. E **59**, 5744 (1999)

[46] R. P. Sear and W. M. Gelbart, J. Chem. Phys. **110**, 4582 (1999)

[47] F. Sciortino *et al.*, Phys. Rev. Lett. **93**, 055701 (2004)

[48] S. Mossa *et al.*, Langmuir **20**, 10756 (2004)

[49] E. Stiakakis *et al.*, Phys. Rev. Lett. **89**, 208302 (2002).

[50] E. Stiakakis *et al.*, Europhys. Lett. **72**, 664 (2005)

[51] Y. Liu, W. R. Chen, and S. H. Chen, J. Chem. Phys. **122**, 044507 (2005)

[52] P. J. Lu *et al.*, Phys. Rev. Lett. **96**, 028306 (2006)

[53] P. J. Lu *et al.*, Nature **453**, 499 (2008)

[54] M. Laurati *et al.*, J. Chem. Phys. **130**, 134907 (2009)

[55] A. J. Archer, C. N. Likos, and R. Evans, J. Phys.: Condens. Matter **14**, 12301 (2002)

[56] M. Watzlawek, H. Löwen, and C. N. Likos, J. Phys.: Condens. Matter, **10**, 8189 (1998)

[57] D. Pini *et al.*, Phys. Rev. Lett. **100**, 055703 (2008)

[58] A. Stradner *et al.*, Nature **432**, 492 (2004)

[59] K. N. Pham *et al.*, Science **296**, 104 (2002)

[60] R. Tuinier, J. Rieger, and C. G. de Kruif, Adv. Colloid Interface Sci. **100**, 055703 (2003)

[61] A. A. Louis *et al.*, J. Chem. Phys. **117**, 1893 (2002)

[62] P. G. Bolhuis, A. A. Louis, and J. P. Hansen, Phys. Rev. Lett. **89**, 1283021 (2002)

[63] A. A. Louis *et al.*, Phys. Rev. E. **65**, 061407 (2002)

[64] O. Guzmán and J. J. de Pablo, J. Chem. Phys. **118**, 2392 (2003)

[65] G. Cinacchi *et al.*, J. Chem. Phys. **127**, 214501 (2007)

[66] S. Abbas and T. Lodge, Phys. Rev. Lett. **99**, 137802 (2007)

[67] S. Abbas and T. Lodge, Macromolecules **41**, 8895 (2008)

[68] D. Vlassopoulos *et al.*, J. Phys.: Condens. Matter **13**, R855 (2001)

[69] P. Attard, J. Chem. Phys. **91**, 3083 (1989)

[70] M. Camargo and C. N. Likos, J. Chem. Phys. **130**, 204904 (2009)

[71] F. Lo Verso, M. Tau, and L. Reatto, J. Phys.: Condens. Matter **15**, 1505 (2003).

[72] F. Lo Verso *et al.*, Phys. Rev. E **70**, 061409 (2004)

[73] T. Lodge *et al.*, Phys. Rev. Lett. **89**,145501 (2004)

[74] M. Laurati *et al.*, Phys. Rev. Lett. **94**, 195504 (2005)

[75] E. Zaccarelli *et al.*, Phys. Rev. Lett. **95**, 268301 (2005)

[76] M. Camargo and C. N. Likos, Phys. Rev. Lett. **104**, 078301 (2010)

[77] C. Mayer *et al.*, Nature Materials. **7**, 780 (2008)

[78] A. Wilk , *et al.*, Eur. Phys. J. E **32**, 127 (2010)

[79] R. Lund *et al.*, Phys. Rev. Lett. **96**, 068302 (2006)

[80] J. S. Pedersen, J. Chem. Phys. **114**, 2839 (2001)

[81] A. Poppe *et al.*, Macromolecules **30**, 7462 (1997)

[82] J. S. Pedersen, Adv. Colloid and Interface Sci. **70**, 171 (1997)

[83] C. von Ferber *et al.*, Eur. Phys. J. E **2**, 311 (2000)

[84] P.J. Carreau, Trans. Soc. Rheol. **16**, 99 (1972)

[85] G. Foffi *et al.*, Phys. Rev. Lett. **90**, 238301 (2003)

[86] W. Götze, in *Liquids, Freezing and Glass Transition*, edited by J. P. Hansen, D. Levesque, and J. Zinn-Justin (North-Holland, Amsterdam, 1991)

[87] B. Loppinet *et al.*, Macromolecules **34**, 8216 (2001)

[88] C. N. Likos *et al.*, J. Chem. Phys. **117**, 1869 (2002)

[89] A. A. Louis, P. G. Bolhuis, and J. P. Hansen, Phys. Rev. E **62**, (2000)

[90] A. Lang *et al.*, J. Phys.: Condens. Matter **12**, 5087 (2000)

[91] C. N. Likos *et al.*, Phys. Rev. E. **63**, 031206 (2001)

[92] C. N. Likos *et al.*, J. Chem. Phys. **126**, 224502 (2007)

[93] M. A. Glaser *et al.*, Eur. Phys. Lett. **78**, 46004 (2007)

[94] B. M. Mladek *et al.*, Phys. Rev. Lett. **96**, 045701 (2006)

[95] A. J. Archer, C. N. Likos, and R. Evans, J. Phys.: Condens. Matter **16**, L297 (2004)

[96] I. O. Götze, A. J. Archer, and C. N. Likos, J. Chem. Phys. **124** 084901 (2006)

[97] B. M. Mladek, G. Kahl, and C. N. Likos, Phys. Rev. Lett. **100**, 028301 (2008)

[98] D. A. Lenz , R. Blaak, and C. N. Likos, Soft Matter **5**, 2905 (2009)

[99] A. Narros, A. J. Moreno and C. N. Likos, Soft Matter **6**, 2435 (2010)

[100] C. N. Likos, M. Watzlawek, and H. Löwen, Phys. Rev. E **58**, 3135 (1998)

[101] S. Overduin and C. N. Likos, Eur. Phys. Lett. **85**, 26003 (2009)

[102] S. Overduin and C. N. Likos, J. Chem. Phys. **131**, 034902 (2009)

[103] A. J. Archer and R. Evans, Phys. Rev. E **64**, 041501 (2001)

[104] A. J. Archer and R. Evans, J. Phys.: Condens. Matter **14**, 1131 (2002)

[105] R. Evans, Adv. Phys. **28**, 143 (1979)

[106] R. Evans *et al.*, Mol. Phys. **80**, 755 (1993)

[107] R. Evans *et al.*, J. Chem. Phys. **100**, 591 (1994)

[108] I. S. Gradshteyn and I. M. Ryzhik, *Table of Integrals, Series and Products* (Academic Press, San Diego, 1994)

[109] J. S. Rowlinson and B. Widom, *Molecular theory of capillarity* (Oxford University Press, New York, 1982)

[110] J. Kuipers and E. Blokhuis, J. Colloid Interface Sci. **315**, 270 (2007)

[111] A. B. Bhatia, N. H. March, and M. P. Tosi, Phys. Chem. Liq. **9**, 229 (1980)

[112] M. M. Telo da Gama and R. Evans, Mol. Phys. **48**, 229 (1983)

[113] J. Winkelmann, J. Phys.: Cond. Matter. **13**, 4739 (2001)

[114] J. R. Henderson, Phys. Rev. E. **50**, 4836 (1994)

[115] S. Dietrich, In *Phase Transitions and Critical Phenomena Vol. 12*, Ed. C. Domb and J. L. Lebowitz (Academic Press, London, 1988)

[116] P. C. Ball and R. Evans, J. Chem. Phys. **89**, 4412 (1988)

[117] J. M. Brader *et al.*, J. Phys.: Condens. Matter **14**, L1 (2002)

[118] K. Binder *et al.*, Soft Matter **4**, 1555 (2008)

[119] S. van Teeffelen, A. J. Moreno, and C. N. Likos, Soft Matter **5**, 1024 (2009)

[120] A. J. Moreno and C.N. Likos, Phys. Rev. Lett. **99**, 107801 (2007)

[121] C. N. Likos *et al.*, Comput. Phys. Commun. **179**, 71 (2008)

[122] D. Frenkel and B. Smit B, *Understanding Molecular Simulation* (San Diego, Academic Press, 1996)

[123] D. A. Keen *et al.*, Phys. Rev. B **68**, 014117 (2003)

[124] A. Gray-Weale and P. A. Madden, J. Phys. Chem. B **108**, 6624 (2004)

[125] S. Hull *et al.*, J. Phys: Condens. Matter **19**, 40621 (2007)

[126] D. Coslovich, L. Strauss, and G. Kahl, Soft Matter, DOI:10.1039/c0sm00545b

[127] M. Bier *et al.*, Phys. Rev. Lett. **101**, 215901 (2008)

[128] A. Patti *et al.*, Phys. Rev. Lett. **103**, 248304 (2009)

[129] M. P. Lettinga and E. Grelet, Phys. Rev. Lett. **99**, 197802 (2007)

[130] G. Cinacchi and L. De Gaetani, Phys. Rev. E **79**, 011706 (2009)

[131] R. Matena, M. Dijkstra, and A. Patti, Phys. Rev. E **81**, 021704 (2010)

[132] G. Cinacchi and L. De Gaetani, Phys. Rev. Lett. **103**, 257801 (2009)

[133] A. Patti *et al.*, J. Chem. Phys. **132**, 224907 (2010)

[134] N. Kikuchi and J. Horbach, Eur. Phys. Lett. **77**, 26001 (2007)

[135] A. J. Moreno and J. Colmenero, J. Chem.Phys. **125**, 164507 (2006)

[136] Th. Voigtmann and J. Horbach, Phys. Rev. Lett. **103**, 205901 (2009)

[137] T. Neuhaus and C. N. Likos, to appear in J. Phys: Condens. Matter (2011) [arXiv:1008.1881]

[138] S. C. Glotzer, J. Non-Cryst. Solids **274**, 342 (2000)

[139] D. A. Lenz *et al.*, J. Phys. Chem. B, doi: 10.1021/jp109132m

[140] C. Pierleoni, B. Capone, and J. P. Hansen, J. Chem. Phys. **127**, 171102 (2007)

[141] B. Capone, C. Pierleoni, and I. Coluzza, Soft Matter **6**, 6075 (2010)

[142] S. Fejer, D. Chakrabarti, and D. J. Wales, Soft Matter, doi: 10.1039/c0sm01289k (2011)

[143] E. Bianchi, R. Blaak, and C. N. Likos, Phys. Chem. Chem. Phys. doi: 10.1039/c0cp02296a (2011)

[144] A. Nikoubashman, G. Kahl, and C. N. Likos, submitted (2011)

[145] C. von Ferber *et al.*, J. Mol. Liq. **93**, 151 (2001)

[146] C. Caccamo, Phys. Rep. **274**, 1 (1996)

Appendix A

Star polymers

Star polymers are a particular class of branched polymers, consisting of f linear polymer chains (arms) attached to a common branch point (core). Assuming that the arms are identical with respect to constitution and degree of polymerization (N), and that the core size is small compared to the length of the chains, the Daoud-Cotton model provides an elegant and transparent way to gain information about the conformation of an isolated star polymer, in particular its monomer density profile $\varrho(r)$, from which the effective interaction between two isolated stars can be derived [4, 5, 32, 33].

Daoud-Cotton model

This geometrical model employs scaling theory in the framework of blob model and regards the inner of the star as a succession of concentric shells of spherical blobs (see Fig. A.1), which are closely packed and within each one every chain behaves as if it were free. In a good solvent and as consequence of the topology, the blob size increases with the radial distance ($\xi(r) \sim f^{1/2}r$), and three monomer density regimes can be observed: (i) the melt-like core regime ($r \sim R_c$, $\varrho(r) \sim$ cte); (ii) the θ-like regime ($r \sim R_1$, $\varrho(r) \sim f^{1/2}/r$), in which blobs are ideal and only the solvent can penetrate in dense suspensions; and (iii) the excluded volume regime ($r \sim R$, $\varrho(r) \sim f^{2/3}/r^{4/3}$), in which blobs are swollen and star-star interpenetration can take place in dense suspensions [17].

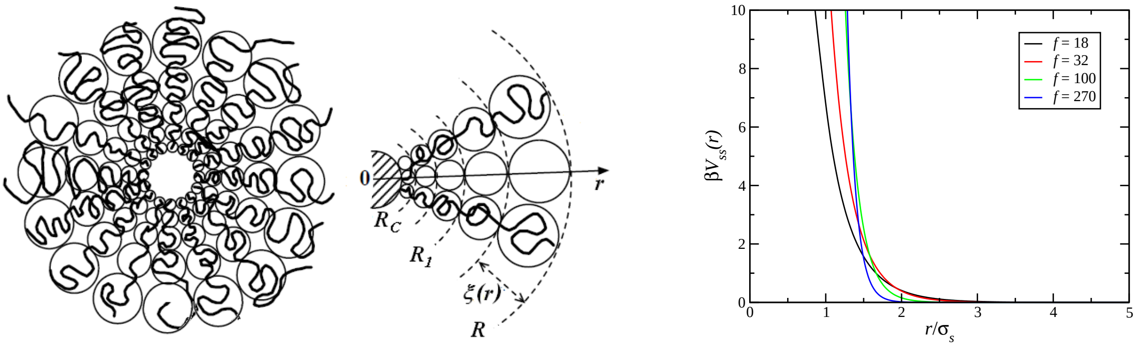

Figure A.1: Left: Schematic representation of the blob representation of the internal structure of a star polymer immersed in a good solvent. Right: Star-star effective potential for several functionalities.

Star-star effective interaction

In the derivation of the effective star-star interaction for good solvent conditions, i.e., when only excluded volume constraints are considered, three main aspects have been taken into account. In first place, the configurational partition function of a single star polymer is a power-law of the degree of polymerization N of the arms. Secondly, at very close approaches, two star polymers of f arms each closely resemble a single star with $2f$ arms. These two conditions lead to a logarithmic dependence of the interaction at short distances between the cores [33, 145]. Finally, the third and last consideration is that for high functionalities, star polymers are practically spherical objects exhibiting a Yukawa-like interaction at long distances, which is typical for sterically stabilized colloids. The resulting interaction potential reads:

$$\frac{V_{ss}(r)}{k_BT} = \frac{5}{18} f^{3/2} \begin{cases} -\ln\left(\frac{r}{\sigma_s}\right) + \frac{1}{1+\frac{\sqrt{f}}{2}} & r \leq \sigma_s \\ \frac{1}{1+\frac{\sqrt{f}}{2}} \left(\frac{\sigma_s}{r}\right) \exp\left[-\frac{\sqrt{f}}{2\sigma_s}(r-\sigma_s)\right] & r > \sigma_s \end{cases} \tag{A.1}$$

where $\sigma_s/2$ is the distance from star center to the center of the outermost blob and the the decay length of the Yukawa interaction is set by the diameter of the outermost blob diameter, $\xi_{\max} \sim 2\sigma_s/f^{1/2}$. As can be seen in Fig. A.1, as f increases the potential become harder and shorter-ranged [4, 5].

Appendix B

Ornstein-Zernike equation

Through the formalism of the distribution functions, it is possible to link the equilibrium thermodynamic properties of a fluid with the structural correlations between its constituting particles. Instead of a direct calculation of the partition function (Z_N), this formalism allows to describe the system by considering the probability of configurational groupings of two, three, and more particles [41]. The pair correlation function $g(\mathbf{r})$ particularly encloses much of the information concerning the thermodynamic and structural properties of a fluid. Solving the Ornstein–Zernike equation is a relatively fast way to obtain approximated results for $g(\mathbf{r})$.

The Ornstein-Zernike (OZ) equation of a homogeneous and isotropic monodispersed system is given by

$$h(r_{12}) = g(r_{12}) + 1 = c(r_{12}) + n \int c(r_{13}) h(r_{32}) d\mathbf{r}_3 \tag{B.1}$$

where $\mathbf{r}_i$ is the position of particle i, $r_{ij} = |\mathbf{r}_i - \mathbf{r}_j|$ $(i \neq j)$, and $h(r) = g(r) - 1$ is the total correlation function. So far, the OZ equation can be interpreted as a definition of the direct correlation function $c(r)$[1].

Equation (B.1) is an integral equation with two unknown functions, i.e. $h(r)$ and $c(r)$, so that an additional relation between them becomes necessary. This additional relation is known as closure relation, and can be derived from a diagrammatic analysis. The diagrams can be adequately grouped leading to the identity

$$g(r) = \exp\left[-\beta v(r) + h(r) - c(r) - B(r)\right] \tag{B.2}$$

---

[1] The $c(r)$ function is rigorously defined through density functional derivative methods [41].

where $v(r)$ is the interaction potential and $B(r)$ encloses the so-called bridge diagrams. By using the closure relation (B.2) the OZ equation would be transformed into an integral equation only for $h(r)$ (or $c(r)$) if $B(r)$ were replaced by an expression that involve only $h(r)$ (or $c(r)$). Since, the complete functional form of $B(r)$ is practically unknown, some approximated closure relation has to be considered.

The approximate closure relation must be consistent with two features of the potential: (i) if a hard-core potential is included, then $h(r < a) = -1$ with a the diameter of particles, and (ii) at large distances $c(r) \to -\beta v(r)$. In the literature, a number of approximative closure relations can be found, each of them giving reasonable results for particular pair potentials. They include among others, mean field (MFA), Perkus-Yevick (PY) and hypernetted chain (HNC) approximations. The MFA pertains to set $c(r) = -\beta v(r)$, while the PY and HNC closure relations come from a partial summation of terms (of all orders in density) of the diagrammatic expansion for $g(r)$. The HNC approximation neglects all bridge diagrams by setting $B(r) = 0$ in (B.2) whereas the PY approximation takes $B(r) = \ln(1 + h(r) + c(r)) - h(r) + c(r)$. The PY treatment is appropriate for describing the hard-core potential while HNC appears to account satisfactorily for long-range repulsive potentials [146].

Appendix C

Non-ergodicity factor

The decay of collective density fluctuations in a fluid of N identical particles is quantified by the normalized time-dependent density autocorrelation function, also known as coherent (or collective) scattering function, which is defined as,

$$F(q,t) = \frac{\langle \rho(\mathbf{q},t)\rho(-\mathbf{q},0)\rangle}{\langle \rho(\mathbf{q},0)\rho(-\mathbf{q},0)\rangle} \tag{C.1}$$

where $\rho(\mathbf{q},t) = \sum_{j=1}^{N} \exp[i\mathbf{q}\cdot\mathbf{r}_j(t)]$ and the sum is performed over the coordinates $\mathbf{r}_j$ of all particles in the system. The plateau value of $F(q,t)$, when present, provides a measure of the structural arrest in the fluid, which persists for times that increase rapidly with decreasing temperature or increasing the density [41].

The mode-coupling approach (MCT) to glass transition shows that the structural arrest appears as a consequence of a non-linear, feedback mechanism. Within MCT the glass transition is identified as an ergodic to non-ergodic transition when the non-ergodicity factor $f(q) = \lim_{t\to\infty} F(q,t)$, defined as the long-time limit of the density autocorrelation function $F(q,t)$, discontinuously jumps from zero (fluid) to a finite value (arrested state). The non-ergodicity factor can be obtained by numerically solving the equation

$$\frac{f(q)}{1-f(q)} = \frac{1}{2}\int \frac{d\mathbf{k}}{(2\pi)^3} V(\mathbf{q},\mathbf{k}) f(k) f(|\mathbf{q}-\mathbf{k}|) \tag{C.2}$$

$$V(\mathbf{q},\mathbf{k}) = \frac{\rho S(q)}{q^4}\left[\mathbf{q}\cdot\mathbf{k}\ \hat{c}(k) + \mathbf{q}\cdot(\mathbf{q}-\mathbf{k})\ \hat{c}(|\mathbf{q}-\mathbf{k}|)\right]^2 S(k)S(|\mathbf{q}-\mathbf{k}|) \tag{C.3}$$

where ρ is the number density and the direct correlation function $c(r)$ is related to the structure factor via the OZ equation in Fourier space, i.e., $S(q) = [1 - \rho\,\hat{c}(q)]^{-1}$ [41, 86].

Die hier vorgelegte Dissertation habe ich eigenständig und ohne unerlaubte Hilfe angefertigt. Die Dissertation wurde in der vorgelegten oder in ähnlicher Form noch bei keiner anderen Institution eingereicht. Ich habe bisher keine erfolglosen Promotionsversuche unternommen.

Düsseldorf, den 01.03.2011

Manuel Alfonso Camargo Chaparro